Title

An Experimental Study of Spin Seebeck Effect in Ferromagnetic/Semiconductor Heterostructure Thin Films

Permalink

Author

Bhardwaj, Ravindra Giriraj

Publication Date

2020

Peer reviewed|Thesis/dissertation

UNIVERSITY OF CALIFORNIA
RIVERSIDE

An Experimental Study of Spin Seebeck Effect in Ferromagnetic/Semiconductor
Heterostructure Thin Films

A Dissertation submitted in partial satisfaction
of the requirements for the degree of

Doctor of Philosophy

in

Mechanical Engineering

by

Ravindra G. Bhardwaj

September 2020

Dissertation Committee:
      Dr. Sandeep Kumar, Chairperson
      Dr. Richard B. Wilson
      Dr. Suveen N. Mathaudhu

The Dissertation of Ravindra G. Bhardwaj is approved:

_____

_____

_____
                                        Committee Chairperson

University of California, Riverside

Acknowledgements

I will remain very grateful to my doctorate advisor, Dr. Sandeep Kumar for providing support and motivation throughout my graduate career. I am thankful to all faculty members with whom I had a great experience while taking their courses. Also, I am also thankful to Dr. Ward P. Beyermann for providing experimental access and technical support and staff of Center for Nanoscale Science and Engineering.

This thesis contains exerts from several published and submitted articles.[1, 2, 3]

[1] Bhardwaj, R. G., Lou, P. C., & Kumar, S. (2018). Spin Seebeck effect and thermal spin galvanic effect in Ni80Fe20/p-Si bilayers. *Applied Physics Letters*, *112*(4), 042404 (*Editor's Pick*). DOI: https://doi.org/10.1063/1.5003008

[2] Bhardwaj, R. G., Lou, P. C., & Kumar, S. (2018). Giant Enhancement in Rashba Spin-Seebeck Effect in NiFe/p-Si Thin Films. *physica status solidi (RRL)–Rapid Research Letters*, *12*(6), 1800064. DOI: https://doi.org/10.1002/pssr.201800064

[3] Bhardwaj, R. G., Katailiha A., Lou, P. C., Beyermann W. P. & Kumar, S. Strain engineering of amorphous-Si thin film interfaces for efficient thermal spin to charge conversion. DOI: https://arxiv.org/abs/2001.01822v1

To my wife and parents for their affection and support

ABSTRACT OF THE DISSERTATION

An Experimental Study of Spin Seebeck Effect in Ferromagnetic/Semiconductor
Heterostructure Thin Films

by

Ravindra G. Bhardwaj

Doctor of Philosophy, Graduate Program in Mechanical Engineering
University of California, Riverside, September 2020
Dr. Sandeep Kumar, Chairperson

Magnetothermoelectrical devices are the prominent systems to generate electrical energy from heat source having small temperature gradient. The spin-Seebeck effect mediated thermoelectric energy conversion can provide an efficient alternative to traditional thermoelectric for waste heat recovery. To achieve this goal, efficient spin to charge conversion using earth-abundant materials is essential. Also, the thermal spin current from the spin-Seebeck effect has been reported to be more energy efficient than the electrical spin injection methods. However, spin detection has been the one of the bottlenecks since metals with large spin-orbit coupling is an essential requirement. Silicon is widely used in semiconductor electronics due to its abundance and versatility but having a centrosymmetric crystal structure, has insignificant intrinsic spin-orbit coupling, leading to negligible spin-charge conversion. However, in silicon, strain engineering mediated

Rashba spin orbit coupling can induce interfacial spin to charge conversion arises due to an electric potential perpendicular to the interface.

The electric potential can be artificially induced, for example, using ferroelectric and piezoelectric thin films at the interface. An alternate way to induce the electric potential could be flexoelectric field. The flexoelectricity can be observed in all the material that either have or lack inversion symmetry, additionally no large gate bias is needed. Hence, the interfacial asymmetry in conjunction with strain engineering can provide an alternate pathway to achieving efficient and controllable spin-to-charge conversion for spintronics applications. In this experimental study, we report large spin to charge conversion (spin-Hall angle- 0.578) at $Ni_{80}Fe_{20}$/amorphous-Si interfaces attributed to flexoelectricity mediated Rashba spin-orbit coupling. The flexoelectricity at the interface also gave rise to flexoelectric mediated interlayer coupling. In addition to spin-charge conversion, the strained interfaces also led to almost three-fold increase in anomalous Nernst effect. This strain engineering for spin dependent thermoelectric behavior at room temperature opens a new window to the realization of spintronics and spin-caloritronics devices.

Contents

List of Figures

List of Tables

Chapter 1

Introduction

Heat energy such as solar heat from the Sun or waste heat energy available freely from an operating equipment can be converted to useful electric potential using conventional Seebeck effect, discovered in 1821 by Thomas Johann Seebeck [1]. Seebeck effect generates electric potential when a temperature gradient is applied across the junction made by two electrical conductors or semiconductors having different Seebeck coefficients. Even though continuing research towards the development of highly efficient thermoelectric devices, the achieved efficiency of thermoelectric devices such as Peltier coolers and Seebeck thermopower devices has remained quite low [2]. Recently discovered spin dependent thermoelectric effect may provide new opportunities to improve the efficiency of thermoelectric energy conversion in magnetic materials, compared to electron based conventional thermoelectric energy conversion phenomena [3]. The study of spin-based phenomena driven by temperature gradient is known as spin caloritronics. The advantages of spin caloritronic effects is that they can be easily manipulated at nanoscale, fabricate in flexible design, and are highly efficient [2].

A temperature gradient drive the electrons, phonons, and magnons out of their thermodynamic equilibrium which will give rise to transport of charge, spin and/or heat [4]. Spin can be transported using conduction electrons, magnons, and phonons [5, 6]. Conduction electrons are the fermions that transport spins, charge, and heat [4]. Magnons

are the bosonic quasi particle that carry heat and spins generated through perturbations of localized magnetization in the lattice. Quantized spin waves are called magnon [4]. Phonon is a quanta of lattice vibrations. It is also a bosonic quasi particle. Phonons nominally transport heat via agitation of lattice vibrations. They do not carry charge or spin but are capable of exciting, scattering and dragging magnetic moment or charge from equilibrium [4].

In the field of spin-caloritronics, the magnetothermal mediated pure spin current can be generated via spin dependent Seebeck effect and spin Seebeck effect. The generation of spin dependent heat current due to non-equilibrium chemical potential of spin polarized electrons in ferromagnetic conductors may be known as spin dependent Seebeck effect [7]. It is observed by many research groups in various materials configuration not limited to $Ni_{80}Fe_{20}$ [8], Co [8], Py/Cu [9], Py/Ag [9], graphene [10, 11], Co/Pt multilayers [12], Co/Ni multilayers [12], and zigzag-edged silicene nanoribbons (ZSiNRs) [13]. On the other hand, the thermal spin current generation in spin Seebeck effect may originates because of propagation of spin waves which can be detected using inverse spin Hall effect [7]. It is observed in ferromagnetic metals [14, 15], ferromagnetic semiconductors [16], ferromagnetic insulators [17, 18], half metallic Heusler compound [19], non-magnetic semiconductor [20], antiferromagnets [21, 22], helimagnetic insulators [23] and organic materials [24]. It should be noted that the spin current in ferromagnet materials is carried by magnons or spin polarized electrons.

Even though there has been a lot of research in the recent field of spin Seebeck effect that discovered more than a decade ago, however the efficiency of spin to charge

conversion remains very low. Experimentally, the efficiency of spin to charge conversion may be lies between 0.01% to 58% for heavy metals, topological insulators, and antiferromagnets [25, 26], however, recently, the maximum spin to charge conversion efficiency is obtained by using Iridium oxide which is about 370% using ferromagnetic resonance, this makes the spin to charge conversion efficiency unpredictable [27]. There may be two fold increase in spin flux generation via thermal excitation as compared to ferromagnetic resonance which intrigues us to use temperature gradient to generate spin flux [4]. We observed spin to charge conversion efficiency of about 57% using thermal excitation. It is true that the observed effects are real and intriguing but complex for researchers to untangle. The applications of spintronics and spin caloritronics are wide and under development [28]. The highest reported spin Seebeck voltage probably is for topological insulator device about 175 μV, that having geometry about 56 times larger compared to ours device [29]. We tried to dig the well deep enough to discover something novel and intriguing which will be beneficial to understand the origin of the spincaloritronics phenomena. Spin detection has been the one of the bottlenecks since metals with large spin-orbit coupling is an essential requirement. Semiconductors such as silicon, despite having advantages such as it is abundant in nature, inexpensive, and easy manufacturing capabilities, is not considered as a strong competent material for spintronics and spin caloritronic due to its weak intrinsic spin orbit coupling (SOC).

The strain engineering is well known in the traditional thermoelectric field but its application in the spintronics and spin caloritronics field are very few. In this research work, we used the strain engineering to show the importance of silicon in the spintronics

3

and spin caloritronics field. We report an efficient thermal generation and interfacial detection of spin current. We measured a spin-Seebeck effect in $Ni_{80}Fe_{20}$ /a-Si bilayers without a heavy metal spin detector and giant inverse spin-Hall effect (spin-Hall angle, $\theta_{SHA} = 0.578$), essential for the detection of spin-Seebeck effects which originates from flexoelectricity mediated Rashba spin-orbit coupling due to structure inversion asymmetry at the interface. The flexoelectricity at the interface also gave rise to flexoelectric mediated interlayer coupling. In addition to spin-charge conversion, the strained interfaces also led to almost three-fold increase in anomalous Nernst effect. This strain engineering for spin dependent thermoelectric behavior at room temperature opens a new window to the realization of spintronics and spin-caloritronics devices.

Chapter 2

Fundamentals of Heat Assisted Spin Transport

Spintronics is the branch of the physics and material science which is analogous to the electronics except the later uses charge of electrons as a transport carrier while the former uses electron's spin degree of freedom along with its electronic charge and a net magnetic moment associated with a charge in motion. Spin is the intrinsic angular momentum of the quantum particles which has definite magnitude and direction. Spin of elementary particles is also called as spin quantum number which is defined as $s = \frac{n}{2}$ where n is the non-negative integer. Elementary particle having integer spins are known as bosons (photons) whereas particles having half-integer are known as fermions (electrons, neutrons, protons). Spin orbit coupling (SOC) also known as spin orbit interaction (SOI) is interaction between spin degree of freedom of electron and the effective magnetic field experienced by an electron under an finite electric field of nucleus or impurity [30, 31]. Spintronics phenomena controls spin transport such as Anomalous Hall Effect (AHE), Spin Hall Effect (SHE), Quantum Spin Hall Effect (QSHE), Inverse Spin Hall Effect (ISHE) and many more. Spintronics find its application in development of read heads for sensing dense magnetic storage data, non-volatile magnetic random access memory (MRAM), magnetic tunnel junction used in logic devices, position control devices in robotics, rotational speed control devices, magnetometers, and high current monitoring devices, etc. [32].

In the field of spintronics, the spin current generation, detection and measurement is of crucial importance. An additional method to generate spin current is using thermal excitation which is called as spin dependent thermoelectric energy conversion method. It is hypothesized that using thermal excitation, the intensity of spin flux generation may be twice as compared to ferromagnetic resonance [4]. The generated thermal spin flux can be converted to electric potential using Inverse Spin Hall Effect (ISHE) [14]. An innovative approach to improving thermoelectric energy storage and conversion is the spin dependent thermoelectric energy conversion using the spin Seebeck effect (SSE), anomalous Nernst effect (ANE), and spin Nernst effect (SNE), which will bring efficiencies because pure spin current, as opposed to charge current, is believed to be dissipationless [33]. Spin caloritronics is the study of interaction between spin with the heat energy [34]. In the spin caloritronics studies, the homogenous temperature gradient and the length scale dependent temperature gradient are established to study the interplay of spin degrees of freedom and temperature gradient in the magnetic structures [35]. Thermal excitation provides two-fold increase in the generation of spin flux compared to spin pumping using ferromagnetic resonance and three-fold increase compared to electrical spin injection via spin Hall magnetoresistance (SMR) [4]. Thermal driven spin flux generation methods are spin Nernst effect (SNE), spin dependent Seebeck effect (SDSE), spin Seebeck effect (SSE), magnon Hall effect (MHE), magnon Nernst effect (MNE) and many more. The imminent application of spin caloritronics is to overcome the thermodynamic bottleneck of Moore's law, reduction in the transistor size while improving the performance generates the unbearable ohmic energy generation due to the constraint motion of the electron [36].

6

Therefore, it is desired to utilize the spin degree of freedom of electron in order to manage the generated thermal heat in the devices and bring the impetus evolution by overcoming the current bottleneck in the field of electronics.

2.1 Fundamentals of Spintronics and Spin Caloritronics

Spintronics and spin caloritronics utilizes the spin degree of freedom of electron along with its charge. The spin of electron is defined by its precession direction, e.g. up spin and down spin is defined as anticlockwise and clockwise precession, respectively. Now, let us understand different types of spin currents.

Spin Current: Spin current is defined by the flow of spin angular momentum in certain directions due to spin potential. There are four types of current, unpolarized, spin polarized, fully polarized and pure spin current as shown in the Figure 2.1.
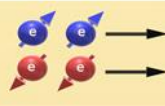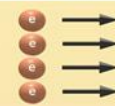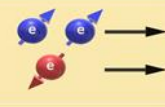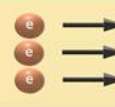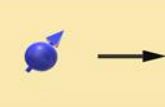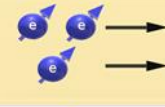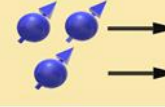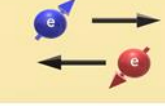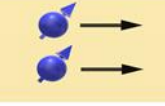
Types of current	Classical view	Charge current	Spin current
Unpolarized current			0
Spin-polarized current			
Fully polarized current			
Pure spin current		0	

Figure 2.1 Types of charge and spin currents

A pure spin current is generated when the equal number of spin up electrons and spin down electrons flows in opposite direction with the same drift velocity, annihilating the charges $I_c = I_c^\uparrow + I_c^\downarrow = 0$ while building a net flow of spin angular momentum, usually called as pure spin current $I_s = I_c^\uparrow - I_c^\downarrow \neq 0$. In case of magnetic insulators, pure spin current is obtained by coherent magnetization precession generating spin waves and their quanta is magnons that can transport heat and spin but not charge. A spin polarized current or fully polarized current is observed when there is net flow of charge and spin angular momentum due to asymmetry in the spin up and spin down electron band structure. Spin current can be generated using spin Hall effect (SHE), spin pumping, spin Seebeck effect (SSE) and photoexcitation [36].

Spin Hall Effect (SHE): When a charge current is passing through a material having strong spin-orbit coupling, there is accumulations of net spin on the opposite sides of a material generating a pure spin current which is polarized in the direction perpendicular to both the

direction of charge current and spin current [37]. This phenomenon is due to the strong spin orbit coupling of the material that results in a spin-dependent transverse deflection of the charge carriers known as spin Hall effect (SHE) as shown in Figure 2.2 (a). The mechanism for SHE in NMs are spin-selective scattering on impurities (extrinsic), and/or inherent spin orbit coupling (intrinsic) [4]. Spin orbit coupling is the process of interaction between spin angular momentum and orbital momentum of electron which will ultimately couples the charge and spin of electrons [38]. The extrinsic mechanism are skew scattering and side jump. In skew scattering, the scattering of conduction electron is depending on the direction of spin orbit interaction and direction of spin of electron [39]. The direction of magnetic field experienced by a conduction electron due to spin orbit interaction is different for electrons moving in different directions. Thus, electrons moving in a conductor will experience a directional dependent scattering that generates a spin polarized current perpendicular to the conductor. In side jump, the scattering of conduction electrons depends on the interaction of spin of electron with the direction of spin orbit interaction due to defect [39]. Defects has its own nuclear electric potential which is opposite in direction at the opposite side of the defects. This electric field of defect induce magnetic field of spin orbit interaction which interact with nearby drifting conduction electron. Depending on the position of conduction electron with respect to defect, the spatial dependent and spin dependent electron scattering takes place resulting in the generation of spin polarized current perpendicular to the conductor. The intrinsic mechanism is dependent on the spin band structure, that occurs due to the non-equilibrium Bloch electrons dynamics [40].

The efficiency of spin to charge or charge to spin conversion is given by the spin Hall angle (SHA), defined as [41],

$$\theta_{SH} = \frac{2e}{\hbar}\left(\frac{j_s}{j_c}\right) \tag{1}$$

Where j_s, j_c and $\hbar$ are spin current generated by SHE, charge current due to applied electric potential and $h/_{2\pi}$ respectively. Heavy metals such as Pt, Ta, Au and W have large spin orbit coupling (SOC) [41]. Semiconductors such as indium arsenide and indium selenide also possess large spin orbit coupling [42].

Inverse Spin Hall Effect (ISHE): When a spin current is passed into a normal metal (NM) having strong spin-orbit coupling, the spin current is converted into a transverse electric field by ISHE. When a spin current is passed through NM, due to spin orbit coupling, electrons of same kind of spin gets accumulated at one side of the material. Simultaneously, electrons of the opposite kind of spin are pulled away from the opposite side of the material and creates holes in that region maintaining charge neutrality in the direction of applied spin flux. This creates a perpendicular electric field to spin flux as shown in the Figure 2.2 (b) [43]. The ISHE voltage E_{ishe} generated perpendicularly to the magnetization M is given by equation,

$$E_{ishe} = (\theta_{SH}\rho)J_S \times \sigma \tag{2}$$

where, θ_{SH}, ρ, J_S and σ are spin hall angle, electrical resistivity of paramagnetic metal, longitudinal spin current due to SSE, and spin polarization vector. The longitudinal voltage shows $\sin\theta$ dependence with two measuring segments at an angle other than 45° and

depends on the FM material and temperature gradient [44]. ISHE does not allow to detect magnetic texture but detects spin current behavior [45].

For many years there is no significant improvement in commercially available thermoelectric semiconductor devices. The material with efficient thermoelectric performance require complex and scarce (rare earth) elements [46]. The thermoelectric energy storage and conversion is enhanced and improved by using spin dependent thermoelectric energy conversion phenomena such as spin Seebeck effect (SSE), anomalous Nernst effect (ANE), and spin Nernst effect (SNE) because they involves dissipationless pure spin current [33]. In the spin caloritronics studies, the homogeneous temperature gradient and the length scale dependent temperature gradient are established across the sample to study the interplay of spin degrees of freedom with respect to temperature gradient in the magnetic structure [47].
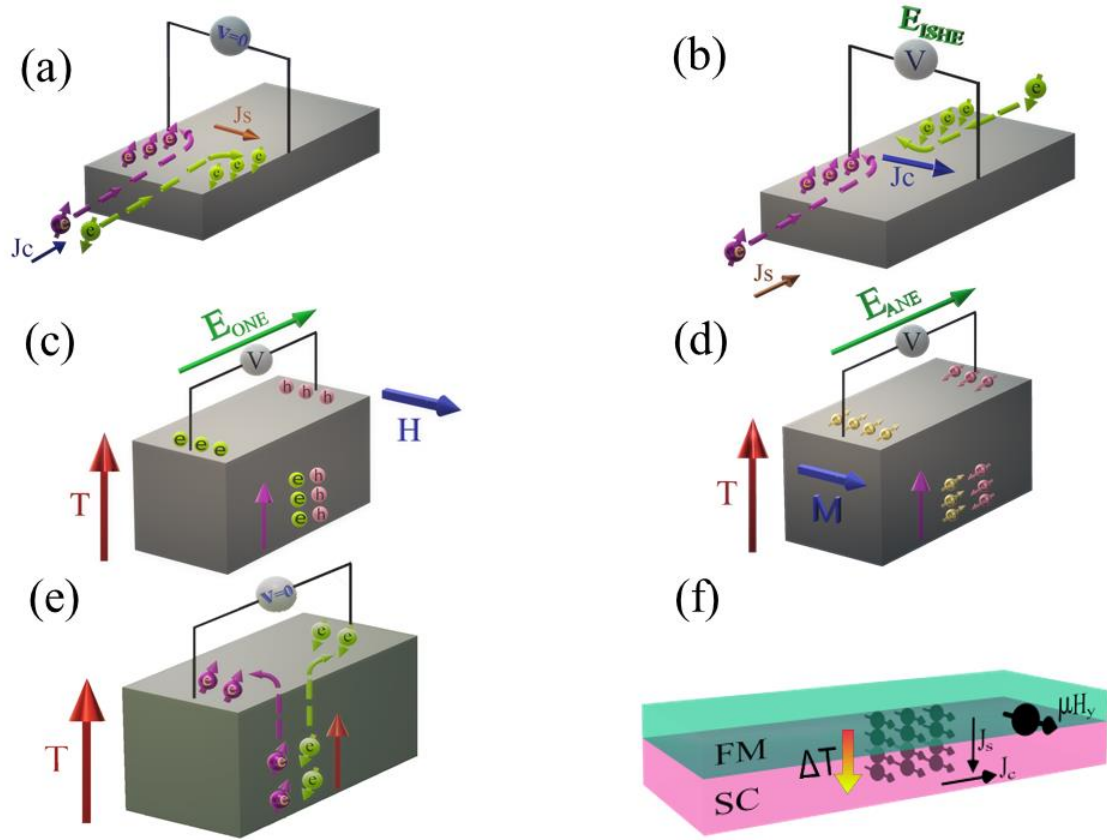
Figure 2.2 Spintronics and spin caloritronics effects. Schematic of (a) spin Hall effect (b) inverse spin Hall effect (c) ordinary Nernst effect (d) anomalous Nernst effect (e) spin Nernst effect (f) spin Seebeck effect

Ordinary Nernst Effect (ONE): Ordinary Nernst effect or Nernst effect is the thermoelectric effect observed when a uniform temperature gradient is applied to a conducting material under an external magnetic field will induce a perpendicular electric voltage (E_{ONE}) to the magnetic field and temperature due to Lorentz force [4] as shown in the Figure 2.2 (c). The ordinary Nernst electric field is given by following equation,

$$E_{ONE} = \mu_0 D_{ONE} \nabla T \times H \tag{3}$$

where, μ_0, D_{ONE}, ∇T and H are permeability of free space, ordinary Nernst coefficient, temperature gradient and applied magnetic field, respectively. D_{ONE} coefficient is used to determine the efficiency of the ONE and to identify the type of carrier present in the material.

Anomalous Nernst Effect (ANE): In ferromagnetic conductor (metal or doped semiconductor), the application of temperature gradient across the material will produce transverse Nernst voltage due to Lorentz force created by internal magnetic field of the magnetization as shown in Figure 2.2 (d), unlike the Nernst effect in which an external magnetic field must apply to the material [4]. The anomalous Nernst electric field perpendicular to the magnetization M and applied temperature gradient ∇T is given by relation $E_{ANE} \propto -M \times \nabla T$. Thus, when temperature gradient is parallel to M, the V_{ANE} vanishes [45]. The Anomalous Nernst coefficient α is given by $\alpha = \chi S$, where S = ordinary Seebeck coefficient and χ = a parameter. The ANE coefficient is proportional to the magnetization [48]. ANE can contribute to ISHE in paramagnetic material due to static magnetic proximity effects [49].

Spin Nernst Effect (SNE): The generation of transverse spin current by the application of longitudinal temperature gradient in the paramagnetic marital having large spin hall angle (W, Pt) is known as spin Nernst effect as shown in the Figure 2.2 (e) [50]. Spin orbit coupling is not the necessary condition to generate the spin current through the SNE but spin Hall conductivity is a must requirement [51]. Spin Nernst angle θ_{SNE} is defined as the

amount of transverse spin current J_S produced by application of heat current J_Q. The equation for θ_{SNE} is defined as,

$$\theta_{SNE} = \frac{J_S}{S\sigma_e \nabla T} \tag{4}$$

where, S, σ_e, and ∇T are Seebeck coefficient, electrical conductivity, and temperature gradient [51]. Different materials can have different sign for θ_{SNE}, also have $\theta_{SNE} > 1$ [52]. SNE can be measured by thermal spin Hall magnetoresistance (TSMR) and local differential detection method (LDD). Thermal spin Hall magnetoresistance is the thermal analog of spin Hall magnetoresistance (SMR)

Spin Hall Magnetoresistance (SMR): Spin Hall magnetoresistance (SMR) is the phenomena of change in electrical resistance of the electric conductor which is in contact with a magnetic material due to the SHE (spin current generated in FM or semiconductor because of their large spin hall angle) [53]. In general, when a charge current is passed in a heavy metal (NM) attached to the ferromagnetic material (FM), the charge current is converted to transverse spin current due to SHA. The generated spin current is injected to the attached FM through the NM/FM bilayer interface, and some part of it flows back into the NM. This returning spin current will get converted to transverse charge current via ISHA and thus change the longitudinal resistance. The SMR depends on the direction of spin (σ_S) and direction of the magnetization (M). In TSMR, the temperature gradient will initiate the generation of charge current in the NM and change the longitudinal resistance due to the SNE. Similar to SMR, there is anomalous magnetoresistance effect (AMR) which describes the change in the electrical resistivity of spontaneous ferromagnetic

materials due to the change in the relative direction between the charge current (J_C) and magnetization (M) [51].

Recent discovery of SSE in 2008 by Uchida *et al.* has led to tremendous progress in ongoing research on generation of pure spin current, a precession of spins or flow of electrons with opposite spins in opposite directions, over a large distance in spintronic devices with the aid of applied temperature gradient in ferromagnetic (FM) materials [14, 54, 55]. The SSE can be an efficient way to produce low cost and high memory spintronic devices [56]. The SSE is observed in ferromagnetic metals [44, 48, 57-61], semiconductors[4, 62-64], insulators[45, 49, 65-69] and even in half metallic Heusler compounds[70]

Spin Seebeck Effect (SSE): The SSE is a two-step spin dependent interfacial effect occurs between a spin polarized ferromagnet and a normal metal (NM) [14]. The first step consists of application of temperature gradient across the specimen to generate heat current is generated from phonon-magnon or phonon-electron interactions [71, 72]. The heat current leads to generation of spin currents in the spin-polarized material [73]. Spin current is in the form of magnons, spin polarized current due to electron or combination of both [72]. In the second step, spin current is injected across the interface from spin polarized FM into NM due to spin potential gradient available between FM and NM at the interface and converted to charge current as shown in the Figure 2.2 (f) [74]. The phenomena responsible for conversion of pure spin current to charge current is inverse spin-Hall effect (ISHE). The spin current generated in a FM material is detected using heavy metals such as Pt, W and Ta by the inverse spin-Hall effect due to their high spin orbit coupling [56, 61, 75].

The spin polarized FM material act as spin source and NM as the spin sink [4]. The NM is generally material with large spin orbit coupling such as Pt, W and Ta [14, 56, 75]. Thus, the major advantage of spin Seebeck effect is that it uses the properties of two or more materials that can be independently optimized [15]. The SSE, discovered by Uchida et al. [61, 76], is a composite effect of thermal spin current and spin-to-charge conversion, which produces an electric field given by,

$$E_{ISHE} = -S\sigma \times \nabla T \qquad (5)$$

where, S is spin Seebeck coefficient and σ is the spin polarization vector. In the above equation, σ can be replaced by M (magnetization), which gives rise to an equation for an anomalous Nernst effect (ANE). It was noted that both SSE and ANE have identical symmetry behavior, which may lead to false identification of ANE as SSE [48, 59].

There are two universal SSE device set-up, longitudinal spin Seebeck effect (LSSE) and transverse spin Seebeck effect (TSSE), in which the in-plane external magnetic field and temperature gradient are applied in the plane of the sample to measure SSE as shown in Figure 2.3 (a) and (b) respectively [47]. In LSSE, the spin current is generated parallel to applied temperature gradient as opposed to the spin current being perpendicular to the temperature gradient in the TSSE [55, 56, 60]. The thermoelectric energy conversion from spin current to charge current depends on the efficient spin to charge conversion due to spin-orbit coupling in NM. The spin Hall Angle (SHA) is the measure of efficient spin to charge conversion given by ratio of charge current generated to the injected spin current [77]. The material with large SHA is Pt, W, and Ta and requires further scientific research

16

in spin dependent thermoelectric energy conversion behavior. The efficiency of SSE device is given by spin Seebeck coefficient (SSC) and it is required to discover larger values of SSC to make efficient spin mediated thermoelectric energy conversion into reality. The SSC for longitudinal SSE device configuration is given by following equation:

$$S_{LSSE} = \frac{E_{ISHE}}{\nabla T} = \frac{V_{ISHE}t_{FM}}{w_{NM}\Delta T} \tag{6}$$

where V_{ISHE}, t_{FM}, w_{NM}, and ΔT are electric voltage measured due to ISHE by the paramagnetic metal or the NM, thickness of the FM material, distance between electrical contact in NM and temperature gradient across the sample respectively [78].

The transverse spin Seebeck effect (TSSE) is first observed experimentally in 2008 by K. Uchida *et. al.* The schematic of TSSE is as shown in the Figure 2.3 (b), where more than two normal metal as spin current detector are attached to the magnetic spin current source. When an in plane temperature gradient is applied along the magnetic material which is perpendicular to the length of spin current detector, the spin current is generated having out of plane direction (J_S) with spin polarization vector (σ) parallel to the magnetization direction (M) of the magnetic material. The generated spin current is injected to the attached normal metal strip and due to the ISHE this injected spin current is converted to detectable charge current. Uchida *et. al.* used ferromagnetic $Ni_{81}Fe_{19}$ film of 20 nm thickness, 6 mm long as a spin source and Pt layer having 10 nm thickness, 4 mm length and 10 µm wide as spin detector. They calculated spin Seebeck coefficient of $-2\,nV/K$ for $Ni_{81}Fe_{19}$ at 300 K as compared to Seebeck coefficient of $-20\,\mu V/K$ for $Ni_{81}Fe_{19}$ [14]. As shown in Figure 2.3 (b), in transverse SSE device, the direction of spin currents is opposite in direction at the near end compared to far end. This happens because

the Seebeck coefficient of up-spin and down-spin conduction electrons are different. The spin voltage is the difference between up-spin and down spin electron's electrochemical potential $(\mu_\uparrow - \mu_\downarrow)$ which is a function of temperature difference. The temperature gradient will generate a finite gradient of spin voltage $\nabla(\mu_\uparrow - \mu_\downarrow)$ having opposite direction at the near end as compared to far end, which ultimately generates spin current in opposite direction at the near end as compared to far end. H. Adachi *et. al.* observed gigantic enhancement in spin Seebeck coefficient about 0.5 µV/K at 50 K using transverse spin Seebeck device with ferrimagnetic insulator $LaY_2Fe_5O_{12}$ as a spin source and Pt as spin detector as shown in Figure 2.4 (a) [71]. They hypothesized that the phonon drag mechanism is responsible for this SSE enhancement since phonon drag mechanism is very effective at low temperature. The non-equilibrium phonons generated because of temperature gradient in magnetic insulator drag the magnons out of their equilibrium because of phonon magnon interactions and generate spin current. This spin current is injected into the attached Pt layer and converted to electric voltage due to ISHE [71]. As shown in Figure 2.4 (a), the solid circles show the experimental values where the maximum value occurs around 50 K. The red colored solid curve shows the numerically calculated SSE signal as a function of temperature due to magnon mediated SSE and phonon drag phenomena. While the blue colored dashed curve is plotted for only magnon mediated SSE signal which clearly suppressed at low temperature and thus is not able to explain low temperature SSE signal enhancement.
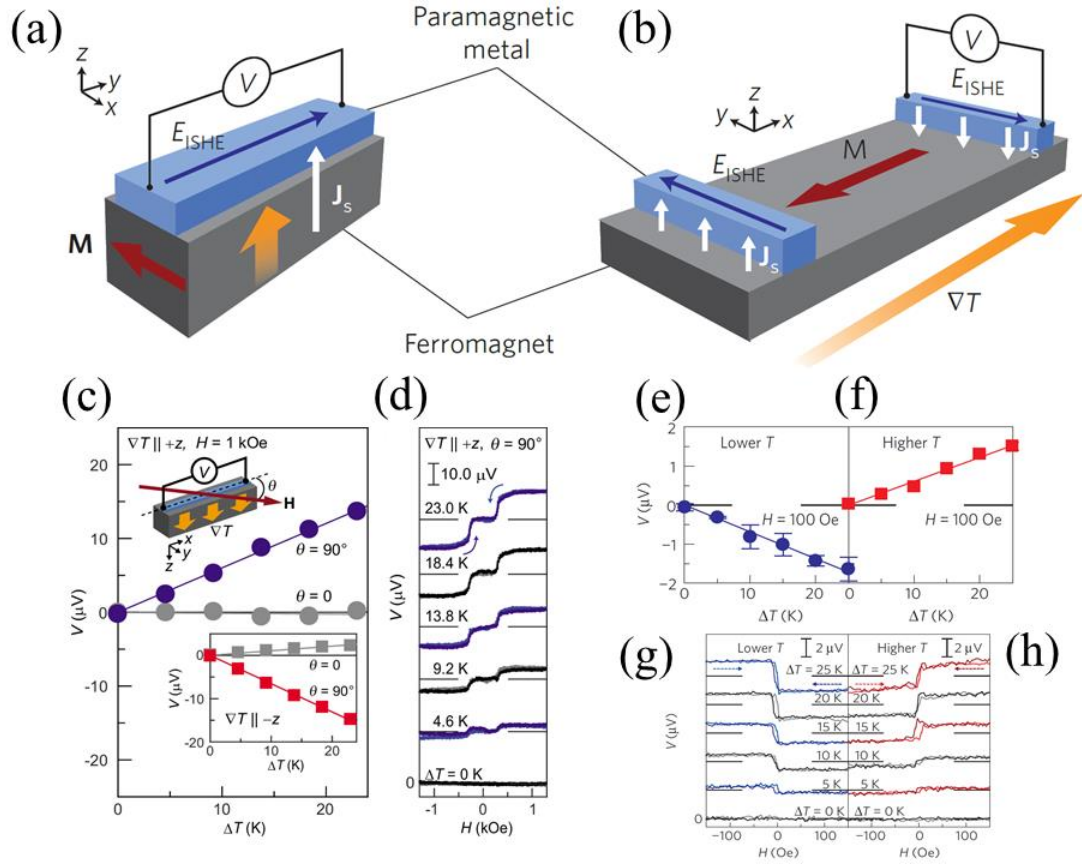
Figure 2.3 Spin Seebeck device configurations (a) longitudinal spin Seebeck device (b) transverse spin Seebeck device. Reprinted by permission from ref [34], © 2012. (c) ISHE voltage as a function of applied temperature gradient in +z direction for $Y_3Fe_5O_{12}$/Pt LSSE device configuration for applied magnetic field H = 1 kOe. Inset in (c), shows observed ISHE voltage as a function of applied temperature gradient in -z direction. θ is the angle between the direction of applied magnetic field and x-axis. (d) ISHE voltage as a function of applied magnetic field for various temperature gradients applied in +z direction for $Y_3Fe_5O_{12}$/Pt LSSE device configuration when $θ = 90°$. Reprinted by permission from ref [17], © 2010. (e, f) ISHE voltage as a function of temperature gradient for $LaY_2Fe_5O_{12}$/Pt TSSE device configuration for H = 100 Oe when Pt film is at lower temperature (300 K, e) and at higher temperature (300 K + ΔT, f) at ends of the $LaY_2Fe_5O_{12}$ film. (g, h) ISHE voltage as a function of applied magnetic field for $LaY_2Fe_5O_{12}$/Pt TSSE device configuration at various temperature gradients, when Pt film is attached to lower temperature (g) and at higher temperature (h) ends of the $LaY_2Fe_5O_{12}$ film. Reprinted by permission from ref [55], © 2010.

The longitudinal spin Seebeck effect (LSSE) is first observed in 2010 by K. Uchida

et. al. in ferrimagnetic insulator $Y_3Fe_5O_{12}$ ($6\ mm \times 2\ mm \times 1\ mm$) and measured by the

paramagnetic Pt film ($6\ mm \times 0.5\ mm \times 15\ nm$) [17]. The schematic of LSSE device is as shown in Figure 2.3 (a) which is considered to be more simple and versatile as compared to TSSE device configuration. In LSSE device configuration the spin current is generated in the direction of applied temperature gradient [17]. The LSSE configuration is usually considered for insulating ferromagnetic materials which acts a spin current source so that the signal from spurious effects such as short circuit current due to electrical conduction of conductive ferromagnet and ANE effect in ferromagnetic material are eliminated [17]. In LSSE device, the out of plane temperature gradient applied along the magnetic spin current source will generate spin current in spatial direction (J_S) as shown in the Figure 2.3 (a). This generated spin current is injected to the attached normal metal usually heavy metal with high spin orbit coupling and gets converted to detectable charge current in the normal metal by ISHE. For $Y_3Fe_5O_{12}$/Pt LSSE device, the ISHE voltage is directly proportional to the temperature difference (ΔT) when the applied magnetic field is perpendicular to the direction of applied temperature gradient ($\theta = 90°$). When the direction of applied temperature gradient is reversed, the sign of ISHE voltage also gets reversed in the normal metal, which is due to the LSSE as shown in the Figure 2.3 (c). This sign reversal occurs because the direction of spin current at the $Y_3Fe_5O_{12}$/Pt interface gets reversed when the direction of temperature gradient is reversed [17]. This is one of the attributes of LSSE. Including this, one more attribute of the LSSE is reversal of ISHE voltage (V) sign by reversing the direction of applied in-plane magnetic field (H) (when $\theta = 90°$) as shown in the Figure 2.3 (d).

As shown in the Figure 2.3 (d) and (g), the sign of ISHE voltage is opposite because the sign of the spin current generation in magnetic insulator / normal metal in LSSE and TSSE is opposite at the lower temperature regime for TSSE. It is hypothesized that this can be understood from imbalance between effective temperature of conduction electron (T_e^*) in normal metal and effective temperature of magnons in magnetic insulator (T_m^*). In LSSE device setup, the normal metal is in direct contact with the heat bath, exposing normal metal to phonon excitations. Now as the electron-phonon interaction is much stronger in normal metal than magnon-phonon interaction in magnetic insulator, the $T_e^* > T_m^*$ at the magnetic insulator / normal metal interface. Contradictory, in TSSE device setup, the normal metal is not in the contact of heat bath while magnetic insulator is in direct contact with heat bath. Thus, the excited phonons will not interact with electrons in normal metal, while they interact with the magnons in magnetic insulator, generating $T_m^* > T_e^*$. This difference in T_m^* and T_e^* may be the origin of sign reversal of SSE in LSSE and TSSE [17].

Transverse spin Seebeck effect is observed in following research articles which are as discussed. Jaworski, C. M., *et al.* observed TSSE in ferromagnetic semiconductor GaMnAs for the first time using Pt film as spin current detector [64]. They also observe voltage signal by using only point contact in GaMnAs without using any Pt film. This interesting signal is originating due to the contribution from SSE and PNE effect, and the spin to charge current conversion may be arising due to self-induced ISHE in GaMnAs [64]. Uchida, K. I., *et. al.* experimentally observed phonon mediated SSE in ferromagnetic metal $Ni_{81}Fe_{19}$ detected by ISHE in Pt film using TSSE device configuration [79]. They fabricated $Ni_{81}Fe_{19}$ $(3\,mm\,\times 0.1\,mm\,\times 20\,nm)/$ Pt $(3\,mm\,\times 0.1\,mm\,\times 10\,nm)$

bilayer structure on sapphire substrate $(10\ mm \times 3\ mm \times 0.5\ nm)$. Owning to insulating, non-magnetic and thermally conductive property of sapphire, the $Ni_{81}Fe_{19}/$ Pt bilayer sample is electrically and magnetically isolated, while only acoustic phonons from sapphire substrate are responsible for the observed phonon mediated SSE in ferromagnetic metal due to the phono-magnon coupling [79]. Substrate also plays an important role in driving phonon mediated spin Seebeck effect due to uncontrollable perpendicular temperature gradient [44, 79]. To address this, Huang, S. Y., *et. al.* fabricated a free standing sample without any underneath substrate and measured intrinsic spin dependent thermoelectric signals as shown in the Figure 2.4 (b), (c) and (d) [44]. They used 20 μm thick Fe film suspended on Cu blocks at both the ends as shown in the Figure 2.4 (b). A completely symmetric transverse thermal transport signal is observed as a function of applied in-plane magnetic field at different angles when a longitudinal temperature gradient is applied along the Fe film, which is as shown in the Figure 2.4 (c), as opposed to asymmetric behavior observed when a substrate is used in spin Seebeck effects. As shown in the Figure 2.4 (d), the angular dependence of thermal voltage behavior shows $\cos^2 \theta$ dependence which is anisotropic magnetoresistance (AMR), different from $\sin \theta$ behavior observed in thin films on substrate [44]. It should be noted that, they did not measure the thermal voltage signal using ISHE for the same device and thus only considered as spin dependent thermal voltage. It should be interesting to implement the free-standing geometry in spin Seebeck measurement to remove the phonon drag occurring from the substrate.
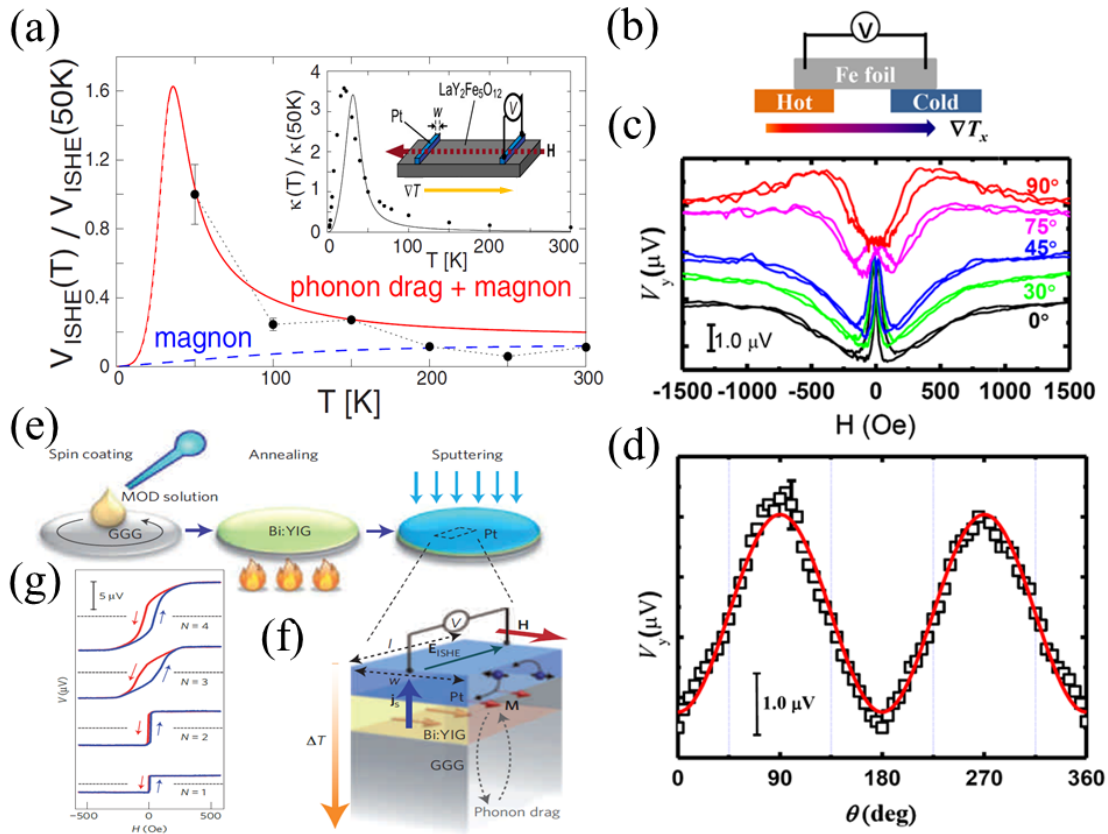
Figure 2.4 (a) Red colored solid curve shows the calculated ISHE voltage as a function of temperature due to both phonon drag TSSE and magnon mediated TSSE for LaY$_2$Fe$_5$O$_{12}$/Pt device. Blue colored dash curve shows the calculated ISHE voltage as a function of temperature due to magnon mediated TSSE for LaY$_2$Fe$_5$O$_{12}$/Pt. Solid black circles shows normalized experimental TSSE data for LaY$_2$Fe$_5$O$_{12}$/Pt. Inset: solid circles shows experimental values of thermal conductivity for LaY$_2$Fe$_5$O$_{12}$, solid curve shows fit. The schematic of TSSE device for LaY$_2$Fe$_5$O$_{12}$/Pt is also shown in the inset. Reprinted by permission from ref [71], © 2010. (b) Schematic of experimental setup for measuring intrinsic spin dependent thermal transport measurement in free standing Fe film. (c) Thermal voltage as a function of applied field at different angles with respect to the applied temperature gradient. (d) Saturated thermal voltage response as a function of field rotation, where red colored solid curve shows the fit to the experimental data shown by small black colored blocks. Reprinted by permission from ref [44], © 2011. (e) Schematic of spin thermoelectric coating process. The STE coating of Bi:YIG is done on GGG substrate by spin coating the MOD solution following annealing. The Pt layer is sputtered on top of Bi:YIG coat. (f) Schematic of LSSE process mediated by phonon drag, where spin current J_s injected into Pt is converted into charge current due to the ISHE. (g) ISHE voltage response as a function of applied magnetic field for different coating steps of Bi:YIG on GGG substrate for $\Delta T = 3\,K$. Reprinted by permission from ref [80], © 2012.

23

Schmid, M., *et. al.* fabricated free standing and conventional TSSE device to observe the contribution of transverse thermoelectric signal from the substrate using ISHE [59]. They observed minimal TSSE response when 20 nm thick Py film is deposited on GaAs or MgO substrate with 10 nm thick Pt strip on Py, while they did not observe TSSE response in 20 nm thick freestanding Py film on 100 nm thick SiN_x membrane with 10 nm thick Pt strip on Py [59]. They hypothesize that the observed transverse thermoelectric response is due to anisotropic magneto thermopower and phonons does not play an important role in their experimentation [59]. Bosu, S., *et. al.* observed TSSE response at room temperature, in half metallic ferromagnetic Heusler compound Co_2MnSi ($6\ mm\ \times 3\ mm\ \times 20\ nm$) deposited on MgO substrate and detected by using ISHE in Pt thin film ($3\ mm\ \times 0.1\ mm\ \times 10\ nm$) deposited on top of Co_2MnSi [70]. Jaworski, C. M., *et. al.* observed giant TSSE in nonmagnetic semiconductor InSb ($15\ mm\ \times 5\ mm\ \times 0.5\ mm$) and detected by ISHE using Pt thin film attached on top of InSb [20]. They obtained a large value of spin Seebeck coefficient of 8 mV/K at 2.8 K [20]. Chang, P. H., *et. al.* observed TSSE in 3D topological insulator Bi_2Se_3 where the spin current generated on the surface of Bi_2Se_3 injected to the attached Pt strip on top of Bi_2Se_3 to generate transverse thermoelectric voltage due to ISHE in Pt as shown in the Figure 2.5 (c) [65]. They measured a spin Seebeck coefficient of 2.5 μV/K [65].

The longitudinal spin Seebeck effect has been observed in different materials by various research groups which are as discussed. Uchida *et. al.* observed LSSE in sintered polycrystalline ferrimagnetic insulator (Mn, Zn) Fe_2O_4 ($6\ mm\ \times 2\ mm\ \times 1\ mm$) using sputtered Pt film ($6\ mm\ \times 0.5\ mm\ \times 15\ nm$) as spin current detector [56]. Weiler,

Mathias, *et. al.* observed LSSE in 10 nm thick insulating ferrimagnet $Y_3Fe_5O_{12}$ (YIG) grown on 1 mm thick $Gd_3Ga_5O_{12}$ (GGG) substrate and detect the spin current using ISHE in 7 nm thick Pt film deposited on top of YIG [45]. They calculated a spin Seebeck coefficient of 0.059 µV/K at room temperature [45]. Kirihara, A., *et. al.* used spin thermoelectric (STE) coating technique to make a LSSE device of bismuth substituted $Y_3Fe_5O_{12}$ (Bi:YIG) ($5\ mm \times 2\ mm \times 60\ nm$) coated on 0.7 mm thick GGG substrate and using Pt to convert spin current to charge current using ISHE as shown in the Figure 2.4 (e) and (f) to scale up the elemental LSSE device configuration [80]. They observe a large spin Seebeck coefficient about 9.6 mV/K and also shows that ISHE voltage response increases as the coating of Bi:YIG is repeated as shown in the Figure 2.4 (g) [80]. In LSSE, the normal metal such as Pt is in direct contact with ferromagnetic material which induces magnetic proximity ANE effect in normal metal by exchange coupling which is difficult to separate from LSSE as both LSSE and ANE have similar configuration [48]. To remove magnetic proximity effect and contribution of ANE effect, Kikkawa, T., *et. al.* implemented spin current detector which does not obey Stoner ferromagnetic instability such as Au and Cu [81]. By using LSSE setup, they fabricated Au/YIG and Pt/Cu/YIG LSSE device on GGG substrate. The Au/YIG device on GGG substrate have dimensions of ($7\ mm \times 6\ mm$), where Au is 10 nm thick, YIG is 4.5 µm thick and GGG substrate is 0.5 mm thick. The Pt/Cu/YIG device on GGG substrate have dimension of ($7\ mm \times 6\ mm$), where Pt is 10 nm thick, Cu is 13 nm thick, YIG is 4.5 µm thick and GGG substrate is 0.5 mm thick [81]. The proximity ANE effect is removed using Au as a spin current detector in Au/YIG bilayer structure and using Cu having very large spin

25

diffusion length (400 nm) as a spacer layer to eliminate proximity effect between Pt and YIG in Pt/Cu/YIG trilayer structure [81].

Ramos, R., *et. al.* observed LSSE in 50 nm thick ferrimagnetic oxide and half metallic Fe_3O_4 deposited on 0.5 mm thick $SrTiO_3$ substrate, where the spin to charge current conversion is take place by ISHE in 5 nm thick Pt film on top of Fe_3O_4 [15]. They obtained a spin Seebeck coefficient of 74±1 nV/K at room temperature [15]. Vlietstra, N., *et. al.* observed SSE in Hall bar structure of Pt (5 nm thick) /YIG and Ta (10 nm thcik) /YIG, where YIG is 200 nm thick grown on GGG substrate by external heating technique and current-induced heating method, as shown in Figure 2.5 (a) [82]. The external heating technique will only show the SSE response while the current-induced heating method will show both SMR and SSE response, where, by measuring second harmonic response using lock-in amplifiers the SMR effect can be removed and only SSE signal can be recorded [82]. They also showed that the ISHE signal gets flipped for Pt and Ta due to their opposite spin Hall angles as shown in Figure 2.5 (b) [82]. Wu, S. M., *et. al.* observed LSSE in paramagnetic insulators $Gd_3Ga_5O_{12}$ (gadolinium gallium garnet, GGG) and $DyScO_3$ (DSC) ($7.5\ mm\ \times 7.5\ mm \times 0.5\ mm$), where the spin current generated in paramagnetic insulators is injected and detected through 5 nm thick Pt or W film ($100\ \mu m\ \times 10\ \mu m$) using ISHE [83]. They deposited 100 nm MgO on top of Pt or W to electrically isolate the LSSE sample from 50 nm thick Au heater deposited on top of MgO as shown in the Figure 2.5 (d) [83]. They used lock-in amplifier to the detect second harmonic response across the Pt or W layer by Joule heating the Au layer passing sinusoidal electric current at first harmonic. Also, the LSSE response are opposite in direction for W and Pt spin current

detector as shown in the Figure 2.5 (e) and (f) respectively, because their spin Hall angles have opposite sign [83]. Also, the W sample shows very large response as compared to Pt sample because their deposited W film has 11 times larger electrical resistivity compared to Pt film [83]. Tian, D., *et. al.* use LSSE device configuration with 120 nm thick YIG as a spin current source on GGG substrate, and inject the spin current to 2 nm thick Co thin film acting as a spin current detector, where spin current is converted to charge current by ISHE, separated by 5 nm Cu spacer film to decouple ANE and SSE response [84].
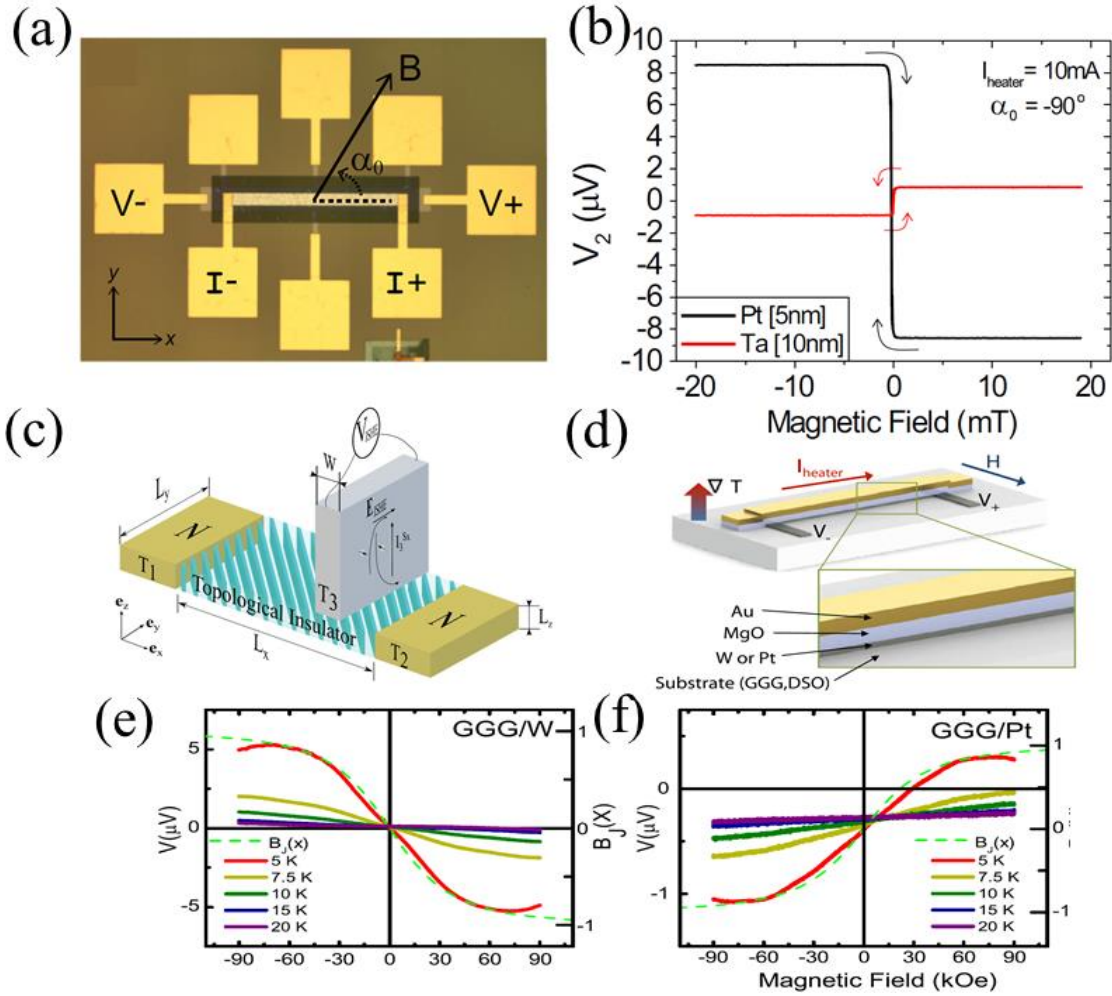
Figure 2.5 (a) Microscope image of Hall bar structure of sample Pt/YIG and Ta/YIG for SSE and SMR measurement where sample is electrically insulated by Al_2O_3 film from Pt heater on top. The experimental contacts are as shown on block and applied field is rotated with angle α_0. (b) Second harmonic voltage from SSE effect as a function of applied magnetic field when $\alpha_0 = -90°$ and heater current is 10 mA. Reprinted by permission from ref [82], © 2014. (c) TSSE device structure for 3D topological insulator Bi_2Se_3 where quintuple layers are set an angle of 45° wrt to the direction of electron propagation ($x - axis$). Reprinted by permission from ref [65], © 2014. (d) Schematic of LSSE device with Joule heating method. Second harmonic response from LSSE as a function of applied magnetic field at different temperatures in W (e) and Pt (f). The dashed curve shows Brillouin function for S = 7/2 paramagnet at 5K is overlaid. Reprinted by permission from ref [83], © 2015.

Wu, S. M., *et. al.* observed LSSE in Pt (4 nm) / MnF$_2$ (30 nm) bilayer thin film structure where MnF$_2$ is grown on MgF$_2$ substrate. The longitudinal temperature gradient across the bilayer is generated using 50 nm thick Ti layer, electrically isolated from bilayer sample using 100 nm MgO spacer layer [21]. The spin Seebeck coefficient is calculated at 15 K and 14 T about 41.2 µV/K [21]. Jiang, Z., *et. al.* detected LSSE in $(Bi_xSb_{1-x})_2Te_3$ / YIG bilayer heterojunction [29]. They used magnetic insulator YIG is a spin current source and topological insulator $(Bi_xSb_{1-x})_2Te_3$ as a spin current detector using topological insulator surface states [29]. Li, J., *et. al.* implemented LSSE device configuration to measure the SSE response in antiferromagnetic thin film FeF$_2$ of 50 nm thick deposited on MgF$_2$ substrate, detected by 5 nm thick Pt thin film using ISHE [85]. Ito, N., *et. al.* observed LSSE in ferromagnetic insulators CrSiTe$_3$ and CrGeTe$_3$ and detected using Pt thin films [86]. Akopyan, A., *et. al.* observed LSSE in helimagnetic insulator Cu$_2$OSeO$_3$, detected by Pt contacts [23].

As seen in the literature review above, generally heavy metals such as Pt, W and Ta with large spin orbit coupling are used for conversion of spin current to charge current. The SSE is enhanced due to phonon drag, and phonons drive spin distribution [71, 87]. The spin-phonon coupling can provide an able platform to engineer spin dependent thermoelectric conversion. To make the spin mediated thermoelectric energy conversion

into reality, we need to discover earth abundant material/interfaces for giant SSE/ANE/SNE and efficient spin to charge conversion.

Interfacial spin to charge conversion arises due to an electric potential perpendicular to the interface. The electric potential can be artificially induced, for example, using ferroelectric and piezoelectric thin films at the interface. An alternate way to induce the electric potential could be flexoelectric field. The flexoelectricity can be observed in all the material that either have or lack inversion symmetry, additionally no large gate bias is needed. Structure inversion asymmetry (SIA) at interfaces give rise to Rashba spin-orbit coupling (SOC), which is being extensively investigated for various spintronics devices [88, 89]. The spontaneous polarization due to applied strain gradient will give rise to an electric field normal to interface, this phenomenon is known as flexoelectric effect. This normal electric field will give rise to Rashba SOC and leads to large spin to charge conversion especially at semiconductor interfaces. For a uniform strain gradient, the flexoelectric field can be written as:

$$E_l = \frac{\mu_{ijkl}}{\varepsilon} \frac{\partial \epsilon_{ij}}{\partial x_k} \tag{7}$$

Where $\frac{\partial \epsilon_{ij}}{\partial x_k}$, μ_{ijkl} and ε are strain gradient, flexoelectric coefficient and dielectric constant, respectively. Hence, the flexoelectric field will give rise to interfacial Rashba SOC [90] at the interface, which can be written as:

$$H_R \propto (\vec{E} \times \vec{p}) \cdot \vec{\sigma} = E_z(-p_y\sigma_x + p_x\sigma_y) = \frac{\mu_{xx,zz}}{\varepsilon} \frac{\partial \epsilon_{xx}}{\partial x_z}(-p_y\sigma_x + p_x\sigma_y) \tag{8}$$

where $\vec{p}$ and $\vec{\sigma}$ are momentum and spin polarization vectors, respectively. While the flexoelectric polarization is very weak in bulk centrosymmetric materials, it can be orders of magnitude larger in nanoscale materials and at interfaces [91-93]. The flexoelectric effect could also lead to charge separation, increasing the charge carrier density in the two-dimension electron gas system (2DES) at the interface. The combined effect of strain [94], strain gradient and charge separation [95] in doped semiconductors will lead to an interfacial 2DES with strong Rashba SOC. Unlike the Rashba SOC in thin metallic film structures, the flexoelectric field driven Rashba SOC can be controlled by changing the strain gradient.

Chapter 3

Experimental Details

In this chapter a brief introduction about the thin film fabrication methods, experimental and characterization techniques used in the research project is provided. The fabrication of thin films is done by using conventional Micro Electromechanical Systems (MEMS) fabrication procedure at Center for Nanoscale Science and Engineering (CNSE) nanofabrication facility of University of California Riverside (UCR) which is class 100 in photolithography and class 1000 in thin film/etching area. A class 100 and class 1000 clean room is the space that maintains less than 100 particles and 1000 particles larger than 0.5 μ in each cubic foot of air space The bilayer thin film device fabrication is conducted on commercially available silicon wafers using lift off photo lithography, DC/RF magnetron sputtering, Plasma Enhanced Chemical Vapor Deposition system (PECVD) and E-beam evaporation methods.

The fabrication of the bilayer longitudinal SSE devices is done on 6-inch substrates. The oxide (SiO_2) layer between the substrate and the device is developed using PECVD system. The purpose of oxide layer is to create a heat sink for developing a temperature gradient along the device. After the deposition of SiO_2, the substrate surface is cleaned using acetone to remove organic impurities, then with isopropyl alcohol (IPA) to remove the residual particles and to allow quick dry of the surface without forming any spot, and then with deionized (DI) water which does not contain any charged particles or impurities.

This three-step substrate cleaning process is adopted every time during substrate cleaning while fabrication. After the cleaning, the substrate is heated for 1 minutes at 110°C to vaporize the water particles if remained on the substrate surface. To make pattern of LSSE's sample, oxide and heater layer, the optical lithography tool is used. Image reversal process using AZ 5214 photoresist is used as it is good for high resolution lift-off process because of formation of undercut after the material deposition. A photoresist works as a temporary mask for structuring steps.

Image reversal is a four-step process consists of exposure, baking, flood exposure and development. First, the AZ 5214 positive photoresist is coated on the top surface of the substrate and then baked for 1 minute at 120°C. The pattern is created by using the optical photolithography using the pattern mask which is the exposure step in image reversal process. This exposure step will make the exposed area of photoresist soften due the formation of carboxylic acid. Then, the substrate is baked at 110°C around 2 minutes until the patter got visible on the substrate surface. This baking step crosslink the previously exposed area which will prevent the thermal softening of resist profiles. Next, the photoresist surface is fully exposed under the ultraviolet (UV) light without the mask of the optical photolithography tool which is generally known as flood exposure. In the flood exposure step, the exposed area (which is all area) gets soften while the previously crosslinked area remains crosslinked. In the last step of image reversal process, which is the development process, the substrate is soaked into inorganic developer which are either sodium or potassium based. We use AZ 400K potassium-based buffer developer because it provides minimum contamination, high contrast, and optimal process control. We diluted

the developing solution as 1:4 with DI water. After the development process, the patterned

is obtained on the substrate's top surface. The complete fabrication process is as shown in

the Figure 3.1.
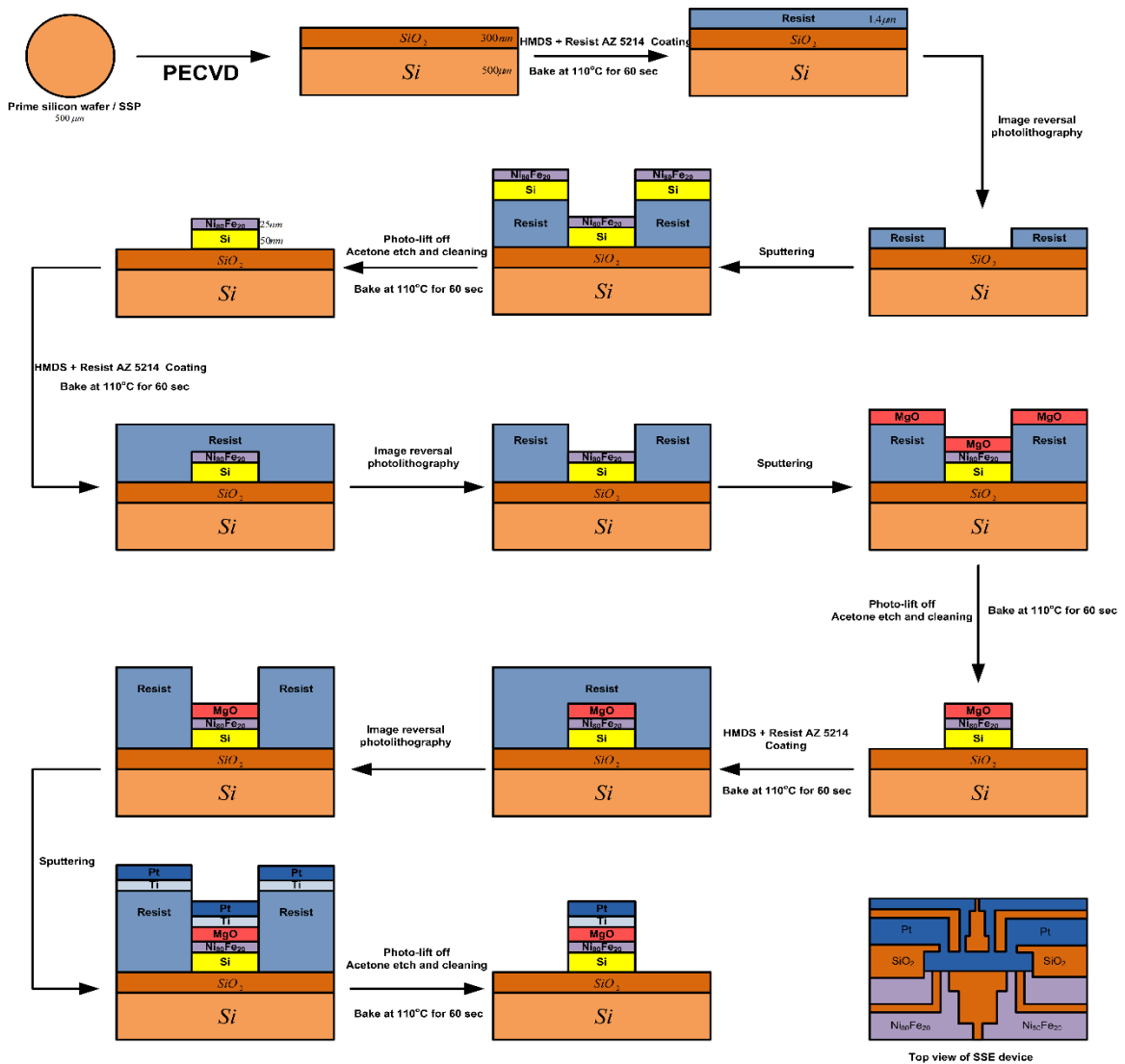
Figure 3.1 Schematic showing the complete fabrication process of longitudinal spin Seebeck device

The material deposition on the obtained pattern is done by using DC/RF magnetron sputtering and E-beam evaporation methods. During the bilayer sample deposition, the vacuum is maintained to avoid any contamination or oxidation of the thin film. After the deposition of LSSE sample material, the unnecessary area containing the photoresist and deposited material is removed using lift off process. The lift off process is done by soaking the material deposited substrate into the acetone bath for an hour. But it is found that due to high residual stresses, the heater film of Pt gets delimited. Thus, the lift off process for future substrates is done using remover PG and then the Pt heater film remains laminated onto the adjacent heater (MgO) thin film. The high vapor pressure of acetone might be a reason along with the residual stress that caused the delamination of thin films.

We developed an experimental setup to measure the longitudinal SSE. In the experimental setup, we use a Pt heater to create the temperature gradient across the $Ni_{80}Fe_{20}$/a-Si bilayer specimen as shown in Figure 3.2 (a). In the LSSE configuration, the temperature gradient across the thin film specimen creates a spin current (J_s), which then get converted into a charge current (J_c). An AC bias across the Pt heater creates the temperature gradient. We measure the first harmonic and the third harmonic response across the heater to quantify the temperature gradient between the heater and the Si substrate. The SSE, ANE, and SNE are measured from the second harmonic response across the $Ni_{80}Fe_{20}$/a-Si bilayer specimen. We use the micro/nanofabrication techniques to make the experimental setup as shown in Figure 3.2 (b). To fabricate the experimental setup, we take a Si wafer and deposit silicon oxide using plasma enhanced chemical vapor deposition (PECVD). We, then, deposit the $Ni_{80}Fe_{20}$/a-Si bilayer (blue color) by RF

sputtering as shown in Figure 3.2 (b). The a-Si target is Boron doped having a resistivity in the range of 0.005–0.01 Ω cm. We sputter 50 nm MgO (green color) to electrically isolate the heater and the specimen. We then deposit Ti (10 nm)/Pt (100nm) (pink color), which acts as a heater.
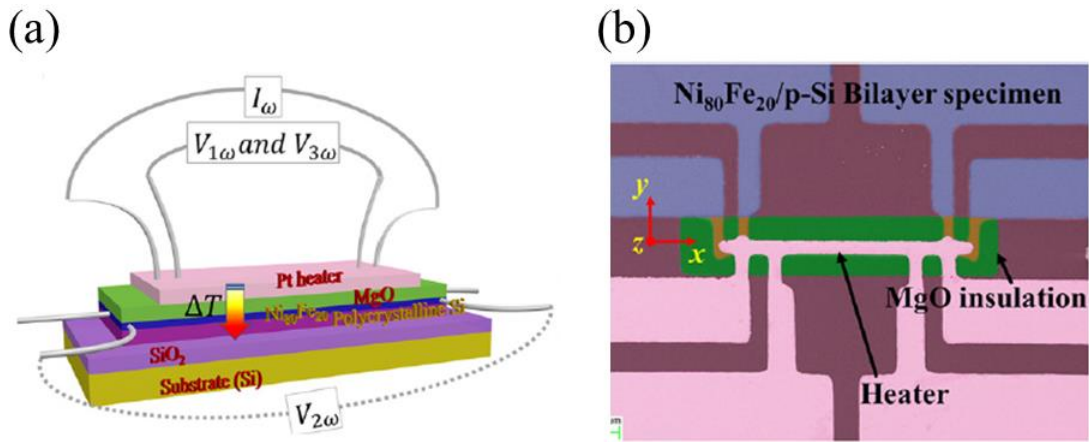
Figure 3.2 (a) The schematic of the experimental setup for the LSSE measurement, (b) the false color SEM micrograph showing the device structure

For subsequent strained and unstrained, bilayer LSSE devices, the fabrication process is discussed in brief in the respective chapters. Also, the device characterization using physical property measurement system (PPMS) for characterizing thermal and electrical properties, atomic force microscopy (AFM) for surface roughness measurement, scanning electron microscopy (SEM) for capturing high resolution images, transmission electron microscopy (TEM) for capturing high resolution layered structure of the experimental specimen, and energy dispersive X-ray spectroscopy (EDXS) to elemental map the thin film layers and interfaces are discussed in brief in the respective chapters.

36

Chapter 4

Spin Seebeck Effect in $Ni_{80}Fe_{20}$/amorphous-Si bilayers

4.1 Introduction

The thermoelectric energy conversion from spin current depends on efficient spin to charge conversion. Currently, the primary material for spin to charge conversion is Pt due to its large spin Hall angle, which inhibits the further scientific research in spin thermoelectric conversion behavior. In this chapter, we report the experimental measurement of the giant SSE in the $Ni_{80}Fe_{20}$/a-Si bilayers. The spin-phonon coupling in a-Si leads to giant enhancement in the SSE at the $Ni_{80}Fe_{20}$/a-Si bilayers bilayer, and SHE in a-Si leads to giant spin-orbit torque (SOT), which can be used for SOT based memory applications.

4.2 Methods

We used MEMS fabrication technique to fabricate the $Ni_{80}Fe_{20}$/a-Si bilayer LSSE device. The longitudinal SSE device fabrication method is already explained in the chapter 3. To fabricate the experimental setup, we take a Si wafer and deposit 300 nm of silicon oxide using plasma enhanced chemical vapor deposition (PECVD). The experimental

measurement is carried inside a quantum design physical property measurement system (PPMS).

4.3   Results

For energy conversion applications, the thermoelectric behavior should be robust at higher temperatures. We applied a heating current in the range of 20mA–5Hz across the outer two electrodes of the Pt heater starting at 400K. We then measured the second harmonic response as a function of the applied magnetic field in the z-direction and the y-direction as shown in Figure 4.1(a). For the magnetic field in the y-direction, the field is perpendicular to the direction of the temperature gradient, we observe a large second harmonic response, which may be related to the ANE/SSE. However, we observe an equally large signal when the magnetic field is applied along the z-direction (field parallel to the temperature gradient). The $Ni_{80}Fe_{20}$ thin films have an in-plane magnetic easy axis and an out-of-plane hard axis [96, 97], which are verified from the magnetoresistance measurement as shown in Figure 4.2 (a) and the anisotropic magnetoresistance (AMR) in Figure 4.2 (b). The second harmonic response in the z-direction is attributed to the hard axis magnetization. We, then, measured the second harmonic response as a function of heating power at 400K as shown in Figure 4.1 (b). We observe a linear relationship between the heating power and the second harmonic response [29] as expected.
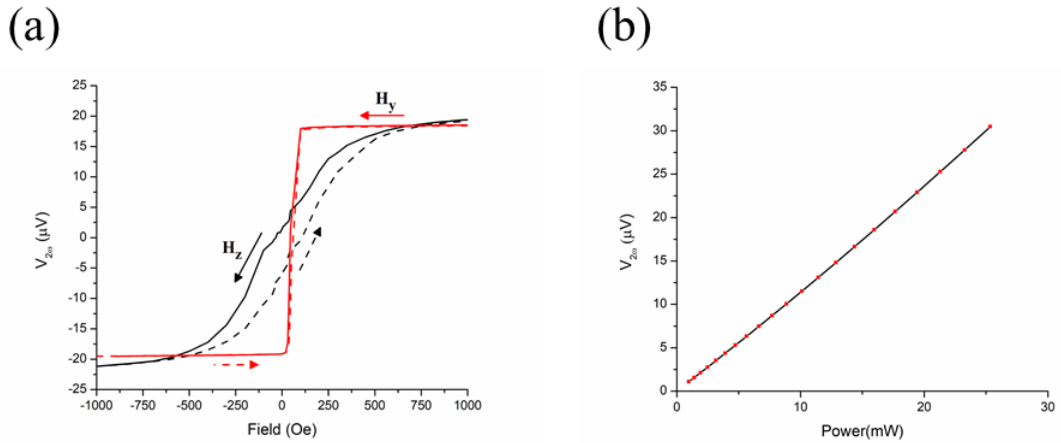
Figure 4.1 (a) the second harmonic response for the applied magnetic field in transverse in-plane (y-direction) and out of plane (z-direction) directions, and (b) the second harmonic response as a function of heating power for an applied magnetic field of 1000 Oe (z-direction).
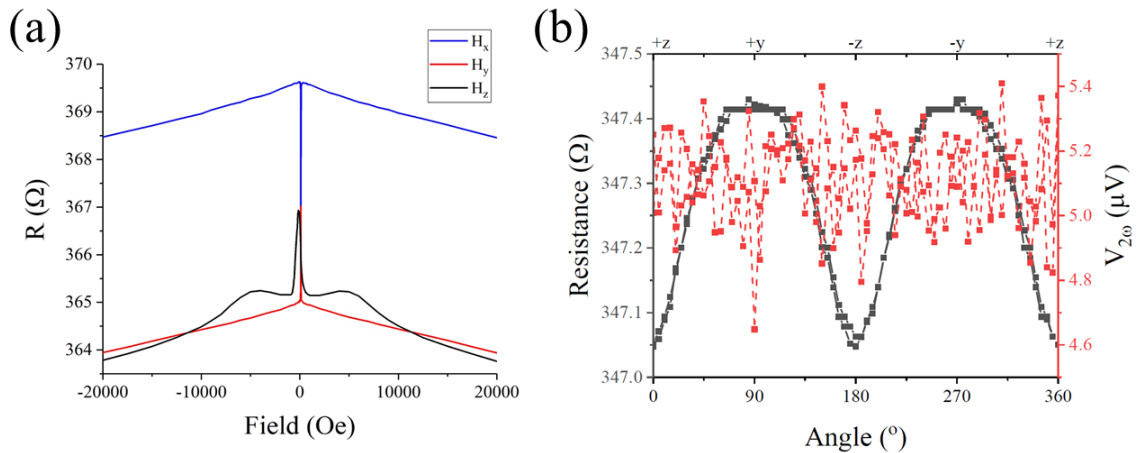
Figure 4.2 (a) The magnetoresistance measurement showing the easy and hard axis (z-direction) of the Ni80Fe20 thin film. The out of plane (z-direction) saturation magnetization is approximately 1.25 T. (b) The resistance and second harmonic response of the bilayer specimen for angular rotation of magnetic field in the yz-plane.

We then measured the second harmonic responses as a function of the magnetic field (from 1000Oe to -1000 Oe) and applied current in the range of 15mA to 50mA at

300K as shown in Figure 4.3 (a-d). We observe a linear second harmonic response (comprising ANE and SSE) as a function of heating power. Surprisingly, we observe that the magnetic hysteresis of the second harmonic response for the field along the z-direction collapses as the heating current is increased to 50mA. At a heating current of 30mA at 300K, we estimate the increase in temperature in the heater to be ~20.84K from the third harmonic measurement. This led us to believe that the observed collapse of hysteresis for the z-direction at 300K cannot arise due to the heating effect only since the collapse of hysteresis in the z-direction is not observed at 400K. This behavior indicates the existence of additional spin current from a-Si to the $Ni_{80}Fe_{20}$ layer. This additional spin current leads to spin-orbit torque and the resulting change in the hysteresis behavior. For the magnetization perpendicular to the plane of the interface, ANE and SSE will not be observed since $M \parallel \Delta T$ and $J_s \parallel \sigma$, respectively.
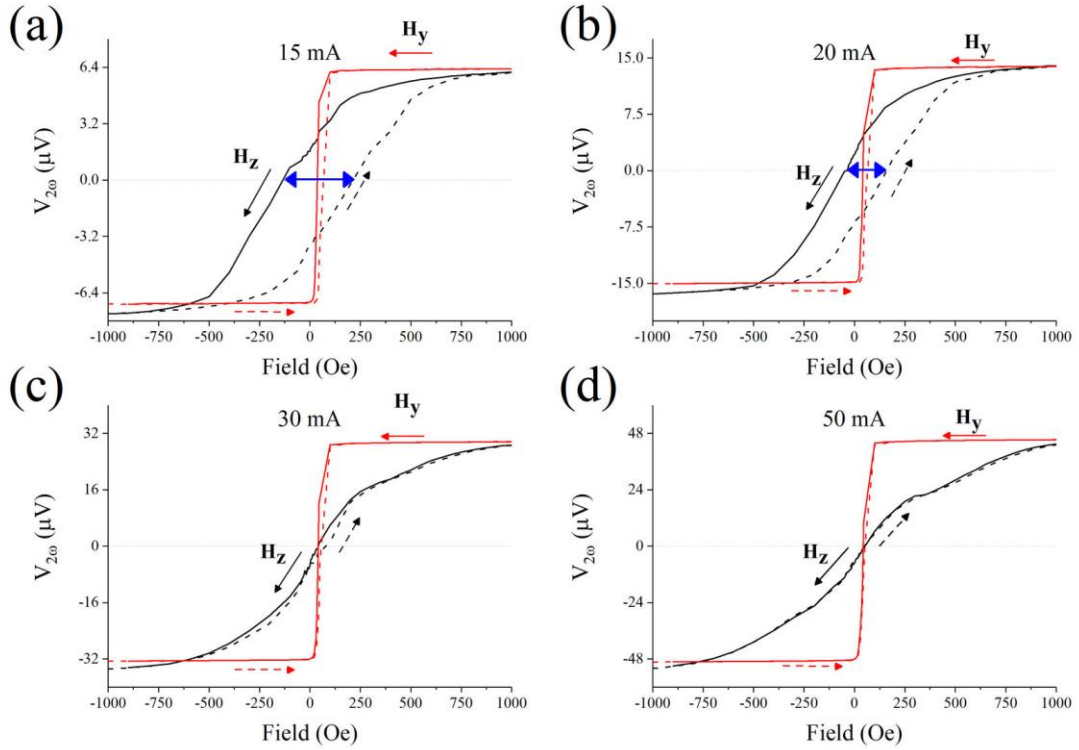
Figure 4.3. The second harmonic response related to the SSE as a function of the magnetic field applied along the y-direction and z-direction at 300K for heating currents of (a) 15 mA, (b) 20 mA, (c) 30 mA, and (d) 50 mA. Arrows show the direction of magnetic field sweep

In order to decouple the contributions of ANE and SSE and to discover the origin of SOT, we measured the second harmonic response for an applied magnetic field (2 T) rotated in the xy, zy, and zx planes as shown in Figure 4.4 (a), where the temperature gradient is along the z-direction. We observe a sine behavior attributed to the SSE in the xy-rotation. The angular dependence in the zx-plane is observed to be cosine, and the zy-plane shows combined sine and cosine behavior. These measurements led us to believe that there is a second thermoelectric effect in the bilayer thin films that is giving rise to the

41

cosine second harmonic response in addition to the out of plane magnetic field dependent behavior reported in Figure 4.4 (a). This cosine behavior is like the ANE response but for now we will call it as transverse spin dependent response. The thermal ANE, in this study, will lead to charge current across the bilayer specimen, causing the second harmonic response. We would like to state that the ANE coefficient in $Ni_{80}Fe_{20}$ is extremely small [4.8 nV/K] [98]. In addition, the specimen size in our measurement is 160 µm $\times$ 12 µm, which is relatively very small as compared to the sample area for the ANE measurements reported [98, 99]. The ordinary Nernst effect (ONE) is not considered in this study because the ONE does not give rise to the switching behavior observed in this work. These measurements lead to two challenges in the interpretation of the results. First, the SSE measurement requires the inverse spin-Hall effect (ISHE) to convert the spin current into voltage. While the SHE has been reported in Si the spin-Hall angle of Si is negligible and may not lead to the observable signal [100, 101]. To address the first challenge, we hypothesize that the ISHE occurs due to Rashba spin orbit coupling at the $Ni_{80}Fe_{20}$/a-Si interface.

The second challenge is to uncover the origin of SOT observed in this study. As stated previously that cosine behavior is attributed to the unknown transverse spin dependent response that may be anomalous Nernst effect (ANE), which causes the second harmonic response, while the magnetization and temperature gradient are parallel to each other. However, this behavior should not lead to SOT observed in Figure 4.4.
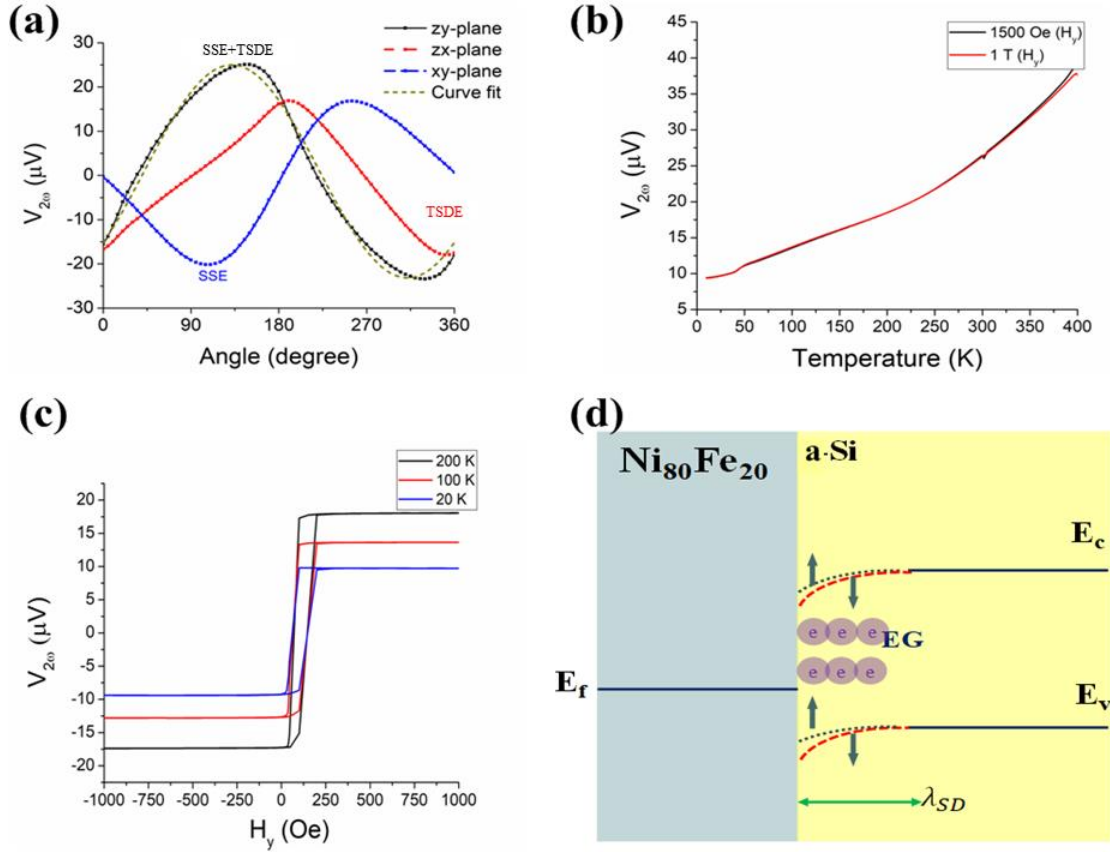
Figure 4.4 (a) The second harmonic response as a function of angular rotation of the constant magnetic field of 2 T in the xy, zx, and zy-planes and curve fitting showing a combined sine (SSE) and cosine (SOT) behavior; (b) the second harmonic response as a function of temperature between 400K and 10K at applied magnetic fields of 1000 Oe and 1 T; (c) the second harmonic response as a function of the magnetic field at 200 K, 100 K, and 20 K; and (d) the schematic showing the electron gas at the Ni80Fe20/a-Si interface (λ_{SD} is the spin diffusion length).

We propose a twostep process that will lead to SOT observed in this study. The first step is transverse spin dependent response (TSDE) where tunneling of spin polarized electrons across the interface in the z-direction, having polarization in the z-direction as well, leads to charge current parallel to the interface in the x-direction due to the inverse Rashba-Edelstein effect, which can be written as [102, 103]

$$J_c^x = \lambda_{TSDE} J_s^{z, \sigma_z} \tag{9}$$

where λ_{TSDE} is the "effective thickness" of the spin orbit layer due to transverse spin dependent effect. Since the spin current is a function of the temperature gradient, this equation can be written as

$$J_c^x \propto \lambda_{TSDE}(T_{FM} - T_{Si}) \tag{10}$$

where T_{FM} and T_{Si} are the temperature of the ferromagnetic layer and temperature of the Si layer, respectively. The Rashba potential leads to spin precession, causing a projection of the polarization in the y-direction, which then leads to ISHE and charge current in the x-direction [102, 103]. The field like SOT acts along $\hat{m} \times \hat{\sigma}$, and damping like torque acts along $\hat{m} \times (\hat{m} \times \hat{\sigma})$, where $\hat{m}$ and $\hat{\sigma}$ are the unit vectors of magnetization and spin polarization, respectively [104]. For $\hat{m}$ acting in the z-direction, the spin polarization ($\hat{\sigma}$) vector has to be in the plane of the thin film for the SOT. In the second step, the interfacial charge current leads to SHE due to Rashba spin-orbit coupling, causing an inverse spin current from a-Si to the $Ni_{80}Fe_{20}$ layer having spin polarization in the plane of the thin film. The charge to spin conversion relationship can be written as

$$J_s^{z, \sigma_y} = \theta_{SHE} J_c^x \tag{11}$$

where θ_{SHE} is the spin-Hall angle. The spin current entering the $Ni_{80}Fe_{20}$ layer can be considered as magnetization entering and exiting the ferromagnetic layer, which will cause the spin orbit torque. The spin current causing the SOT can be related to the temperature gradient through the following approximate equation:

44

$$SOT \propto J_s^{z,\sigma_y} \propto \theta_{SHE}\lambda_{TSDE}(T_{FM} - T_{Si}) \tag{12}$$

The SOT characterization requires the application of electric current across the specimen and measurement of first and second harmonic Hall responses. In this study, the $Ni_{80}Fe_{20}$ thin film is two orders of magnitude more conducting than the a-Si layer. Hence, the SOT observed in this study is not quantifiable with current techniques since it is of thermal origin. However, the SOT leads to collapse of hysteresis in a 25 nm $Ni_{80}Fe_{20}$ thin film as compared to the few nanometer films used in the SOT studies [105-108], and only earth abundant materials are used. While we propose that the second harmonic response for the out-of-plane magnetic field is due to the Rashba effect mediated transverse spin dependent response, other mechanisms may also be present, which can lead to better understanding of the observed measurements.

Now, we needed to quantify the LSSE at the $Ni_{80}Fe_{20}$/a- Si interface. The efficiency of converting spin current voltage at the interface of the bilayer in a LSSE device is given by [109]

$$S_{LSSE} = \frac{E_{ISHE}}{\nabla T} = \frac{V_{ISHE}t_{FM}}{w_{NM}\Delta T} \tag{13}$$

where V_{ISHE} is the electric voltage measured due to ISHE by the paramagnetic metal or the normal metal (NM), t_{FM} is the thickness of the FM material, w_{NM} is the distance between electrical contact in NM, and ΔT is the temperature gradient across the sample. For thin film structures, the temperature gradient is difficult to find out. We estimate the temperature gradient between the heater and the substrate using the 3ω method, and the temperature gradient across the specimen is estimated using finite element modelling

45

(FEM) (COMSOL). The temperature gradient between the heater and far field temperature

using the 3ω method [110] is given by

$$\Delta T = \frac{4V_{3\omega}}{R'I_{rms}} \tag{14}$$

where $V_{3\omega}$ is the third harmonic response, R' is the resistance as a function of temperature,

and I_{rms} is the heating current. The measured R' is 0.07 Ω/K as shown in the Figure 4.5

(a). Using the 3ω method, we calculated the temperature gradient in the heater to be 4.98

K, 10.9 K, and 20.84K for heating currents of 15 mA, 20 mA, and 30 mA, respectively.

Using FEM, we estimated the temperature gradient across the specimen to be ~14.08 mK

corresponding to a heating current of 20 mA. For modeling the temperature gradient, we

assumed the $\kappa_{a-Si} = 25 \, W/mK$ [111, 112] and $\kappa_{Ni_{80}Fe_{20}} = 20 \, W/mK$ [113]. For the

temperature gradient, we calculated S$_{LSSE}$ to be ~0.355 µV/K. This value is significantly

higher than S$_{TSSE}$ reported for the Ni$_{80}$Fe$_{20}$ [59] thin film but lower than S$_{LSSE}$ [0.8 µV/K

[114]] reported for Ni$_{81}$Fe$_{19}$ thin films. It needs to be stressed that ISHE in this study is

interfacial, whereas all the other reported studies use Pt for spin to charge conversion. From

the S$_{LSSE}$ measurement in this study, we can deduce that $\theta_{SH}^{interfacial}$ is of the same order

as θ_{SH}^{Pt}. The calculated specimen temperature gradient is a function of κ_{a-Si}. We repeated

the calculation for $\kappa_{a-Si} = 25 \, W/mK$ and $30 \, W/mK$ as shown in the Figure 4.5 (b) and

(c), Table 4-1 and Table 4-2, and S$_{LSSE}$ is calculated to be 0.308 µV/K and 0.395 µV/K,

respectively.
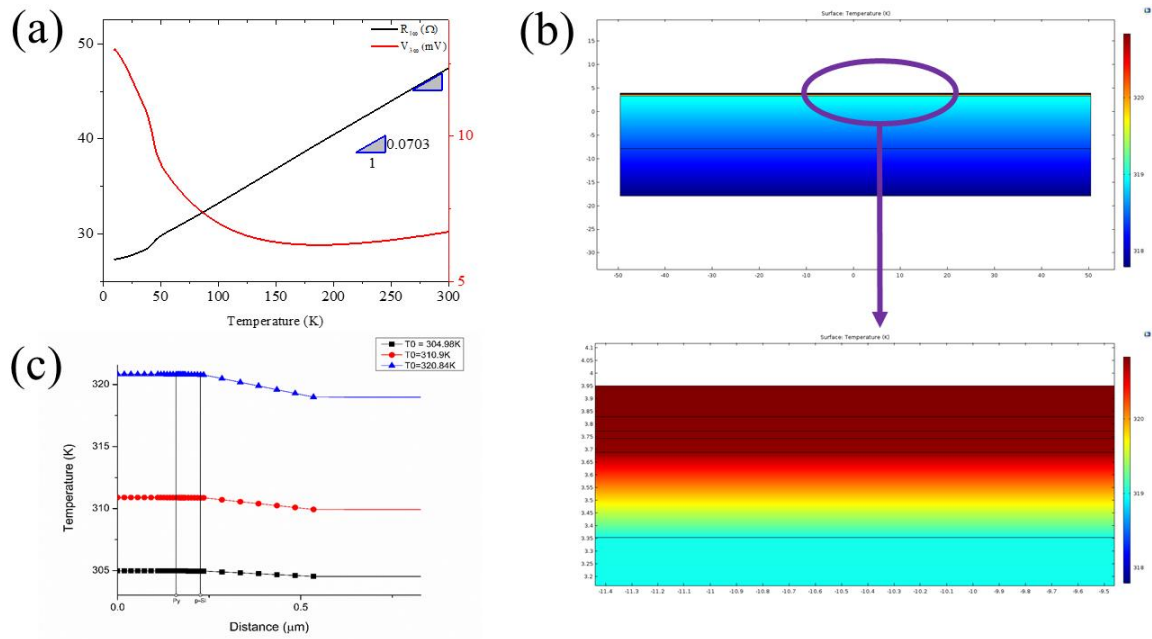
Figure 4.5. (a) The resistance and third harmonic response of Pt heater from 300 K to 10 K. The resistance data is used to fit and estimate $R' = \frac{dR}{dT}$. (b) The COMSOL model showing the temperature gradient between the heater and the substrate and the temperature gradient across the layered structure for 30 mA of heating current. (c) The temperature gradient across the specimen for heater temperatures corresponding to 15 mA, 20 mA and 30 mA of heating current.

Table 4-1 The properties used for the modelling

Material	Thermal conductivity (W/mK)	Density (Kg/m^3)	Specific heat (J/KgK)
Platinum	69.1	21450	130
MgO	30	3580	877
Py	19.6648	8740	502.415783

a-Si	22	2328	678
Si	130	2328	700
SiO$_2$	1.3 – 1.5	2650	680 – 730

Table 4-2 The effect of κ_{a-Si} on the temperature gradient across the specimen

Thermal conductivity (W/mK) of a-Si	Heater Temperature (T$_1$)	Temperature difference
20	304.98 K	0.00741716 K
	310.9 K	0.01623436 K
	320.84 K	0.03103890 K
25	304.98 K	0.00643506 K
	310.9 K	0.01408479 K
	320.84 K	0.02692908 K
30	304.98 K	0.00578012 K
	310.9 K	0.01265127 K
	320.84 K	0.02418830 K

Phonons from the sample and substrate are the primary component that governs the non-equilibrium state of metallic magnets (Py) whereas magnons and phonons are

responsible for non-equilibrium states in insulating magnets [115]. The SSE in semiconductors has been proposed to occur due to phonon drag but we observe a large SSE at 400K. In order to ascertain the effect of phonons, we measured the second harmonic response as a function of 1500 Oe and 1 T as shown in Figure 4.4 (b) for a second device. We do not observe effect of phonon drag and Si phonons in this measurement. We also measured the SSE at 200 K, 100 K and 20 K and the SSE is reduced gradually as the temperature is lowered as shown in the Figure 4.4 (c). From the temperature dependent study, we propose that the observed second harmonic response is attributed to the magnon mediated SSE. The second harmonic measurement shows reduction as a function of temperature as expected for magnon mediated SSE, which further supports our assertion that observe behavior is SSE and not ANE.

From the experimental studies, we observe the SSE for transverse in-plane magnetic field and TSDE is observed for out of plane magnetization. The metal-semiconductor interface will lead to electron gas (EG) at the interface having thickness like the spin diffusion length as shown in Figure 4.4 (d). The charge potential in the EG gives rise to strong Rashba SOC, which is the underlying cause of SSE, TSDE and SOT observed in this study. The spin orbit coupling due to lack of inversion symmetry in Si metal-oxide semiconductor field effect transistor (MOSFET) has been reported using magneto-transport behavior in two-dimensional electron gas (2DEG) [116-119] and using spin resonance measurements [120]. This agrees with the proposed Rashba effect behavior hypothesized in this study for the specimen having ferromagnetic metal-Si interface. The structure inversion asymmetric interface and intrinsic SOC are the essential requirements

for strong Rashba SOC. In this study, large intrinsic SOC in $Ni_{80}Fe_{20}$ [121] may give rise to the strong Rashba SOC as shown in Figure 4.4 (d) [122, 123]. This hypothesis is further supported by observation of the strong Rashba spin split states at Bi/Si(111) interface [124]. In addition, the Rashba SOC mediated spin-Hall magnetoresistance has been reported in $Ni_{81}Fe_{19}$/MgO/p-Si thin films [125] and in n-Si [126]. The mechanistic explanation of the observed behavior is given in Figure 4.6. For the in-plane transverse magnetic field, the temperature gradient will generate a spin current leading to SSE at the interface as shown in Figure 4.6 (a). While the out of plane magnetization will lead to spin accumulation causing a charge current across the interface due to transverse spin dependent response. This charge current leads to SHE and resulting SOT observed in this study as shown in Figure 4.6 (b) [127]. We would like to stress that the transverse spin dependent response behavior may originate due to currently unknown mechanism as well, maybe ANE. Further experimental and simulation work is needed to develop mechanistic understanding of the behavior as well as the Rashba SOC responsible for it.
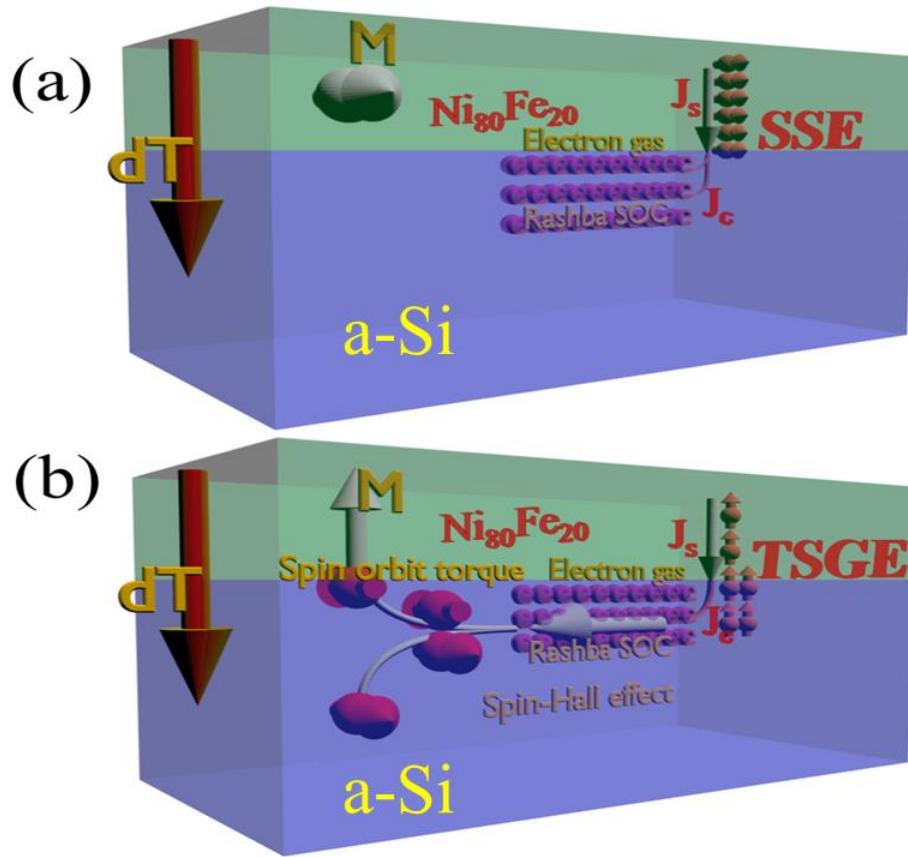
Figure 4.6 (a) The schematic showing the mechanism of spin-Seebeck effect and (b) The transverse spin dependent response mediated thermal spin-orbit torque observed in this study.

4.4   Conclusion

In conclusion, we observed giant spin-Seebeck effect and spin-orbit torques in $Ni_{80}Fe_{20}$/a-Si bilayer specimen. This measurement does not require any heavy metal for the spin to charge conversion. Instead, the inverse spin-Hall effect occurs at the $Ni_{80}Fe_{20}$/a-Si interface due to Rashba spin orbit coupling. The Rashba spin-orbit coupling is proposed to occur due to electron gas at the interface. The electron gas behavior can be controlled using the Si semiconductor physics developed over decades. This may allow Si interfaces with

giant spin-orbit coupling which may eclipse Pt as a primary spin detector. This may also lead to enhanced spin-Seebeck coefficient and in turn efficient thermal energy conversion. While the longitudinal spin-Seebeck coefficient measured in this study is similar to the values reported in literature but the room temperature V_{SSE} observed in this study is one of the largest reported values [60, 61, 76, 128] especially for a small temperature gradient of 10.9 mK across the interface. In addition to spin-Seebeck effect, the giant spin-orbit torque is also discovered, which is attributed to the transverse spin dependent effect or anomalous Nernst effect (ANE) due to thermal spin pumping. The thermal spin-orbit torques lead to collapse of out of plane magnetic hysteresis of 25 nm thick $Ni_{80}Fe_{20}$ film. The thermal spin-orbit torques can be used to develop energy efficient memory devices utilizing the magnetization reversal behavior. In addition, these results will give impetus to the interfacial behavior at light elements having insignificant intrinsic spin-orbit coupling. These results bring the ubiquitous Si to forefront of spintronics research and will lay the foundation of energy efficient Si spintronics and Si spin caloritronics devices.

Chapter 5

Giant Enhancement in Rashba Spin-Seebeck Effect in $Ni_{80}Fe_{20}$/amorphous-Si Thin Films

The spin-Seebeck effect mediated thermoelectric energy conversion can provide efficient alternative to traditional thermoelectric for waste heat recovery. To achieve this goal, efficient spin to charge conversion using earth-abundant materials is essential. Proximity induced Rashba effect arises from the charge potential mediated by structural inversion asymmetry, which has been reported in Si thin films and can be manipulated by controlling the thickness of Rashba layer. We demonstrate a giant Rashba spin-Seebeck effect in NiFe/a-Si bilayer thin films. The bilayer thin film specimens have a-Si layer thickness of 5 nm, 25 nm and 100 nm while keeping the NiFe layer thickness at 25 nm. The Rashba spin Seebeck coefficient has been estimated to be $0.266 \frac{\mu V}{K}$ for 100 nm a-Si, and increases by an order of magnitude to $2.11 \frac{\mu V}{K}$ for 5 nm a-Si. The measured spin-Seebeck coefficient in 5 nm a-Si specimen is one of the largest coefficients ever reported. The measured voltage of 100.3 µV is one of the largest reported spin-Seebeck voltage, with smallest area of ~ 160×10 µm^2 used in any spin-Seebeck measurement. This scientific and technological breakthrough using earth abundant elements brings the spin mediated thermoelectric energy conversion for waste heat recovery closer to reality.

5.1   Introduction

Pt is the primary material for spin to charge conversion due to its large SHA, which can be enhanced by defects and impurities. Extensive research has been reported in methods to enhance the spin-Hall angle for inverse spin Hall effect. These methods include alloying [129] and metastable phases [130, 131]. In the previous chapter, we reported SSE and transverse spin dependent response in $Ni_{80}Fe_{20}$/a-Si bilayer specimen without any heavy metal detector. In this chapter, we proposed that the spin to charge conversion in a-Si layer in the bilayer specimen is due to structure inversion asymmetry of sandwich structure and proximity effect. We observed that the spin-Seebeck coefficient in the bilayer is of the same order as Pt. However, larger values of spin Seebeck Coefficient (S_{LSSE}) is required to make the efficient spin mediated thermoelectric technologies into reality. The Rashba spin-orbit coupling (SOC) relies on the charge potential due to structure inversion asymmetry (SIA), which can be controlled by reducing the thickness of the sandwiched layer. The Rashba effect mediated spin-Hall magnetoresistance has also been reported in $Ni_{81}Fe_{19}$/MgO/a-Si [100, 101, 132] and $Ni_{81}Fe_{19}$/MgO/n-Si [133] thin films as well. The spin-Hall magnetoresistance arises due to ISHE, which is essential for SSE. We hypothesize the reduction in thickness of a-Si will increase Rashba SOC, leading to efficient spin to charge conversion. To explore the thickness dependent SSE behavior, we fabricated three specimen having a-Si layer thickness of 5nm, 25nm and 100nm while keeping the thickness of NiFe at 25 nm. In this chapter, we demonstrate giant enhancement in spin mediated thermoelectric energy conversion due to efficient spin to charge conversion from Rashba SOC.

5.2   Methods

In this work, we use the LSSE configuration to discover the spin mediated thermoelectric energy conversion behavior in NiFe/a-Si bilayers. To fabricate the experimental setup, we take a Si wafer and deposit 450 nm of thermal silicon oxide using chemical vapor deposition (CVD). We, then, deposit the NiFe/a-Si bilayers using the RF sputtering. We deposit three sets of bilayers with 5 nm, 25 nm and 100 nm of a-Si while keeping the NiFe thickness at 25 nm. We hide three quarters of the wafer and deposit each of the bilayer individually. We sputter 50 nm MgO to electrically isolate the heater and the specimen. We then deposit heater composed of Ti (10 nm)/Pt (100 nm). The insulator and heater deposition are common to all the bilayers devices, which reduces the fabrication induced measurement variations. We acquire experimental data inside a Quantum design Physical property measurement system (PPMS).

5.3   Results

To ascertain the thermal response characteristics, we acquire the second harmonic response as a function of current at an applied magnetic field of 1500 Oe as shown in

Figure 5.1. We observe that the $V_{2\omega}$ response shows a relationship having both quadratic and linear terms with respect to the applied heating current. This behavior suggests that the temperature rise across the specimen do not have linear relationship with the square of heating current, which may be due to temperature drop across MgO (top) and thermal oxide layers (bottom).To investigate the SSE behavior, we acquire the $V_{2\omega}$ response as a function of magnetic field (1500 Oe to -1500 Oe) applied in the y-direction

(normal to the temperature gradient) for all the three specimens. The data is acquired at 10 K, 100 K and 300 K as shown in Figure 5.2 (a)-(c). The observed behavior demonstrates the magnetic switching behavior for all the thicknesses, which is consistent with SSE and ANE. At 300 K, the $V_{2\omega}$ for the 5 nm, 25 nm and 100 nm are 100.3 µV, 36.77 µV and 31.08 µV, respectively. Although the $V_{2\omega}$ response for the 25 nm and 100 nm specimens is similar in magnitude but the magnitude of $V_{2\omega}$ response for 5 nm is extremely large. This behavior eliminates ANE as an underlying mechanism for the observed behavior since the NiFe layer thickness is same across all the specimens. For specimen with 5 nm a-Si layer thickness, the V_{SSE} is 100.3 µV at 300 K, which is significantly larger as compared to any other SSE measurement reported in the literature. In addition, the SSE specimen area is $160{\times}10$ µm^2 in this study, which is an order of magnitude smaller than the other reported experiments. Notable, this efficient spin mediated thermoelectric energy conversion is achieved without using any heavy metal for spin to charge conversion. This giant enhancement in SSE, presented in this study, is attributed to the proximity induced Rashba SOC in a-Si layer, which increases significantly with reduction in a-Si layer due to structure inversion asymmetry, resulting in the observed behavior. The Rashba SOC may also give rise to transverse spin dependent response. Here, we undertake a experiment to uncover the transverse spin dependent response. We measure the $V_{2\omega}$ response as a function of magnetic field (from -2500 Oe to 2500 Oe) applied in the z-direction (parallel to temperature gradient) at 300K for a heating current a 20 mA as shown in the Figure 5.2 (d). The observed $V_{2\omega}$ response is similar to SSE measurement. The $V_{2\omega}$ response in case of specimen having 5 nm a-Si layer is very large as compared to specimens having 25 nm

and 100 nm a-Si thick layer. We propose that this out of plane $V_{2\omega}$ response is due to transverse spin dependent response likely to be ANE.
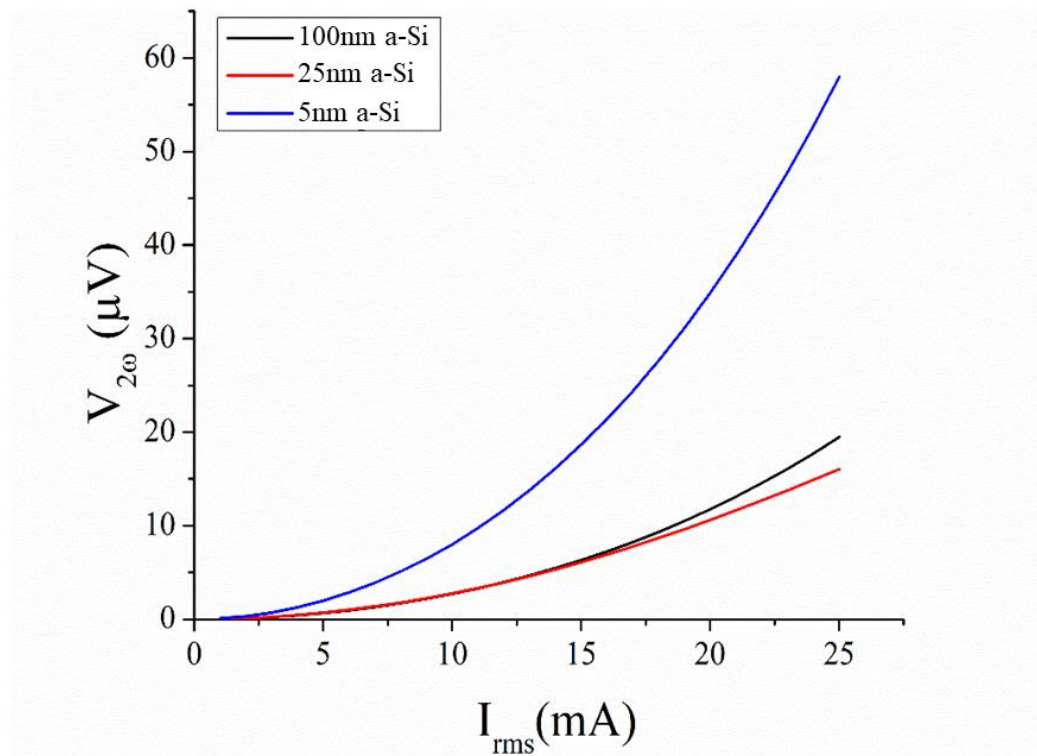
Figure 5.1 The second harmonic response as a function of heating current for an applied magnetic field of 1500 Oe
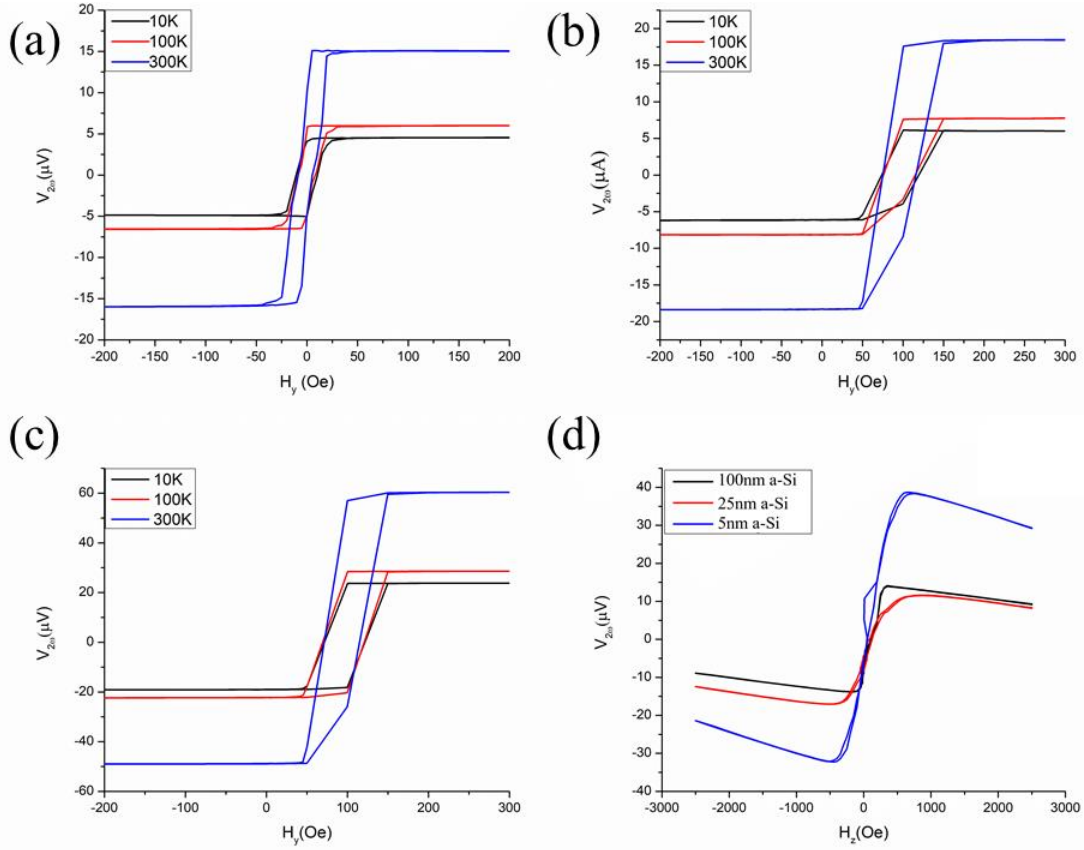
Figure 5.2 The longitudinal spin-Seebeck effect measurement for magnetic field applied along the y-direction at 300 K, 100 K and 10 K for the specimen having 25 nm of NiFe layer and a-Si layer thickness of (a) 100 nm, (b) 25 nm and (c) 5 nm, and (d) the transverse spin dependent effect measurement at 300 K for field applied along z-direction for specimen having a-Si layer thickness of 100 nm, 25 nm and 5 nm of a-Si.

The measurement of $V_{2\omega}$ response as a function of magnetic field leads to confirmation of the SSE and transverse spin dependent response. To uncover the underlying mechanism of SSE mediated energy conversion behavior, we measure $V_{2\omega}$ response as a function of temperature from 350 K to 10 K under a magnetic field of 1000 Oe applied along the y-direction. We observe a gradual decrease in the $V_{2\omega}$ response as the temperature is lowered to 10 K as shown in Figure 5.3 (a). The temperature dependent behavior signifies that the observed $V_{2\omega}$ response is due to spin polarized electrons and not

58

magnons [134], hence the SDSE was the underlying cause of the transverse spin dependent thermal response reported in this work. To further support our argument, we measured angular dependence of the $V_{2\omega}$ response for a constant applied magnetic field of 2 T rotated in the yx-plane. For all the specimens, we observe an embedded cosine behavior attributed to SSE as shown in the Figure 5.3 (b). The deviation from the cosine behavior can arise from the transverse spin dependent response.

To quantify the SSE in this study, we estimate the longitudinal spin Seebeck coefficient and using 3ω method the temperature gradient between heater and the far field substrate temperature is calculated. The heater temperature is estimated to be ~313.7 K for bilayer specimen having 25 nm a-Si layer and 313.4 K in case of 100 nm a-Si specimen for R' of 0.07 Ω/K [46]. We use finite element method (FEM) (COMSOL software) to simulate the temperature gradient across the bilayer specimen, which is essential for spin-Seebeck coefficient. For modeling the temperature gradient, we assumed the κ_{a-Si} to be 15 W/mK, 20 W/mK and 35 W/mK [112, 135] for thickness of 5 nm, 25 nm and 100 nm respectively and κ_{NiFe} to be 20 W/mK [113].
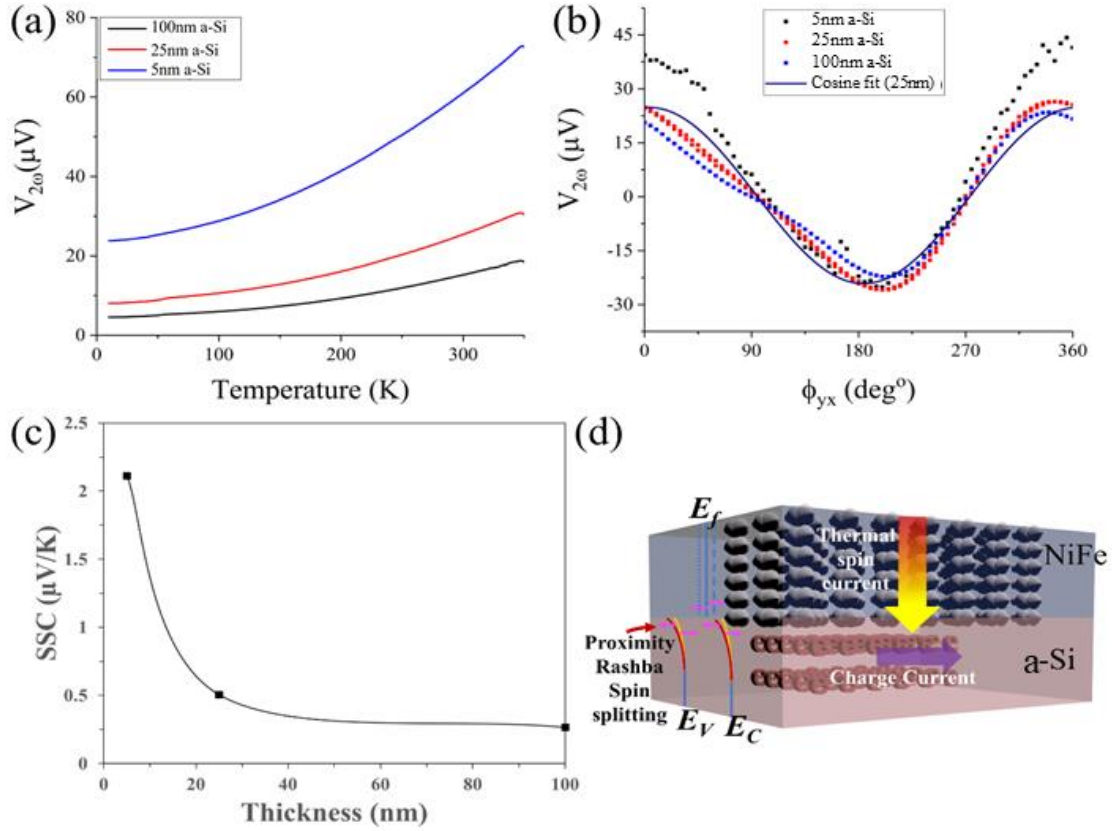
Figure 5.3 The spin-Seebeck voltage response for bilayer specimen having a-Si layer thickness of 100 nm, 25 nm and 5 nm (a) as a function of temperature from 350 K to 5 K, (b) angular dependence in the yx-plane for an applied magnetic field of 2 T, (c) the calculated spin-Seebeck coefficient as a function of thickness, and (d) schematic of the proposed mechanism for the observed behavior showing proximity Rashba spin splitting and resulting spin to charge conversion.

We observe that simulated temperature gradient across the NiFe layer is similar for all the a-Si layers. This observation reinforces that the ANE is not the underlying reason of observed $V_{2\omega}$ response. Using the simulated temperature gradient across the bilayer, the S_{LSSE} is calculated to be $2.11 \frac{\mu V}{K}$, $0.506 \frac{\mu V}{K}$ and $0.266 \frac{\mu V}{K}$ for 5nm, 25nm and 100nm thick a-Si layer thickness respectively as shown in Figure 5.3 (c). As stated earlier, the observed SSE behavior is proposed to occur due to proximity Rashba SOC. The Figure 5.3 (d) shows

the mechanism of the observed Rashba SSE behavior. Using ARPES measurement, Gierz et al. [136] demonstrated giant spin-splitting at the Bi/Si (111) interface, which is ascribed to structural inversion asymmetry or Rashba effect. This Rashba energy of 140 meV is reported, which is larger than any other semiconductor heterostructure. In addition, anisotropic electronic band structure is reported for Si (110) using ARPES and simulations [137]. These measurements support our hypothesis. This study includes a ferromagnet having large spin-orbit coupling [121, 138], which will introduce in-plane Rashba spin spitting in addition to lifting the degeneracy of band structure due to ferromagnetic proximity effect as show in Figure 5.3 (d). While Rashba SOC can give rise to giant spin to charge conversion, it may not give rise to ISHE essential for SSE observe in this study. But, Rashba SOC can lift the degeneracy of electronic band structure. The splitting of band structure due to Rashba SOC and ferromagnetic proximity effect can give rise to ISHE. We propose that a combined effect Rashba SOC and ferromagnetic proximity effect leads to the observed giant SSE response in this study. Since, we observe SSE in a-Si layer having thickness of 100 nm, the resulting behavior cannot arise from the two-dimensional electron gas only. The proposed Rashba SOC is bulk, which is consistent with recent reports on Si [132, 133, 139]. With the reduction in a-Si layer thickness, the Rashba SOC will increase and in turn SSE response, which is supported by our measurements.

The thickness dependent LSSE measurement can be used to calculate the spin-Hall angle and spin diffusion length. Qu et al. [140] used the LSSE measurement to uncover the spin-Hall angles using the following equation,

$$\Delta V_{th} \, or \, V_{SSE} = [2CL\Delta T][\rho(t)\theta_{SH}][\frac{\lambda_{SF}}{t}\tanh\left(\frac{t}{2\lambda_{SF}}\right)] \tag{15}$$

where ΔV_{th} is the thermal voltage due to SSE, the first factor on the right-hand side $[CL\Delta T]$ relates to spin injection efficiency, the length of the wire, and temperature gradient respectively. The second factor on the right-hand side $[\rho(t)\theta_{SH}]$ material specific quantity and relates to the spin conductivity. The last factor relates to the spin diffusion length (λ_{SF}) and thickness (*t*). Note that the equation (20) assumes that the intrinsic spin diffusion length and spin-Hall angle are independent of material thickness. Although this assumption may be true for the intrinsic spin orbit coupling in case of 5d heavy metals [129, 140] but the Rashba SOC that is responsible for the ISHE is thickness dependent. Hence, the equation (20) cannot quantify the spin transport behavior in NiFe/a-Si bilayer thin films presented in this work.

Instead of quantitative analysis, we undertake a comparative study of the observed SSE in NiFe/a-Si bilayer specimen. We analyzed the reported LSSE measurement over the years for various materials. To demonstrate the quantum of spin-Seebeck behavior observed in the present study, we list the reported $V_{SSE} > 10 \, \mu V$ in Table 5-1, where three articles report spin-Seebeck voltage of more than $100 \, \mu V$ [128]. Jiang et al. reported a spin-Seebeck voltage of $175 \, \mu V$ in Bi doped topological insulator (Sb_2Te_3), which is probably the highest V_{SSE} reported in the literature [141]. While the V_{SSE} reported in present study is smaller, but the area of the specimen in present study is ~56.25 times smaller as well. In addition, the heating power used to achieve the $175 \, \mu V$ is 500 mW whereas the heating power of 17.6 mW is used in this study to generate $100.3 \, \mu V$. This observation clearly

demonstrates the superiority of the thermoelectric efficiency in the NiFe/a-Si bilayer system. Lin et al. [142] demonstrated a similar V_{SSE} with NiO spacer in between YIG and Pt. They also report the highest SSC of 6 µV/K. The SSC is proportional to the thickness of the FM layer (YIG), which is 500 µm in this reported study. In addition, the specimen area is three orders of magnitude larger as compared to present study. Ramos et al. demonstrated a giant spin-Seebeck voltage in Fe_3O_4/Pt system using a spin-Hall thermopile setup. But the specimen area is 3 orders of magnitude larger than the specimen area in this study. In addition, the spin-Hall thermopile configuration can be applied to NiFe/a-Si bilayer system as well to achieve even higher voltages. We have listed other reports of large spin-Seebeck voltage. All specimens in the listed studies consist of areas that are three orders of magnitude larger, with spin-Seebeck voltages that are an order of magnitude smaller than presented in this work.

Table 5-1. The summary of largest spin-Seebeck voltages and corresponding spin source, spin detector, specimen dimensions and spin-Seebeck coefficient.

$\Delta V(\mu V)$	Spin source	Detector	Specimen (L × B)	SSC ($\mu V/K$)	Dimensional Normalization	Ref.
~175	YIG	$(Bi_xSb_{1-x})_2Te_3$	900 µm × 100 µm	Not reported	N/A	[128]
~175	YIG	Pt/NiO	7 mm × 2 mm	6	Yes	[142]
100.3	NiFe	a-Si	160 µm × 10 µm (smallest)	0.2-2.2	Yes	This study
~100	Fe_3O_4	Pt	Spin-Hall thermopile (7 mm × 2 mm)	Not reported	N/A	[141]

~26	YIG	Pt	6 mm × 2 mm	0.100	No	[76]
~25 and ~12	Fe_3O_4	Pt	7 mm × 2 mm	0.03 and 0.7	Yes	[58, 143]
~18	YIG	Pt	10 mm × 2.3 mm	1.500	No	[144]
~12	$NiFe_2O_4$	Pt	8 mm × 5 mm	0.030 − 0.020	No	[145]

5.4   Conclusion

In conclusion, we report a giant increase in SSE in NiFe (25 nm)/a-Si bilayer specimens having a-Si thickness of 5 nm, 25 nm and 100 nm. The spin-Seebeck voltage shows a three-fold increase in case of 5 nm a-Si specimen as compared to the 25 nm and 100 nm a-Si specimens. The inverse spin-Hall effect is proposed to occur due to proximity induced Rashba spin orbit coupling at the NiFe/a-Si interface. This observation eliminates the requirement of heavy metal (Pt or Ta) for spin to charge conversion. The largest spin-Seebeck coefficient reported in this study is a technological breakthrough, which may help in realization of waste heat recovery applications using spin-Seebeck effect.

Chapter 6

Strain Engineering of Spin-to-Charge Conversion at amorphous-Si Thin Film Interfaces

In this chapter, we report large spin to charge conversion (spin-Hall angle- 0.578) at $Ni_{80}Fe_{20}$/amorphous-Si interfaces attributed to flexoelectricity mediated Rashba spin-orbit coupling. The flexoelectricity at the interface also gave rise to flexoelectricity mediated interference coupling. In addition to spin-charge conversion, the strained interfaces also led to almost three-fold increase in anomalous Nernst effect. This strain engineering for spin dependent thermoelectric behavior at room temperature opens a new window to the realization of spintronics and spin-caloritronics devices.

6.1   Introduction

In this chapter, we hypothesized that the spontaneous polarization under an applied strain gradient (known as the flexoelectric effect – shown in Figure 6.1 (a)) will give rise to an electric field normal to the interface, which can give rise to Rashba SOC and large spin to charge conversion especially at semiconductor interfaces. Over the years, experimental studies have reported both proximity driven strong spin-splitting at Si surfaces [136, 137] as well as weak Rashba SOC in Si 2DES [119, 120].
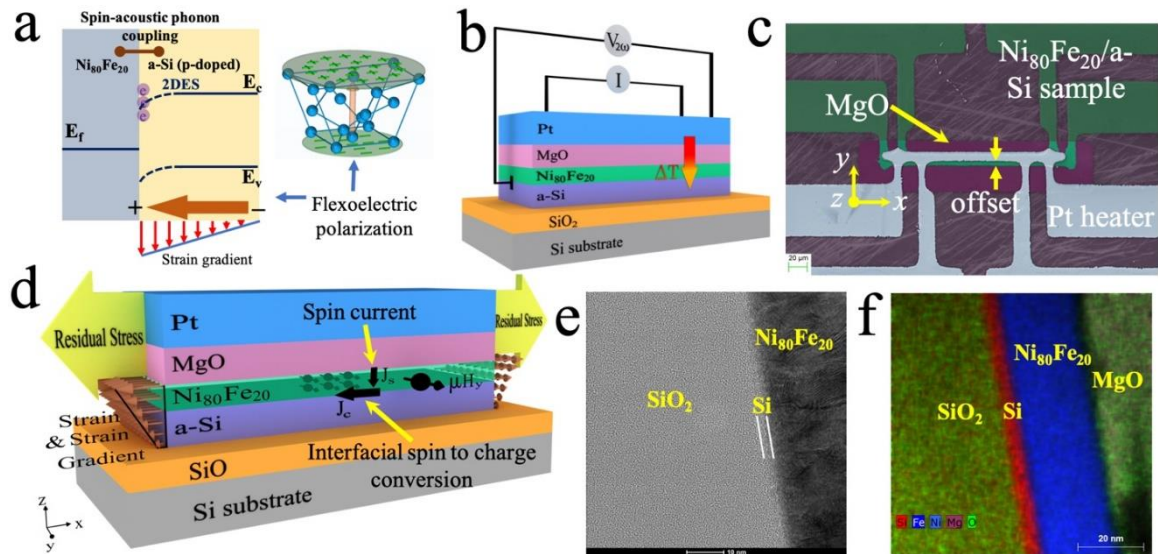
Figure 6.1 (a) a schematic showing flexoelectric polarization in Si lattice due to strain gradient and band diagram showing the mechanistic origin of Rashba SOC and interlayer coupling, (b) a schematic showing the experimental setup with the temperature gradient, (c) a representative false color scanning electron micrograph showing the experimental device, (d) a schematic showing the origin of strain and strain gradient leading to the interfacial spin-Seebeck effect in our experimental setup (e) a high resolution transmission electron micrograph showing the layered structure of the experimental specimen and (f) an energy dispersive X-ray spectroscopy elemental map showing the thin film layers and interfaces.

Recently, Lou et al. reported observation of large spin-Hall effect in Si due to strain gradient [146]. Similarly, Yang et al. experimentally reported that flexo-photovoltaic response in a-Si was an order of magnitude larger than $SrTiO_3$ [147]. This led us to hypothesize that strain gradient mediated 2DES at the p-doped Si interface might exhibit stronger Rashba SOC and large spin-to-charge conversion without any gate biasing. Our hypothesis is similar to a recent report where ferroelectric field perpendicular to the interface was used to manipulate spin to charge conversion [148]. Instead, we propose to use flexoelectric field, which does not require large gate bias. We chose amorphous-Si (a-Si) as it lacks a center of inversion and may exhibit larger flexoelectric polarization as well

as strain splitting at nanoscale. The metal interface with p-doped a-Si will have a 2DES due to band bending as shown in Figure 6.1 (a). We chose highly doped Si layer to have higher carrier concentration due to charge separation [95]. This hypothesis was tested using a spin-Seebeck effect (SSE) measurement in p-doped amorphous-Si (a-Si) thin film interfaces. The spin-to-charge conversion in the case of a-Si was found to be an order of magnitude larger than that of Pt. This difference disappeared when the strain was relaxed, proving our hypothesis that strain and strain gradient caused by residual stresses give rise to 2DES and Rashba SOC.

6.2   Methods

We fabricated four devices with the following sample structures: a $Ni_{80}Fe_{20}$ (25 nm) control device, a Pt (3 nm)/$Ni_{80}Fe_{20}$ (25 nm), a $Ni_{80}Fe_{20}$ (25 nm)/a-Si (50 nm) and a $Ni_{80}Fe_{20}$ (25 nm)/a-Si (5 nm). We take a prime Si wafer and deposit 350 nm of thermal silicon oxide using chemical vapor deposition (CVD). Using lift-off photolithography, we then deposit the sample to be studied using the RF sputtering. The sputtering deposition will have substrate conformal thin film coating. Hence, it will have the same interfacial and surface roughness as the underlying layers. The second lift-off photolithography is carried out to deposit 50 nm MgO to electrically isolate the sample from the heater. The third lift-off photolithography is then used to deposit heater composed of Ti (10 nm)/Pt (100 nm) using e-beam evaporation.

The residual stresses from Pt (heater) and MgO (insulator) layers are proposed to be the underlying cause of strain gradient mediated Rashba SOC. The existence of residual

stresses can be seen in Figure 6.2, where the Pt heater was delaminated due to the residual stresses.
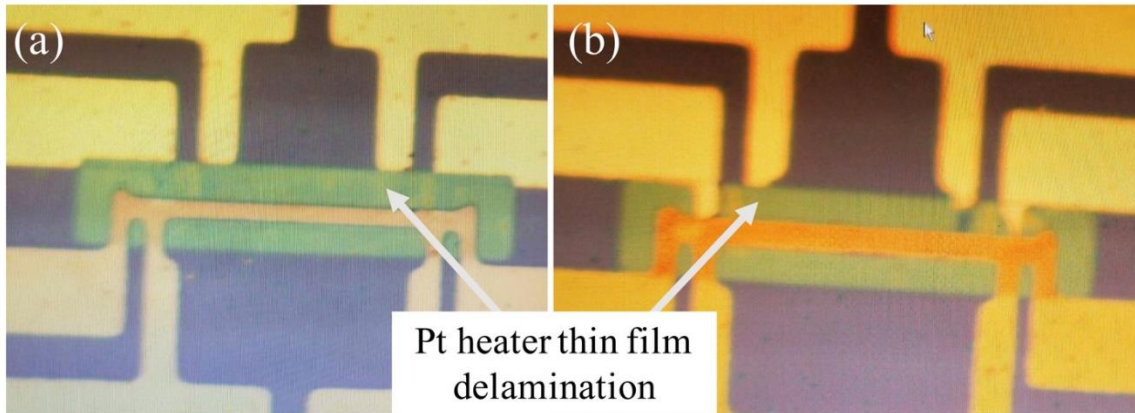
Figure 6.2. (a)-(b)The optical images showing Pt thin film heater layer peeled off (delaminated) due to residual stresses for two devices. The residual stress in Pt heater and MgO layer is proposed to be the cause of strain and strain gradient in the underlying sample.

For the second set of devices with switched sample and heater positions, we first deposited Ti (10 nm) / Pt (100 nm) on a Si wafer with predisposition of thermal silicon oxide (650 nm) using CVD. We then sputter 50 nm MgO using RF sputtering for electrical isolation. We fabricated two set of devices having the a-Si (50 nm)/$Ni_{80}Fe_{20}$ (25 nm) bilayer sample and $Ni_{80}Fe_{20}$ (25 nm) sample on top of the MgO.

These devices will allow us to estimate the ANE contribution and evaluate the efficiency of the spin-to-charge conversion of the a-Si. The order of layers in the Pt sample was switched to ensure that the anomalous Nernst effect (ANE) and transverse spin dependent thermal responses have the same sign [98]. The schematic of the device and a representative image are shown in Figure 6.1 (b, c), respectively. The temperature gradient (ΔT_z) was generated across the thickness of the thin film sample by passing an electric

current (I) through the Pt heater, as shown in Figure 6.1 (b). The residual compressive stresses, due to lattice mismatch and thermal expansion [149], in the MgO and Pt heater layer lead to a strain as well as a strain gradient in the sample, as shown in the Figure 6.1 (d). The resulting flexoelectric effect will lead to the hypothesized Rashba SOC at the interface. It was noted that the Pt heater layer was electrically isolated from the sample and will make no contribution towards any spin dependent response.

The structure of the thin films was verified using a high-resolution transmission electron microscope (HRTEM) study for the $Ni_{80}Fe_{20}$ (25 nm)/a-Si (5 nm) sample, as shown in Figure 6.1 (e)-(f). TEM lamellae were prepared from the layered sample following established procedures with a Dual Beam scanning electron microscope and FIB instrument using Ga ion source (Quanta 200i 3D, Thermo-Fisher Scientific). First, a strap of 5 µm thick protective Carbon layer was deposited over a region of interest using the ion beam. Subsequently approximately 80 nm thin lamella of was cut and polished at 30 kV and attached to a TEM grid using in-situ Omniprobe manipulator. To reduce surface amorphization and Gallium implantation final milling at 5 kV and 0.5 nA was used to thin the sample further. TEM and STEM imaging was performed at 300 kV accelerating voltage in a Thermo-Fisher Scientific Titan Themis 300 instrument, fitted with X-FEG electron source, 3 lens condenser system and S-Twin objective lens. High-resolution TEM images were recorded at resolution of 2048x2048 pixels with a FEI CETA-16M CMOS digital camera with beam convergence semi-angle of about 0.08 mrad. STEM images were recorded with Fischione Instruments Inc. Model 3000 High Angle Annular Dark Field (HAADF) Detector with probe current of 150 pA, frame size of 2048x2048, dwell time of

15 μsec/pixel, and camera length of 245 mm. Energy dispersive X-ray Spectroscopy (EDS) analyzes and elemental mapping were obtained in the STEM at 300 kV, utilizing Thermo-Fisher Scientific SuperX system equipped with $4x30mm^2$ window-less SDD detectors symmetrically surrounding the specimen with a total collection angle of 0.68 srad, by scanning the thin foil specimens. Elemental mapping was performed with an electron beam probe current of 550 pA at 1024 x1024 frame resolution. From the HRTEM study, we observed a continuous a-Si thin film layer for a 5 nm a-Si sample. We did not observe any measurable Ni or Fe diffusion in the a-Si layer as shown in Figure 6.1 (f).

We also did surface roughness measurement using Atomic Force Microscopy (AFM). The surface roughness of the bilayer sample directly reflects the underlying interfacial roughness. The interfacial roughness cannot be more than the surface roughness since the sputter coating is conformal. The AFM measurements are carried out on samples having 50 nm a-Si and 5 nm a-Si layers as shown in Figure 6.3. Using HRTEM and AFM measurement, we deduced that the mean roughness for the a-Si samples is ~1.22 nm, as shown in Figure 6.3.
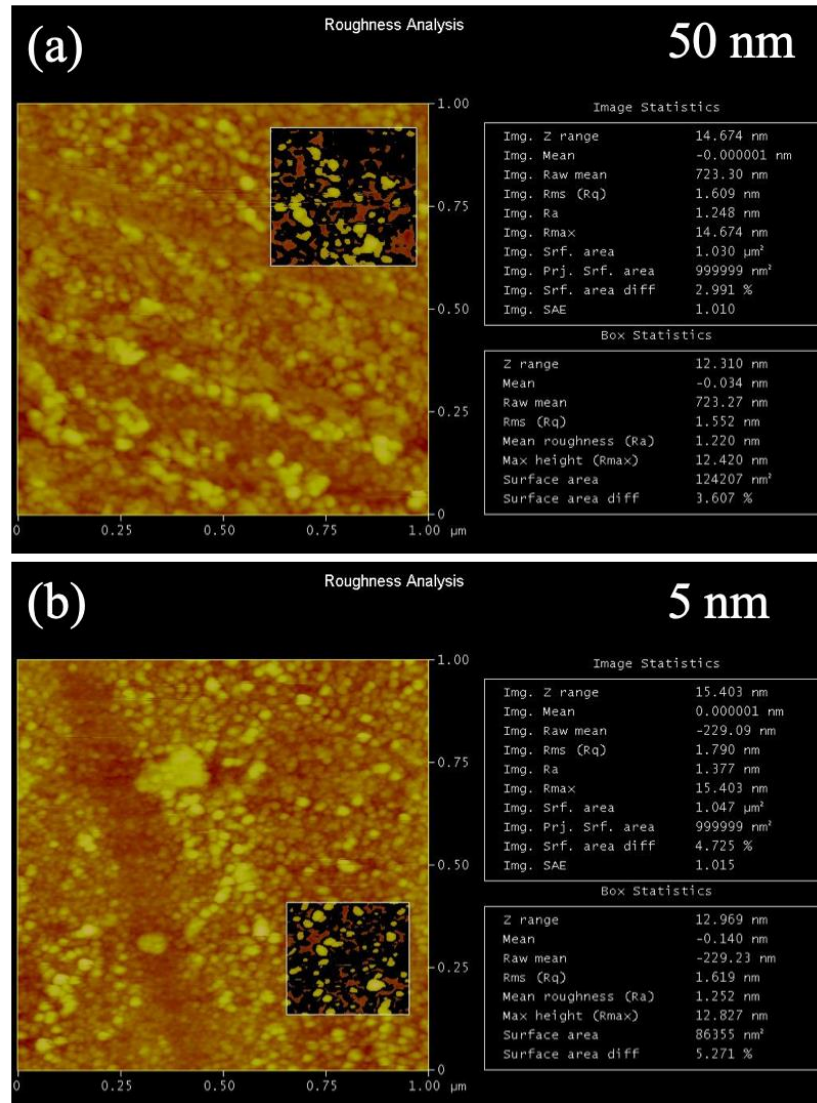
Figure 6.3. The AFM measurements at the surface of $Ni_{80}Fe_{20}$ layer in (a) 50 nm and (b) 5 nm a-Si bilayer samples. The mean roughness of both samples is ~1.2 nm.

6.3 Results

The transverse thermoelectric response measurements were undertaken at 30 mA/5 Hz of heating current and resulting $V_{2\omega}$ response (being quadratic in heating current) was acquired as a function of the magnetic field (1500 Oe to -1500 Oe) applied in the y-direction (normal to the temperature gradient). This is called in-plane magnetized (IM)

configuration of thermoelectric response measurement. The $V_{2\omega}$ responses were measured

at 300 K are 15.1 µV, 33 µV, 85 µV and 165.45 µV for $Ni_{80}Fe_{20}$, Pt, 50 nm a-Si and 5 nm

a-Si devices respectively, as shown in Figure 6.4 (a).
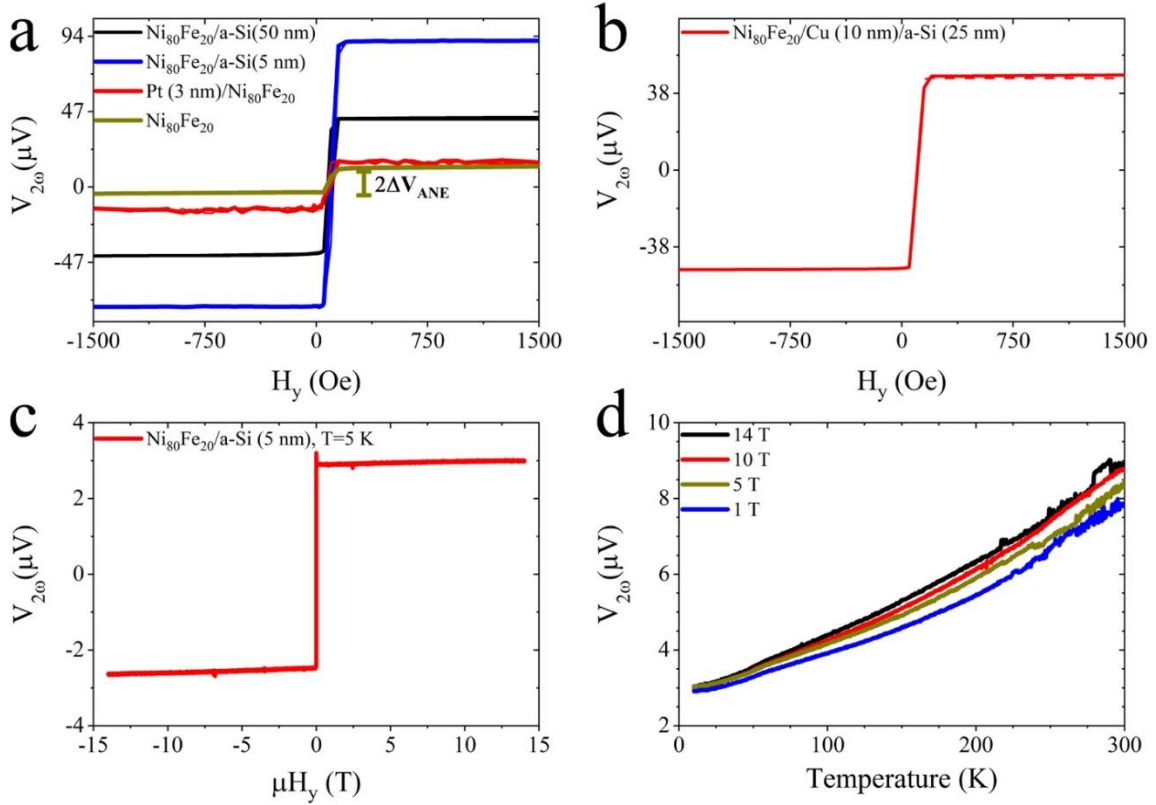
Figure 6.4. (a) the transverse spin dependent thermal measurement for $Ni_{80}Fe_{20}$ (25 nm), Pt (3 nm)/$Ni_{80}Fe_{20}$ (25 nm), $Ni_{80}Fe_{20}$ (25 nm)/a-Si (50 nm) and $Ni_{80}Fe_{20}$ (25 nm)/a-Si (5 nm) samples at 300 K, (b) the spin-Seebeck effect measurements for $Ni_{80}Fe_{20}$ (25 nm)/Cu (10 nm)/a-Si (25 nm) sample at 300 K, (c) the high magnetic field transverse spin dependent thermal measurement for $Ni_{80}Fe_{20}$ (25 nm)/a-Si (5 nm) sample at 5 K, and (d) the transverse spin dependent thermal measurement as a function of temperature for $Ni_{80}Fe_{20}$ (25 nm)/a-Si (5 nm) sample at an applied magnetic field (μH_y) of 1 T, 5 T, 10 T and 14 T from 300 K to 10 K. The fluctuations in the temperature-dependent measurements are due to instrumental settings.

All the samples had the resistances between 320 Ω- 350 Ω and $Ni_{80}Fe_{20}$ thin film

resistivity was expected to be 5×10^{-7} Ωm. In the case of $Ni_{80}Fe_{20}$, the measured response

of 15.1 µV was attributed to the ANE. In the case of the Pt sample, the estimated transverse spin dependent response was due to SSE having magnitude of ~18 µV; a behavior consistent with the reported ANE and SSE responses for the Pt/ $Ni_{80}Fe_{20}$ sample [98]. The corresponding transverse spin dependent thermal response in the case of the a-Si samples will be ~70 µV and 150.35 µV for 50 nm and 5 nm a-Si, respectively, which was 4 times and 8.5 times that of SSE response in Pt sample. The interfacial roughness between 50 nm and 5 nm a-Si samples was not different, as shown in Figure 12, and will not cause observed difference in measurements. We also measured the transverse thermoelectric response of 33.5 µV in 50 nm a-Si sample at 20 mA of heater current as shown in Figure 6.5.
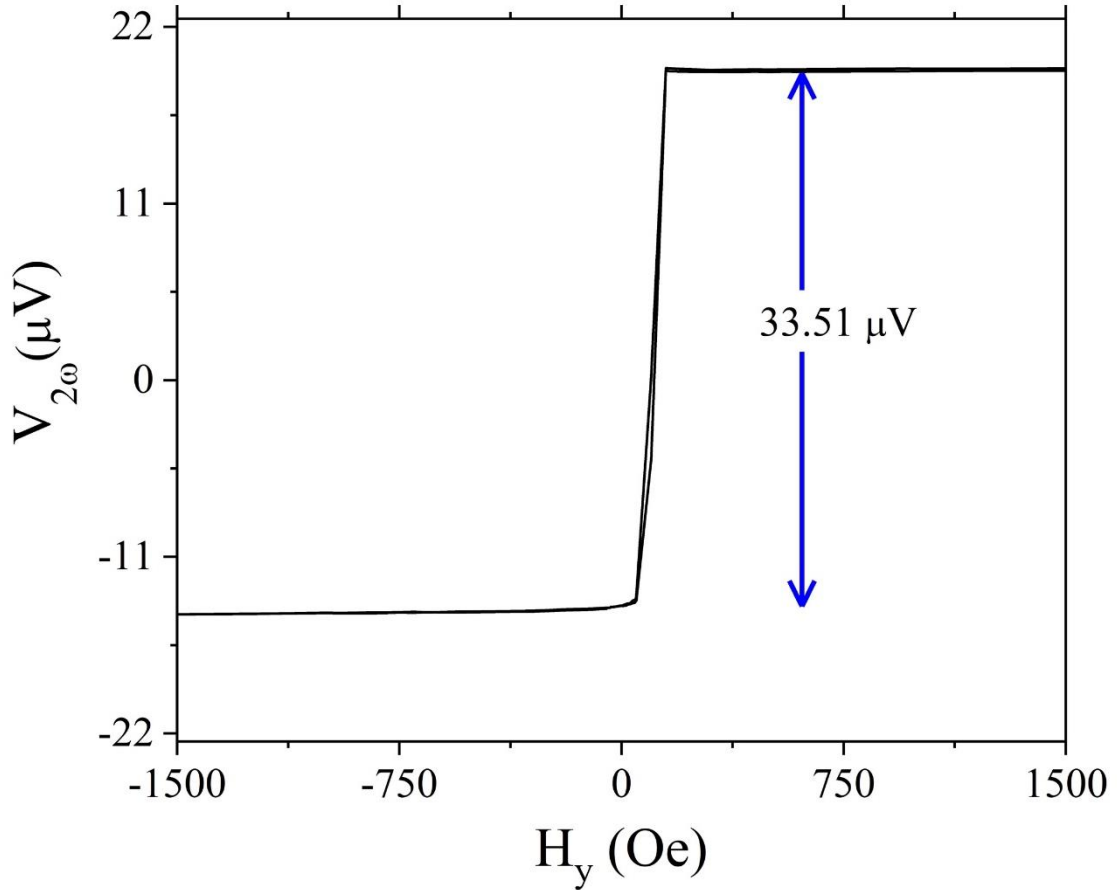
Figure 6.5. The $V_{2\omega}$ response in IM configuration in $Ni_{80}Fe_{20}$/a-Si (50 nm) sample.

Heating power follows a quadratic relationship with the current. The corresponding response at 30 mA should have been 75.37 µV (2.25 times 33.5 µV) as compared to 85 µV. This difference was attributed to the additional strain gradient due to thermal expansion mismatch at the interface. The larger strain gradient was also responsible for larger transverse spin dependent thermal response in the thinner 5 nm a-Si sample. We used the 3ω method [150] to estimate the increase in heater temperature and finite element method simulation to estimate the temperature drop across $Ni_{80}Fe_{20}$ layers. The 3ω measurement was carried out at 20 mA and resulting temperature rise was estimated to be

74

18.817 K and 18.45 K for 50 nm a-Si and 5 nm a-Si devices, respectively. The $V_{3\omega}$ responses were 6.58 mV and 5.0718 mV for 50 nm a-Si and 5 nm a-Si devices, respectively. Similarly, the values of R' were estimated to be 0.07 Ω/K and 0.055 Ω/K for Pt thin film in 50 nm a-Si and 5 nm a-Si devices, respectively. Resistivity of the Pt heater is approximately $3.8 - 4 \times 10^{-7}$ Ωm. The temperature rise could also be verified using change in resistance due to large current. From a different 5 nm a-Si sample, we measured a change in resistance due to 20 mA of current to be ~1.2 Ω. Consequently, the temperature rise at the heater will be 21.8 K, which was slightly higher, and this difference could arise due to small variation in the value of R'. Hence, the heater temperature estimates were using 3ω method were correct. The corresponding temperature rise for 30 mA of heating current would be 42.34 K and 41.50 K, respectively. Using this temperature information, we did finite element simulation using COMSOL and found the temperature difference across the Py film for 50 nm a-Si and 5 nm a-Si devices to be 11.924 mK and 11.388 mK, respectively. The values of thermal conductivities used in COMSOL simulations are 20 W/mK, 30 W/mK and 15 W/mK for $Ni_{80}Fe_{20}$, 50 nm a-Si and 5 nm a -Si, respectively. The vertical temperature distribution for 5 nm a-Si and 50nm a-Si along with temperature data at the interfaces is shown in the Figure 6.6 (a) and (b), respectively.
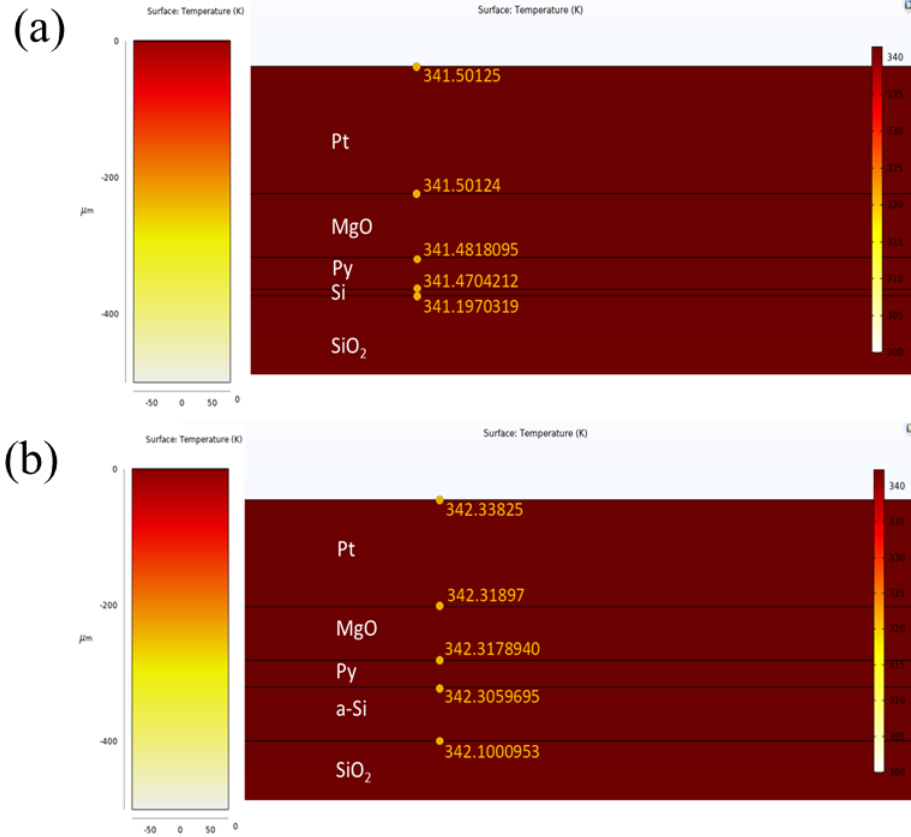
Figure 6.6. (a) Temperature distribution for 5 nm a-Si SSE device (b) Vertical temperature distribution for 50 nm a-Si SSE device

The spin Seebeck coefficient is estimated using spin Seebeck coefficient equation discussed in chapter 2. For 5nm a-Si and 50 nm a-Si the $V_{2\omega}$ is 150.45 µV and 70 µV respectively. So, the S_{LSSE} for 5 nm a-Si and 50nm a-Si is 1.032±0.1 µV/K and 0.458±0.05 µV/K, respectively. The corresponding ANE (easy axis) coefficient of $Ni_{80}Fe_{20}$ was estimated to be 0.1 µV/K. While this value was larger than the values reported in literature (0.045 µV/K) [151] but the ANE (easy axis) coefficient in thin film could be as large as 0.5%[151] of Seebeck coefficient (-20 µV/K), as reported in this study.

To uncover the effects of strain gradient, we fabricated a set of control devices with unstrained samples where the position of sample and heater were switched as shown in Figure 6.7.
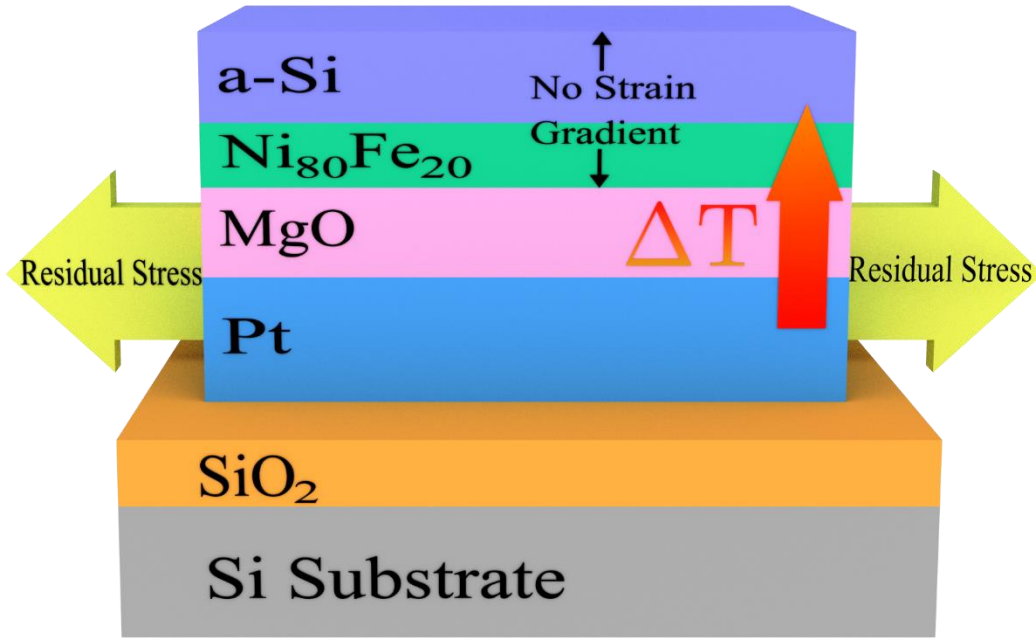
Figure 6.7 The schematic showing the experimental setup for unstrained samples.

We had hypothesized that strain gradient mediated Rashba SOC is the underlying cause of large spin dependent thermal responses presented in this study. Thus, these responses should disappear if the strain is removed. We demonstrated this situation by modifying the experimental setup – switching the position of the heater and the sample, as shown in Figure 6.7. In this configuration, the sample is no longer constrained by the MgO (insulator) and Pt (heater) layers, thus, the strain and strain gradient effects will be significantly reduced. We fabricated set of devices in the new configuration having the following structure- a-Si (50 nm)/Ni$_{80}$Fe$_{20}$ (25 nm), Ni$_{80}$Fe$_{20}$ (25 nm) and Pt (3

nm)/$Ni_{80}Fe_{20}$ (25 nm). We will call the new samples as unstrained while the samples with heater (Pt) on top will be referred to strained.

The transverse thermoelectric response in IM configuration was 0.95 µV, 0.35 and 0.71 in unstrained a-Si (50 nm)/$Ni_{80}Fe_{20}$, $Ni_{80}Fe_{20}$ and Pt/$Ni_{80}Fe_{20}$ samples, respectively, as shown in Figure 6.8 (a)-(d) and in Table 6-1. The transverse thermoelectric response in case of Pt/$Ni_{80}Fe_{20}$ was estimated by angle dependent measurement as shown in Figure 6.8 (d) since planar Nernst effect (PNE) response made it difficult to measure in field dependent measurement as shown in Figure 6.8 (c). Similar to strained samples, the SSE response in Pt (0.36 µV) was estimated to be same as the ANE response in $Ni_{80}Fe_{20}$ (0.35 µV). The spin dependent thermal response in a-Si sample was found to be 1.67 times larger than that of Pt sample as compared to four times in strained sample. This difference clearly supported our hypothesis of strain gradient mediated Rashba SOC at the interface. Based on the ANE coefficient of 0.1 µV/K reported earlier, we estimated the temperature difference of 0.27 mK across the thickness of the sample. Hence, ANE coefficient, estimated in this study, is believed to be correct for our experimental configuration.

Figure 6.8. The magnetic field dependent transverse thermoelectric response measurement in IM configuration in (a) a-Si (50 nm)/ $Ni_{80}Fe_{20}$ (25 nm), (b) $Ni_{80}Fe_{20}$ (25 nm) and (c) Pt (3 nm)/$Ni_{80}Fe_{20}$ (25 nm) unstrained samples, respectively. (d) the angle dependent (in xy-plane) transverse thermoelectric response in Pt (3 nm)/$Ni_{80}Fe_{20}$ (25 nm) unstrained sample.

Then, we introduced a 10 nm Cu layer in between the strained $Ni_{80}Fe_{20}$ (25 nm) and a-Si (25 nm) to remove the ferromagnetic proximity effect [81, 152]. For similar heating power, we measure the $V_{2\omega}$ response to be 95.8 μV for this, which was larger than that of Pt sample. The addition of Cu layer should have reduced the transverse thermal response due to shunting effect. However, the larger response in this case might arise from an additional strain gradient in 25 nm a-Si layer due to additional layer. This measurement eliminated the ferromagnetic proximity effect.

Table 6-1. List of ANE (easy axis) and SSE responses and corresponding coefficients for both unstrained and strained samples in IM configuration.

IM configuration	Sample	$2(V_{ANE} + V_{SSE})$ (μV)	ANE/SSE Coefficient ($\mu V/K$)
Strained	$Ni_{80}Fe_{20}$	15.1	0.1 (ANE)
	$Pt/Ni_{80}Fe_{20}$	33	0.117 (SSE)
	$Ni_{80}Fe_{20}/a-Si$ (50 nm)	85	0.458±0.05 (SSE)
	$Ni_{80}Fe_{20}/a-Si$ (5 nm)	165.45	1.032±0.1 (SSE)
	$Ni_{80}Fe_{20}/Cu/a-Si$ (25 nm)	95.8	-
Unstrained	$Ni_{80}Fe_{20}$	0.35	-
	$Pt/Ni_{80}Fe_{20}$	0.71	-
	a-Si (50 nm)/$Ni_{80}Fe_{20}$	0.95	-

Then, we measured the $V_{2\omega}$ response at 5 K for 10 mA of heating current and applied magnetic field from 14 T to -14 T in the 5 nm a-Si bilayer sample, as shown in Figure 6.4 (c). The magnonic spin current could be suppressed at low temperatures and with high magnetic field [153, 154], which we did not observe as shown in Figure 6.4 (c). This suggested that the origin of the spin current was due to the spin dependent Seebeck effect (SDSE). This assertion was further supported by the $V_{2\omega}$ response as a function of temperature from 10 K to 300 K with applied magnetic field 1 T, 5 T, 10 T, and 14 T as shown in Figure 6.4 (d). The $V_{2\omega}$ response increased as the magnetic field was increased.

This shows that the origin of spin current was most likely electronic and not magnons [134], hence the SDSE was the underlying cause of the transverse spin dependent thermal response reported in this work. The increase in the $V_{2\omega}$ response with increasing magnetic field could be attributed to an increase in SDSE due to a reduction in electron-magnon scattering at higher magnetic fields. While the origin of spin current was due to SDSE, we propose to call transverse spin dependent thermal response as SSE since the detection was attributed to the spin-to-charge conversion.

Then, we undertook measurements in perpendicularly magnetized (PM) configuration [48]. In PM configuration, in-plane temperature difference (ΔT_y) and out of plane magnetic field (μH_z) led to transverse thermal response as shown in inset of Figure 6.9 (a). In the measurement devices, the heater and sample had an offset due to lithographic misalignment, as shown in Figure 6.1 (c). This offset gave rise to a temperature gradient along the y-axis. Since the misalignment was not controlled, the resulting temperature difference varies from sample to sample.
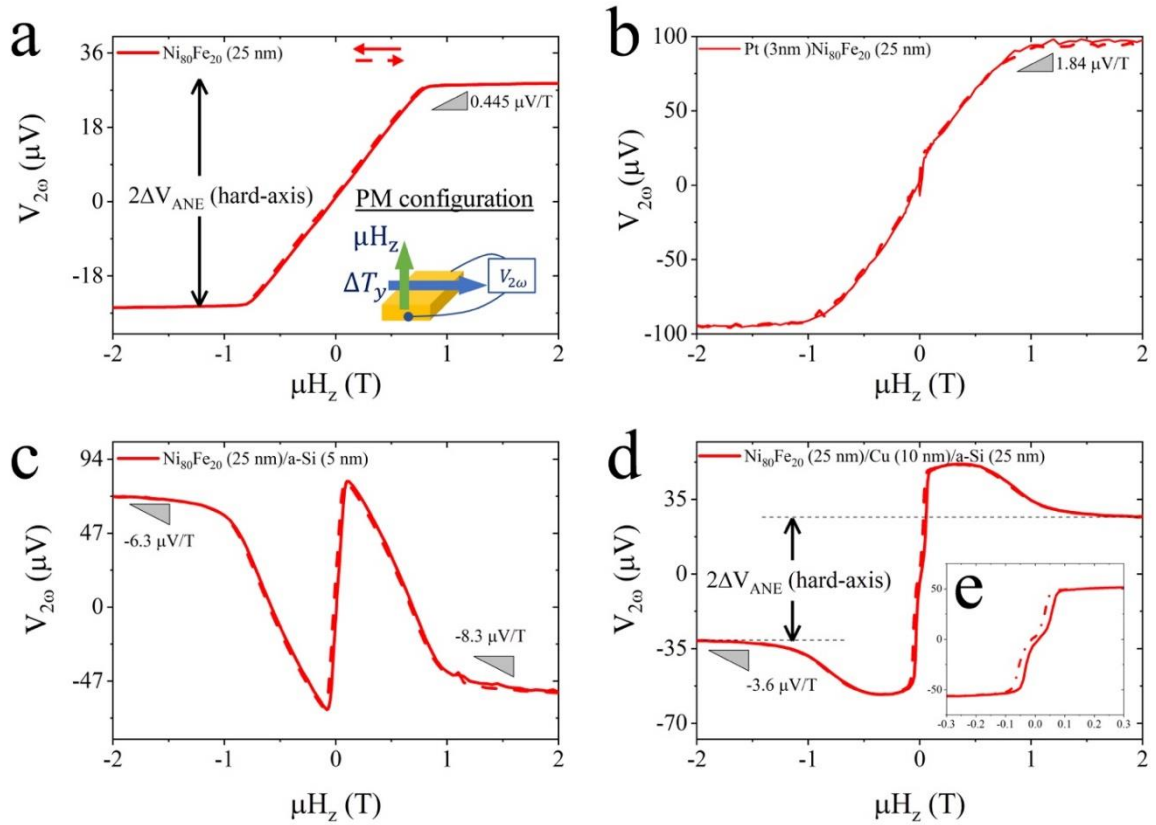
Figure 6.9. The $V_{2\omega}$ response perpendicularly magnetized (PM) configuration for an applied magnetic field sweep from 2 T to -2 T in (a) $Ni_{80}Fe_{20}$ (25 nm), (b) Pt(3nm)/$Ni_{80}Fe_{20}$ (25 nm). Similar measurement in (c) $Ni_{80}Fe_{20}$ (25 nm)/a-Si (5 nm) and (d) $Ni_{80}Fe_{20}$ (25 nm)/Cu (10 nm)/a-Si (25 nm) samples. (e) shows the low field behavior (between 0.3 T to -0.3 T) in $Ni_{80}Fe_{20}$ (25 nm)/Cu (10 nm)/a-Si (25 nm) sample. Inset in (a) shows the measurement setup. Arrows in (a) shows the direction of magnetic field sweep.

The transverse thermoelectric responses in all the strained and unstrained were measured in PM configuration for applied magnetic field of 2 T to -2 T as shown in Figure 6.9 and Figure 6.10, respectively, and are listed in Table 6-2.
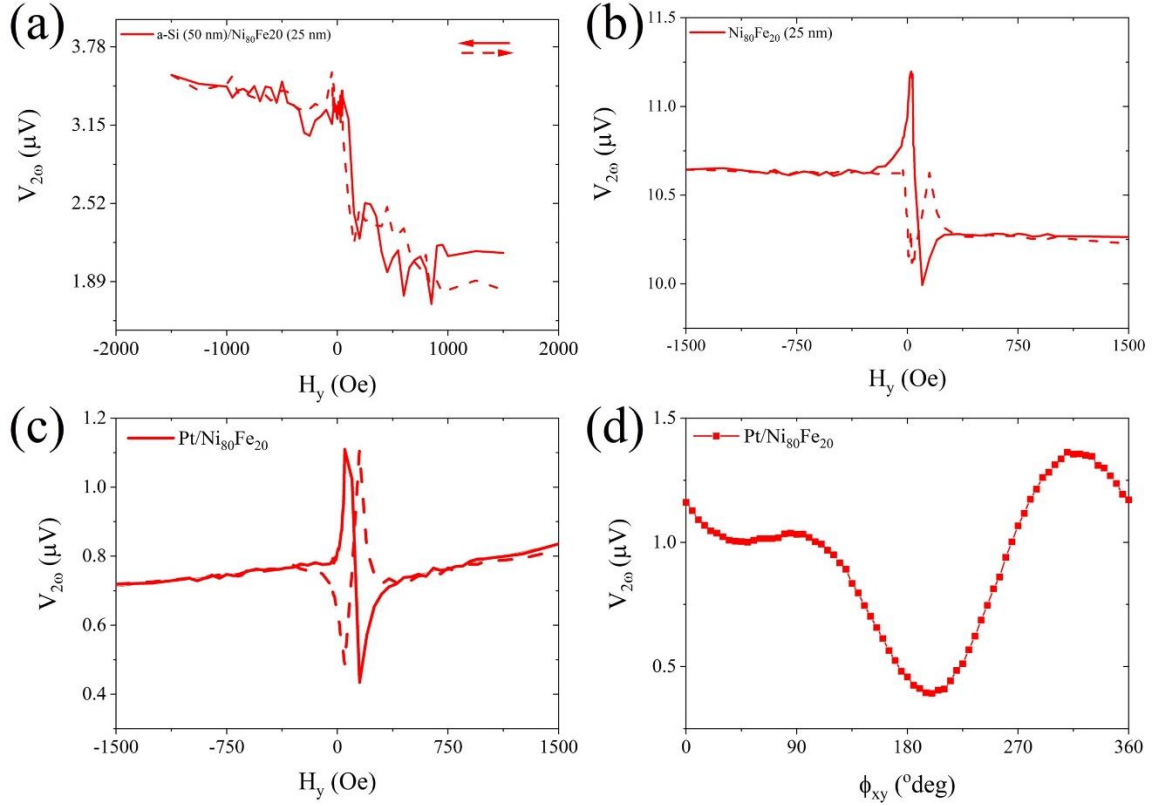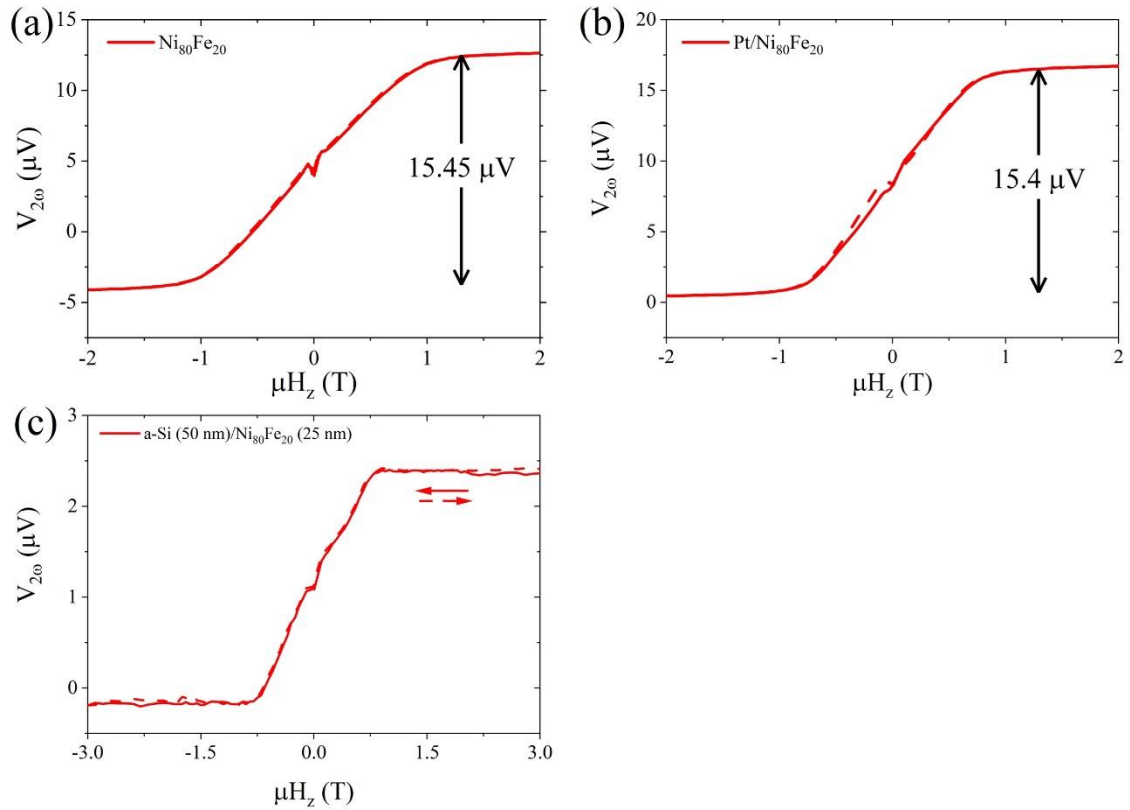
Figure 6.10. The magnetic field dependent transverse thermoelectric response measurement in PM configuration in unstrained (a) $Ni_{80}Fe_{20}$ (25 nm), (b) Pt (3 nm)/$Ni_{80}Fe_{20}$ (25 nm) and (c) a-Si (50 nm)/ $Ni_{80}Fe_{20}$ (25 nm) samples, respectively.

Table 6-2 List of ANE and ONE responses and corresponding coefficients for both unstrained and strained samples in PM configuration.

PM configuration	Sample	$2V_{ANE}$ (Hard axis) (μV)	ANE Coefficient (μV/K)	ONE (μV/T)	ONE coefficient (μV/(KT)
Strained	$Ni_{80}Fe_{20}$	52.50	6.6	0.445	0.113
	$Pt/Ni_{80}Fe_{20}$	185	4.65	1.84	0.0926
	$Ni_{80}Fe_{20}$/a-Si (5 nm)	95.93	6.6	-6.3 (-μH_z) and -8.3 (+μH_z)	-0.542 (-μH_z) and -0.714 (+μH_z)
	$Ni_{80}Fe_{20}$/Cu/a-Si (25 nm)	71.5	6.6	-3.6 μV/T	-0.664
Unstrained	$Ni_{80}Fe_{20}$	15.45	2.565	0.338	0.113
	$Pt/Ni_{80}Fe_{20}$	15.40	2.565	0.278	0.0926
	a-Si (50 nm)/$Ni_{80}Fe_{20}$	2.5	2.565	0.0015	0.0015

For unstrained samples, the $Ni_{80}Fe_{20}$ sample showed a hard-axis ANE behavior and measured response is 15.45 μV. The Pt sample also exhibits hard-axis ANE behavior and measured response is 15.4 μV. Using the planar Nernst response ($\sin 2\theta$ in xy-rotation as shown in Figure 6.8 (d) of 0.21 μV and PNE coefficient of 70 nV/K, we estimated a $\Delta T_y =$

0.1875 K along the width of the sample. The corresponding out of plane $2V_{ANE}$ was 15.4 µV. Using the temperature information, we estimated the ANE coefficient for in-plane temperature gradient:

$$S_{ANE} = \frac{V_{ANE}w}{L\Delta T} \tag{17}$$

where, $2V_{ANE} = V_{2\omega} = 15.4$ µV, w= 10 µm, L = 160 µm and ΔT is the temperature difference across the width of $Ni_{80}Fe_{20}$ thin film. The ANE coefficient for hard-axis magnetization was estimated to be 2.565 µV/K. Using the slope of high field behavior, we could also estimate the ordinary Nernst effect (ONE) coefficient. The unstrained samples had the slopes of 0.338 µV/T, 0.278 µV/T and 0.0015 µV/T in $Ni_{80}Fe_{20}$, Pt/ $Ni_{80}Fe_{20}$ and a-Si (50 nm)/ $Ni_{80}Fe_{20}$ samples, respectively. Using ΔT_y= 0.1875 K, we estimated that the S_{ONE} were 0.113 µV/(KT) and 0.0926 µV/(KT) in $Ni_{80}Fe_{20}$ and Pt/ $Ni_{80}Fe_{20}$ samples, respectively, as shown in Table 6-2. For the unstrained a-Si (50 nm)/ $Ni_{80}Fe_{20}$ sample, we assumed that the ANE coefficient would be same as $Ni_{80}Fe_{20}$. The resulting S_{ONE} in unstrained a-Si sample was estimated to be 0.0015 µV/(KT).

We also estimated the ANE coefficients, ONE response and ONE coefficient for all the samples where temperature could be ascertained as shown in Table 6-2. The temperatures were estimated using planar Nernst effect (PNE) coefficient of 70 nV/K [155] and assuming ONE coefficient will not change in $Ni_{80}Fe_{20}$ sample since it is bulk behavior. The slope for ONE in strained samples– +0.445 µV/T, +1.84 µV/T, -8.3 µV/T and -6.3 µV/T and -3.6 µV/T in $Ni_{80}Fe_{20}$, Pt/ $Ni_{80}Fe_{20}$, $Ni_{80}Fe_{20}$/a-Si (5 nm) and $Ni_{80}Fe_{20}$/Cu/a-Si (25 nm) as shown in Figure 6.9. In $Ni_{80}Fe_{20}$ sample (strained), we estimated the horizontal

temperature difference using ANE and ONE coefficient is to be 0.64 K and 0.247 K, respectively, as shown in Table 6-2. However, the ONE coefficient reflects primarily the bulk behavior whereas ANE response can be significantly affected by the interfaces. Hence, the temperature difference calculated using ONE behavior is assumed to be closer to actual temperature difference. Using ΔT_y=0.247 K and ANE response of 52.5 µV, we estimated the S_{ANE} in strained $Ni_{80}Fe_{20}$ sample to be 6.6 µV/K instead of 2.565 µV/K in the unstrained sample. It is noted that unstrained sample had one interface with MgO while the strained sample had two interfaces one with MgO and other with SiO_2. And this increase in ANE coefficient was expected to arise due to spin dependent behavior at interfaces with oxides. To demonstrate the effect of interface, we compared the ONE coefficient is in strained and unstrained Pt devices and estimated the temperature a difference of ΔT_y=1.437 K in strained Pt device. Using this temperature information, we estimated the ANE coefficient from 185 µV ANE (hard axis) response to be 4.65 µV/K, which was smaller than strained $Ni_{80}Fe_{20}$ sample. This difference in ANE coefficients was attributed to the absence of $MgO/Ni_{80}Fe_{20}$ interface in the strained $Pt/Ni_{80}Fe_{20}$ sample. For 5 nm a-Si strained sample, the ONE response was negative and could not be considered to be same as $Ni_{80}Fe_{20}$ sample in spite of a-Si being only 5 nm. Instead, we estimated the temperature difference of ΔT_y=0.726 K from 95.93 µV of ANE (hard axis) response and using ANE coefficient of 6.6 µV/K. Then, the corresponding S_{ONE} would be -0.542 µV/(KT) and -0.714 µV/(KT) for negative and positive magnetic fields, respectively. The a-Si sample clearly demonstrated an asymmetry in the ONE measurement. Using similar assumption, we estimated the ΔT_y=0.338 K and S_{ONE}=-0.664 µV/(KT) in $Ni_{80}Fe_{20}/Cu/a$-Si

(25 nm) sample. This exercise demonstrated approximate temperature differences and corresponding ANE (hard axis) and ONE coefficients. The ANE coefficient was found to be 0.66 times that of Seebeck coefficient of $Ni_{80}Fe_{20}$ (bulk). This increase is attributed to spin-dependent behavior at MgO and SiO_2 interfaces.

Additionally, in case of unstrained a-Si (50 nm)/$Ni_{80}Fe_{20}$ sample, the transverse thermoelectric response in PM configuration exhibits a hard-axis ANE behavior and response is ~2.5 µV as shown in Figure 6.10 (c). This behavior is opposite as compared to the strained sample, as shown in Figure 6.9 (c). In strained sample, the magnitude of low field response in PM configuration is similar to total response in IM configuration, which means that 0.95 µV of low field thermal response should have been present in PM configuration for unstrained sample. The absence of such response clearly indicated that the observed behavior arose due to strain and strain gradient at the interface. In addition, the response in PM configuration also proves that the interstitial Cu and Ni atoms are not the primary drivers of spin dependent behavior reported in this study. Instead, interfacial roughness in conjunction with strong Rashba SOC might be the underlying cause of observed behavior PM configuration as hypothesized.

The transverse thermoelectric response behavior in strained configuration are shown in Figure 6.9 (a)-(d). The ANE (hard-axis) coefficients were estimated to be 2.565 (±10%) µV/K and 6.6 (±10%) µV/K for unstrained and strained $Ni_{80}Fe_{20}$ samples, respectively. The ANE (hard-axis) coefficient was found to be ~0.128 times the Seebeck coefficient in the unstrained sample was similar to bulk value of 0.13 [44, 156], which then increased to 0.33 in the strained sample. This increase arose due to self-induced spin

dependent behavior at strained MgO and SiO$_2$ interfaces [157]. This argument was supported by reduction in ANE (hard-axis) coefficient (4.65 µV/K) in strained Pt/Ni$_{80}$Fe$_{20}$ sample, where Ni$_{80}$Fe$_{20}$ had only one interface with the oxide. This measurement showed that strained interfaces could change the behavior significantly. This measurement also showed that there was an order of magnitude difference between easy-axis and hard-axis ANE coefficients. This was attributed to the increased surface/interfacial scattering in the out of plane temperature gradient causing reduction in easy-axis ANE coefficient. The S$_{ONE}$ were 0.113(±10%) µV/(KT) and 0.0926(±10%) µV/(KT) in Ni$_{80}$Fe$_{20}$ and Pt/ Ni$_{80}$Fe$_{20}$ samples, respectively, as shown in Table 6-2.

The transverse thermoelectric response in Ni$_{80}$Fe$_{20}$/a-Si (5 nm) and Ni$_{80}$Fe$_{20}$/Cu/a-Si (25 nm) samples had ANE response, ONE response and an additional unknown response superimposed on them as shown in Figure 6.9 (c, d). The ONE response was negative for both the samples. Yang et al. [158] observed a similar to sign in anomalous Hall effect (AHE) in Mn$_x$Si$_{1-x}$, which they attributed to Rashba SOC. Hence, this transition seen in experiment was attributed to Rashba SOC. However, Rashba SOC might not lead to change in sign directly. The AHE due to skew-scattering is considered to have opposite sign as compared to intrinsic AHE [159]. We propose that the change in sign of ANE (hard axis) was due to transition from intrinsic mechanism to skew-scattering mechanism. We propose that flexoelectric mediated interlayer coupling between Ni$_{80}$Fe$_{20}$ and a-Si was the underlying cause of skew-scattering and it was also supported by negative ONE response.

The ANE and ONE measurement were supplemented by the Hall resistance measurements. Instead of a-Si, we utilized the single crystal Si device layer. The

freestanding thin film structure buckles due to residual stresses. We fabricated two devices with 2 µm a-Si and 400 nm a-Si. The thinner a-Si device would have larger strain gradient and consequently larger flexoelectric polarization. The Hall effect measurement was carried out at 200 K from 8 T to -8 T for both devices as shown in Figure 6.11. In the 2 µm a-Si device, the Hall resistance was negative, as it should be since electrons are the dominant charge carriers. Whereas, in 400 nm a-Si device, the Hall resistance was positive, which was attributed to hole mediated charge transport. The sign of Hall effect depends only on the sign of charge carrier and not on scattering mechanism as opposed to ONE. The flexoelectric field at the interface is expected to change the band structure of $Ni_{80}Fe_{20}$ layer leading to change in sign of charge carriers. This measurement clearly demonstrated that flexoelectric field is the underlying cause of large SSE response measurement in this study.
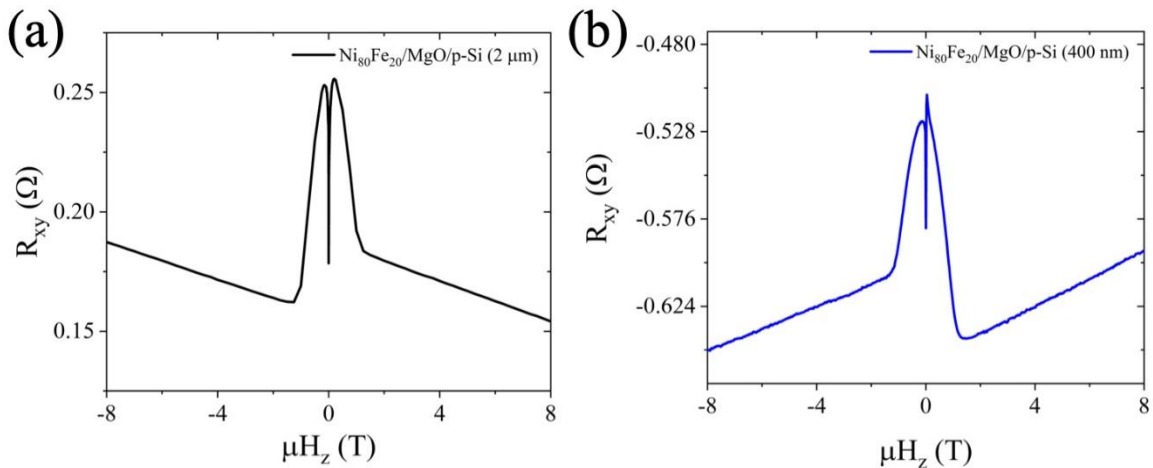
Figure 6.11. The Hall resistance measurement for an applied magnetic field of 8 T to -8T at 200 K showing (a) negative Hall resistance in $Ni_{80}Fe_{20}$ (25 nm)/MgO (1.8 nm)/a-Si(2 µm) and (b) positive Hall resistance in $Ni_{80}Fe_{20}$ (25 nm)/MgO(1.8 nm)/a-Si(400 nm).

The response in unstrained a-Si (50 nm)/$Ni_{80}Fe_{20}$ corroborated our hypothesis since both ONE and ANE responses were positive as shown in Table 6-2 and Figure 6.10 (c). The positive ANE response in sample with Cu interlayer also supported our hypothesis as shown in Table 6-2 and Figure 6.10 (d). These measurements further supported our contention that the response in IM configuration was due to strain gradient mediated SSE and not ANE (easy axis). The ANE (hard axis) response in the PM configuration was negative whereas the corresponding SSE response (in IM configuration) was positive in $Ni_{80}Fe_{20}$/a-Si (5 nm) sample. If the origin of the thermoelectric response in $Ni_{80}Fe_{20}$/a-Si (5 nm) sample in IM configuration was ANE (easy axis) then the sign should have been negative as opposed to positive. These measurements in PM configuration also suggested an additional reason for the larger SSE response in sample with Cu interlayer. In a-Si samples without the Cu interlayer, the ANE (easy axis) response was, possibly, negative and should be added to the measured response whereas in sample with Cu spacer the ANE (easy axis) response was positive and already included in the total response. If we use this analogy then the SSE response in 50 nm a-Si, 5 nm a-Si and sample with Cu spacer should be 100.1 µV, 180.45 µV and 80.7 µV, respectively. This might explain the absence of shunting effect in the raw data in addition to extra strain from Cu layer as stated earlier.

Then, we analyzed the unknown low field response in a-Si samples with and without Cu interlayer in the framework of Rashba coupled 2DES at rough interface. The interfacial roughness might force the Rashba coupled 2DES to have an out of plane component. Then, the spin current injected (due to vertical temperature gradient) from $Ni_{80}Fe_{20}$ into spin-momentum coupled 2DES will lead to the spin to charge conversion in

spite of magnetic field being perpendicular to the interface in PM configuration. However, once the magnetization of $Ni_{80}Fe_{20}$ was completely aligned out of plane at high magnetic fields (larger than saturation magnetization), the injected spin current will not have a component in the plane of interface and only ONE response due to in-plane temperature gradient would be left. In this framework, the magnitude of the transverse thermal response in PM configuration at low fields should be same as in the IM configuration because they both arise due to vertical temperature difference and spin to charge conversion. This behavior was clearly absent in $Ni_{80}Fe_{20}$ and $Pt/Ni_{80}Fe_{20}$ samples as well as in unstrained a-Si sample as shown in Figure 6.9 (a, b) and Figure 6.10, respectively. Our hypothesis needed a clear evidence of out of plane magnetization attributed to roughness. In $Ni_{80}Fe_{20}/a$-Si (5 nm) sample, the ONE response was significantly different for positive (-8.3 µV/T) and negative (-6.3 µV/T) magnetic fields. This asymmetry might arise due to interfacial spin polarization (out of plane) and was not observed in any other sample. Similarly, the low field response (in PM configuration) in sample with Cu interlayer exhibited a switching behavior that was similar to an exchange biased layered thin film as shown in Figure 6.9 (e). In addition, this exchange biased switching behavior was absent in the IM configuration as shown Figure 6.4 (b); a behavior expected of Rashba coupled 2DES – no net magnetic moment in the plane of the interface. This low field behavior was not observed in unstrained a-Si (50 nm)/$Ni_{80}Fe_{20}$ sample as shown in Figure 6.10 (c), which meant that strain gradient was expected to be the primary cause of observed responses in strained a-Si samples shown in Figure 6.9 (c, d). It needed to be stated that interfacial

roughness contributed to the behavior, but it was not the primary reason for observed low field response.

The next step was quantitative description of the spin-to-charge conversion efficiency. The spin-Hall angle of the Pt was 0.068 [160] for $Ni_{80}Fe_{20}$ ferromagnetic source. We estimated that the SSE response of 5 nm a-Si was 8.5 times that of SSE in Pt sample. The corresponding spin-Hall angle for 5 nm a-Si will be 0.578. This value was much larger than that of most heavy metals [161]. The effective spin mixing conductance in bulk Si $(1.74 \times 10^{19} \text{ m}^{-2} – 5.2 \times 10^{19} \text{ m}^{-2})$ [162, 163] was reported to be similar to that of Pt $(2.1 \times 10^{19} \text{ m}^{-2})$ [164]. Hence, the spin injection efficiency might not be the underlying cause of large spin to charge conversion in a-Si. However, the strained a-Si might have larger spin mixing conductance due to magnetoelastic coupling and might contribute towards larger SSE response. The largest spin-Seebeck coefficient in this work was estimated to be 1.032 μV/K, which was smaller than YIG/NiO/Pt system reported by Lin et al [142]. Our value was similar to Fe_3O_4/Pt system [58]. However, we achieved it using strain gradient and in spite of insignificant SOC in Si.

For Rashba SOC-coupled 2DES, an alternate method to define the spin-to-charge conversion efficiency is Rashba-Edelstein length $\lambda_{IEE} = \alpha_R \tau / \hbar$, where α_R and τ are Rashba parameter and relaxation time, respectively. The Rashba spin splitting cannot be calculated from transport measurements. However, the Rashba-Edelstein length can be estimated using multiplication of spin-Hall angle and spin diffusion length. The smallest thickness of the a-Si used in our studies was 5 nm and it had the highest spin-Seebeck response. We assumed that spin diffusion length is approximately 5 nm. Using this value,

we estimated the Rashba-Edelstein length for a-Si samples to be ~2.68 nm. This value was larger than the value of Rashba-Edelstein length in the case of strained HgTe [165] ($\lambda_{IEE} = 2$) and α-Sn[166]). The largest magnitude of Rashba-Edelstein length has been reported for the 2DES at LAO/STO interface under a large gate bias (125 V [167] to 175 V [168]). However, there was no need for gate bias in the case of p-doped a-Si, as shown in this study. It needed to be stated that Rashba parameter cannot be estimated from these measurements since spin splitting is not known.

6.4   Conclusion

In conclusion, we reported one of the largest thermal spin-to-charge conversion response at a strained metal/a-Si interface. The efficiency of spin-to-charge conversion was an order of magnitude larger than that of Pt and similar to topological insulator surface states, however, without any added fabrication complexity. We also presented the first experimental proof of flexoelectric polarization mediated Rashba SOC, which avoided any gate biasing. We propose that the change in sign of ANE (hard axis) was due to transition from intrinsic mechanism to skew-scattering mechanism. We propose that flexoelectric mediated interlayer coupling between $Ni_{80}Fe_{20}$ and a-Si was the underlying cause of skew-scattering and it was also supported by negative ONE response. Interfacial strain not only gave rise to large spin to charge conversion, but it also led to 2.5 times increase in anomalous Nernst coefficient in $Ni_{80}Fe_{20}$ thin films. The observation of a large SSE in an a-Si challenges the inherent need for large intrinsic SOC in spintronics and spin-caloritronics research.

Chapter 7

Conclusions & Future Directions

There are many natural and artificial available heat sources to convert heat energy to useful work (electrical or mechanical). Conventional thermoelectric devices were considered best for heat energy harvesting until the discovery of nanotechnology and spin Seebeck effect. They have some bottlenecks such as large size, highly resistant, rigid, inefficient at low temperature gradient or room temperature environment. MEMS is a great option for providing low cost and highly efficient energy harvesting devices. Discovery of magnetothermoelectrical effects such as spin Seebeck effect (SSE) is a breakthrough in the research of heat energy harvesting as they are efficient, reliable, flexible and operate at low temperature gradient and room temperature. However, the spin current to charge current conversion in SSE is done by using heavy metals such as Ta, Pt and W due to their large spin orbit coupling. It is required to explore earth abundant, economical, low processing-based material such as silicon for spin to charge current conversion by using interfacial Rashba spin orbit coupling.

Silicon is a diamond cubic centrosymmetric structure without any large spin orbit coupling. The weak spin orbit coupling of silicon makes it as inessential spintronic material. However, we are the first experimentalist to use silicon as a spin to charge conversion material by removing the spin degeneracy using the strain engineering at the room temperature. The spin to charge conversion efficiency was an order larger than

commonly used heavy metal platinum that occurred due to the presence of strong Rashba spin orbit coupling (SOC) in the 2D electron gas (2DEG) system generated at the Py and a-Si interface because of flexoelectric effect and broken inversion asymmetry. The inhomogeneous strain and strain gradient due to lattice mismatch during fabrication and thermal expansion during the joule heating will cause the charge separation due to flexoelectric effect which is responsible for large Rashba spin orbit coupling at the Py/a-Si interface.

The large spin Seebeck response is reported for 25 nm Py / 5 nm a-Si bilayer as 150.35 µV which is 8.5 times that of SSE response in Pt sample. The spin-Seebeck coefficients is 1.032±0.1 µV/K for 5 nm a-Si devices. The ANE contribution from LSSE is removed by subtracting magneto thermal transport response of 25 nm Py device from LSSE device, giving pure SSE response. The thickness dependent measurement by varying the silicon thin film thickness also shows variation in SSE response which confirms that the present observation is SSE as ANE is thickness independent phenomena. The COMSOL simulation showed that the temperature difference across the Py thin film is 11.388 mK for 5 nm a-Si LSSE device which shows the high efficiency of our LSSE device. The magnetic proximity effect at the Py/a-Si interface is removed by inserting a Cu layer because of its negligible response in SSE measurement and very large spin diffusion length allows to pass spin current.

To bolster our hypothesis of observation of strain mediated Rashba spin orbit coupling in silicon, we also fabricated unstrained LSSE device which showed 0.95 µV response for 50 nm a-Si LSSE device. The mean surface roughness for 5 nm and 50 nm a-

Si sample was almost same, which conforms that the observed behavior does not occur due to surface roughness. The low temperature measurement at 5 K showed small $V_{2\omega}$ response and temperature sweep from 10 K to 300 K at different magnetic field showed increment in $V_{2\omega}$ response with respect to increment in magnetic field. This manifest that the spin current is mostly electronic but not magnonic, thus spin dependent Seebeck effect is the underlying cause of spin current generation. However, the spin to charge current conversion is performed using inverse spin Hall effect which makes us to call this magneto thermoelectric effect as spin Seebeck effect.

This work will be considered as a foundation for silicon in future spintronics and spin caloritronics. The weak spin orbit coupling materials can be considered for spintronics and spin caloritronics devices by using strain engineering and/or by breaking structure inversion symmetry to lift the spin degeneracy. We observed such large spin Seebeck effect using bilayer thin film structure, if we implement multilayered heterostructure we can increase the second harmonic response and observe large spin Seebeck effect. Also, we can develop a numerical model for the simulation in COMSOL to find the spin Hall angle, strain dependent Rashba spin orbit coupling, stress-strain analysis, and temperature dependent magneto thermoelectric measurements. In general, micro magnetic simulation of magnetic structure can be done using OOMMF software and can be implement to study the magnetic properties of our sample. It is important to study the ballistic transport, scattering mechanisms, properties and interaction between energy carriers which are not important at macroscopic level. Experimentally, the stress and strain measurement can be done using surface profilometer and thin film stress gauze tool.

The overall thermoelectric energy conversion efficiency can also be increased by implementing spin Seebeck thermoelectric generator (TEG). Due to advanced nanofabrication technology and using flexible substrate such as polyimide, spin Seebeck TEG can be manufactured at high packing density. For flexible spin Seebeck TEG, parallel integration of electrodes is must to provide flexibility in any uniaxial direction and reduce mechanical stresses during any uniaxial bending. The main advantages of flexible thermoelectric module are small, lightweight, durable, maintenance free, solid state device, environmentally friendly, operate at low temperature difference, and noiseless.

In terms of solar energy harvesting, nano photovoltaic cells can be researched like thermoelectric generator. It is desired to implement nano solar cells with novel materials that are more efficient compared to modern solar cells. Comprehensive understanding of nano-photonics and nano plasmonic is required to accomplish the task of discovering the novel nano solar cell (NNSC) material that can harvest and store the energy for prolonged time. Some of the new thin film material for solar cells are a-Si, Cadmium Telluride, and copper indium gallium selenide (CIGS). There are current bottlenecks on mass manufacturing of thin film photovoltaic cells, efficiency, reliability, and availability. To address these problems, research will be done to make use of earth abundant material aided with novel phenomena to develop harmless efficient nano photovoltaic cells.

Bibliography

1.   Moultif, N., et al., *Reliability Study of High-Power Mechatronic Components by Spectral Photoemission Microscopy*, in *Reliability of High-Power Mechatronic Systems 2*. 2017, Elsevier. p. 241-271.

2.   Goennenwein, S.T. and G.E. Bauer, *Spin caloritronics: Electron spins blow hot and cold.* Nature nanotechnology, 2012. **7**(3): p. 145.

3.   Vandaele, K., et al., *Thermal spin transport and energy conversion.* Materials Today Physics, 2017. **1**: p. 39-49.

4.   Boona, S.R., R.C. Myers, and J.P. Heremans, *Spin caloritronics.* Energy & Environmental Science, 2014. **7**(3): p. 885-910.

5.   Berk, C., et al., *Strongly coupled magnon–phonon dynamics in a single nanomagnet.* Nature communications, 2019. **10**(1): p. 1-6.

6.   Woolsey, R.B. and R.M. White, *Electron-magnon interaction in ferromagnetic semiconductors.* Physical Review B, 1970. **1**(11): p. 4474.

7.   Inoue, J.-i., *2 - GMR, TMR, BMR, and Related Phenomena*, in *Nanomagnetism and Spintronics (Second Edition)*, T. Shinjo, Editor. 2014, Elsevier: Oxford. p. 15-106.

8.   Dejene, F., J. Flipse, and B. Van Wees, *Spin-dependent Seebeck coefficients of Ni 80 Fe 20 and Co in nanopillar spin valves.* Physical Review B, 2012. **86**(2): p. 024436.

9.   Erekhinsky, M., et al., *Spin-dependent Seebeck effect in non-local spin valve devices.* Applied Physics Letters, 2012. **100**(21): p. 212401.

10.   Rameshti, B.Z. and A.G. Moghaddam, *Spin-dependent Seebeck effect and spin caloritronics in magnetic graphene.* Physical Review B, 2015. **91**(15): p. 155407.

11.   Tang, X.-Q., et al., *Metal-free magnetism, spin-dependent Seebeck effect, and spin-Seebeck diode effect in armchair graphene nanoribbons.* Scientific reports, 2018. **8**(1): p. 1-6.

12.   Choi, G.-M., et al., *Thermal spin-transfer torque driven by the spin-dependent Seebeck effect in metallic spin-valves.* Nature physics, 2015. **11**(7): p. 576-581.

13.   Fu, H.-H., et al., *Spin-dependent Seebeck effect, thermal colossal magnetoresistance and negative differential thermoelectric resistance in zigzag silicene nanoribbon heterojunciton.* Scientific reports, 2015. **5**: p. 10547.

14.   Uchida, K., et al., *Observation of the spin Seebeck effect.* Nature, 2008. **455**(7214): p. 778.

15.   Ramos, R., et al., *Observation of the spin Seebeck effect in epitaxial Fe3O4 thin films.* Applied Physics Letters, 2013. **102**(7): p. 072413.

16.   Jaworski, C., et al., *Observation of the spin-Seebeck effect in a ferromagnetic semiconductor.* Nature materials, 2010. **9**(11): p. 898-903.

17.   Uchida, K.-i., et al., *Observation of longitudinal spin-Seebeck effect in magnetic insulators.* Applied Physics Letters, 2010. **97**(17): p. 172505.

18.   Uchida, K.-i., et al., *Spin seebeck insulator.* Nature materials, 2010. **9**(11): p. 894-897.

19.   Bosu, S., et al., *Spin Seebeck effect in thin films of the Heusler compound Co 2 MnSi.* Physical Review B, 2011. **83**(22): p. 224401.

20.   Jaworski, C., et al., *Giant spin Seebeck effect in a non-magnetic material.* Nature, 2012. **487**(7406): p. 210-213.

21.   Wu, S.M., et al., *Antiferromagnetic spin Seebeck effect.* Physical review letters, 2016. **116**(9): p. 097204.

22.   Prakash, A., et al., *Spin Seebeck effect through antiferromagnetic NiO.* Physical Review B, 2016. **94**(1): p. 014427.

23.   Akopyan, A., et al., *Spin Seebeck effect in Cu 2 OSeO 3: Test of bulk magnon spin current theory.* Physical Review B, 2020. **101**(10): p. 100407.

24.   Kalappattil, V., et al., *Giant spin Seebeck effect through an interface organic semiconductor.* Materials Horizons, 2020.

25.   Santana, F., et al., *Spin Hall angle fluctuations in a device with disorder.* Physical Review B, 2020. **102**(4): p. 041107.

26.   Xu, Z., et al., *Giant Spin Hall Effect in Cu-Tb Alloy Thin Films.* ACS Applied Materials & Interfaces, 2020.

27.   Sahoo, B., et al., *Giant spin Hall angle in Iridium Oxide.* arXiv preprint arXiv:2006.01865, 2020.

28.   Sinova, J., *Thinks globally but acts locally.* Nature materials, 2010. **9**(11): p. 880-881.

29.   Jiang, Z., et al., *Enhanced spin Seebeck effect signal due to spin-momentum locked topological surface states.* Nature Communications, 2016. **7**(1): p. 11458.

30.   Tan, S.G. and M.B.A. Jalil, *2 - Nanoscale physics and electronics*, in *Introduction to the Physics of Nanoelectronics*, S.G. Tan and M.B.A. Jalil, Editors. 2012, Woodhead Publishing. p. 23-77.

31.   Murakami, S. and N. Nagaosa, *1.07 - Spin Hall Effect*, in *Comprehensive Semiconductor Science and Technology*, P. Bhattacharya, R. Fornari, and H. Kamimura, Editors. 2011, Elsevier: Amsterdam. p. 222-278.

32.   Bandyopadhyay, S. and M. Cahay, *Introduction to spintronics*. 2008: CRC press.

33.   Murakami, S., N. Nagaosa, and S.-C. Zhang, *Dissipationless quantum spin current at room temperature.* Science, 2003. **301**(5638): p. 1348-1351.

34.   Bauer, G.E.W., E. Saitoh, and B.J. van Wees, *Spin caloritronics.* Nature Materials, 2012. **11**(5): p. 391-399.

35.   Weiler, M., et al., *Local Charge and Spin Currents in Magnetothermal Landscapes.* Physical Review Letters, 2012. **108**(10): p. 106602.

36.   Maekawa, S., et al., *Spin current*. Vol. 22. 2017: Oxford University Press.

37.   Sinova, J., et al., *Spin hall effects.* Reviews of Modern Physics, 2015. **87**(4): p. 1213.

38.   Yan-Ting, C., et al., *Theory of spin Hall magnetoresistance (SMR) and related phenomena.* Journal of Physics: Condensed Matter, 2016. **28**(10): p. 103004.

39.   Vignale, G., *Ten years of spin hall effect.* Journal of superconductivity and novel magnetism, 2010. **23**(1): p. 3.

40.   Bougiatioti, P., *Thermal spin transport phenomena and magnetic proximity effect in Pt/ferromagnet bilayer systems. Spintronics and spin caloritronics.* 2019.

41.   Misawa, T. and K. Nomura, *Semi-quantized Spin pumping and Spin-orbit torques in topological Dirac Semimetals.* Scientific Reports, 2019. **9**(1): p. 1-8.

42.   Grundler, D., *Spintronics.* Physics World, 2002. **15**(4): p. 39.

43.   Boona, S.R., R.C. Myers, and J.P. Heremans, *Spin caloritronics.* Energy Environ. Sci, 2014. **7**: p. 885.

44. Huang, S.Y., et al., *Intrinsic Spin-Dependent Thermal Transport.* Physical Review Letters, 2011. **107**(21): p. 216604.

45. Weiler, M., et al., *Local Charge and Spin Currents in Magnetothermal Landscapes.* PHYSICAL REVIEW LETTERS, 2012. **108**(10): p. 106602.

46. Bhardwaj, R.G., P.C. Lou, and S. Kumar, *Spin Seebeck effect and thermal spin galvanic effect in Ni80Fe20/p-Si bilayers.* Applied Physics Letters, 2018. **112**(4): p. 042404.

47. Weiler, M., et al., *Local charge and spin currents in magnetothermal landscapes.* Physical review letters, 2012. **108**(10): p. 106602.

48. Kikkawa, T., et al., *Separation of longitudinal spin Seebeck effect from anomalous Nernst effect: Determination of origin of transverse thermoelectric voltage in metal/insulator junctions.* PHYSICAL REVIEW B, 2013. **88**(21): p. 214403.

49. Sola, A., et al., *Evaluation of thermal gradients in longitudinal spin Seebeck effect measurements.* JOURNAL OF APPLIED PHYSICS, 2015. **117**(17): p. 17C510.

50. Meyer , S., et al., *Observation of the spin Nernst effect.* Nature materials, 2017. **16**(10): p. 977.

51. Bose, A. and A.A. Tulapurkar, *Recent advances in the Spin Nernst effect.* Journal of Magnetism and Magnetic Materials, 2019: p. 165526.

52. Kim, D.-J., et al., *Observation of transverse spin Nernst magnetoresistance induced by thermal spin current in ferromagnet/non-magnet bilayers.* Nature Communications, 2017. **8**(1): p. 1400.

53. Chen, Y.-T., et al., *Theory of spin Hall magnetoresistance.* Physical Review B, 2013. **87**(14): p. 144411.

54. Qu, D., et al., *Intrinsic spin Seebeck effect in Au/YIG.* Physical review letters, 2013. **110**(6): p. 067206.

55. Uchida, K., et al., *Spin seebeck insulator.* Nature materials, 2010. **9**(11): p. 894.

56. Uchida, K.-i., et al., *Longitudinal spin-Seebeck effect in sintered polycrystalline (Mn, Zn) Fe 2 O 4.* Applied Physics Letters, 2010. **97**(26): p. 262504.

57. Dejene, F.K., J. Flipse, and B.J. Van Wees, *Spin-dependent Seebeck coefficients of Ni 80 Fe 20 and Co in nanopillar spin valves.* Physical Review B, 2012. **86**(2): p. 024436.

58.   Ramos, R., et al., *Observation of the spin Seebeck effect in epitaxial Fe3O4 thin films.* Applied Physics Letters, 2013. **102**(7): p. 072413.

59.   Schmid, M., et al., *Transverse Spin Seebeck Effect versus Anomalous and Planar Nernst Effects in Permalloy Thin Films.* Physical Review Letters, 2013. **111**(18): p. 187201.

60.   Uchida, K., et al., *Longitudinal spin Seebeck effect: from fundamentals to applications.* Journal of Physics: Condensed Matter, 2014. **26**(34): p. 343202.

61.   Uchida, K., et al., *Observation of the spin Seebeck effect.* Nature, 2008. **455**(7214): p. 778-781.

62.   Jaworski, C.M., et al., *Spin-Seebeck Effect: A Phonon Driven Spin Distribution.* Physical Review Letters, 2011. **106**(18): p. 186601.

63.   Jaworski, C.M., et al., *Giant spin Seebeck effect in a non-magnetic material.* Nature, 2012. **487**(7406): p. 210-213.

64.   Jaworski, C.M., et al., *Observation of the spin-Seebeck effect in a ferromagnetic semiconductor.* Nat Mater, 2010. **9**(11): p. 898-903.

65.   Chang, P.H., et al., *Spin-Seebeck effect on the surface of a topological insulator due to nonequilibrium spin-polarization parallel to the direction of thermally driven electronic transport.* Physical Review B, 2014. **89**(19): p. 195418.

66.   Flipse, J., et al., *Observation of the spin Peltier effect for magnetic insulators.* Physical review letters, 2014. **113**(2): p. 027601.

67.   Jin, H., et al., *Effect of the magnon dispersion on the longitudinal spin Seebeck effect in yttrium iron garnets.* PHYSICAL REVIEW B, 2015. **62**(5): p. 054436.

68.   Kehlberger, A., et al., *Length Scale of the Spin Seebeck Effect.* Physical Review Letters, 2015. **115**(9): p. 096602.

69.   Siegel, Gene, et al., *Robust longitudinal spin-Seebeck effect in Bi-YIG thin films.* Scientific reports, 2014. **4**.

70.   Bosu, S., et al., *Spin Seebeck effect in thin films of the Heusler compound Co2MnSi.* Physical Review B, 2011. **83**(22): p. 224401.

71.   Adachi, H., et al., *Gigantic enhancement of spin Seebeck effect by phonon drag.* Applied Physics Letters, 2010. **97**(25): p. 252506.

72.   Xiao, J., et al., *Theory of magnon-driven spin Seebeck effect.* Physical Review B, 2010. **81**(21): p. 214418.

73.   Uchida, K., et al., *Thermal spin pumping and magnon-phonon-mediated spin-Seebeck effect.* Journal of Applied Physics, 2012. **111**(10): p. 103903.

74.   Bhardwaj, R.G., P.C. Lou, and S. Kumar, *Giant Enhancement in Rashba Spin-Seebeck Effect in NiFe/p-Si Thin Films.* physica status solidi (RRL)–Rapid Research Letters, 2018.

75.   Sola, A., et al., *Evaluation of thermal gradients in longitudinal spin Seebeck effect measurements.* Journal of Applied Physics, 2015. **117**(17): p. 17C510.

76.   Uchida, K., et al., *Spin Seebeck insulator.* Nat Mater, 2010. **9**(11): p. 894-897.

77.   Wang, L., et al., *Giant room temperature interface spin Hall and inverse spin Hall effects.* Physical review letters, 2016. **116**(19): p. 196602.

78.   Sola, A., et al., *Longitudinal spin Seebeck coefficient: heat flux vs. temperature difference method.* Scientific reports, 2017. **7**: p. 46752.

79.   Uchida, K.-i., et al., *Long-range spin Seebeck effect and acoustic spin pumping.* Nature materials, 2011. **10**(10): p. 737-741.

80.   Kirihara, A., et al., *Spin-current-driven thermoelectric coating.* Nature Materials, 2012. **11**(8): p. 686-689.

81.   Kikkawa, T., et al., *Longitudinal Spin Seebeck Effect Free from the Proximity Nernst Effect.* Physical Review Letters, 2013. **110**(6): p. 067207.

82.   Vlietstra, N., et al., *Simultaneous detection of the spin-Hall magnetoresistance and the spin-Seebeck effect in platinum and tantalum on yttrium iron garnet.* Physical Review B, 2014. **90**(17): p. 174436.

83.   Wu, S.M., J.E. Pearson, and A. Bhattacharya, *Paramagnetic spin Seebeck effect.* Physical Review Letters, 2015. **114**(18): p. 186602.

84.   Tian, D., et al., *Separation of spin Seebeck effect and anomalous Nernst effect in Co/Cu/YIG.* Applied Physics Letters, 2015. **106**(21): p. 212407.

85.   Li, J., et al., *Spin Seebeck Effect from Antiferromagnetic Magnons and Critical Spin Fluctuations in Epitaxial FeF 2 Films.* Physical Review Letters, 2019. **122**(21): p. 217204.

86.   Ito, N., et al., *Spin Seebeck effect in the layered ferromagnetic insulators CrSiTe 3 and CrGeTe 3.* Physical Review B, 2019. **100**(6): p. 060402.

87.   Jaworski, C., et al., *Spin-Seebeck effect: A phonon driven spin distribution.* Physical review letters, 2011. **106**(18): p. 186601.

88. Manchon, A., et al., *New perspectives for Rashba spin-orbit coupling.* Nat Mater, 2015. **14**(9): p. 871-882.

89. Soumyanarayanan, A., et al., *Emergent phenomena induced by spin–orbit coupling at surfaces and interfaces.* Nature, 2016. **539**(7630): p. 509-517.

90. Hanakata, P.Z., et al., *Strain-induced gauge and Rashba fields in ferroelectric Rashba lead chalcogenide $\mathrm{Pb}X$ monolayers ($X=\mathrm{S}$, Se, Te).* Physical Review B, 2018. **97**(23): p. 235312.

91. D., N.T., et al., *Nanoscale Flexoelectricity.* Advanced Materials, 2013. **25**(7): p. 946-974.

92. Lee, D. and T.W. Noh, *Giant flexoelectric effect through interfacial strain relaxation.* Philosophical Transactions of the Royal Society A: Mathematical, Physical and Engineering Sciences, 2012. **370**(1977): p. 4944.

93. Das, S., et al., *Enhanced flexoelectricity at reduced dimensions revealed by mechanically tunable quantum tunnelling.* Nature Communications, 2019. **10**(1): p. 537.

94. Kato, Y., et al., *Coherent spin manipulation without magnetic fields in strained semiconductors.* Nature, 2004. **427**: p. 50.

95. Wu, Z., J.B. Neaton, and J.C. Grossman, *Charge Separation via Strain in Silicon Nanowires.* Nano Letters, 2009. **9**(6): p. 2418-2422.

96. Li, X., et al., *Magnetic properties of permalloy films with different thicknesses deposited onto obliquely sputtered Cu underlayers.* Journal of Magnetism and Magnetic Materials, 2015. **377**: p. 142-146.

97. Haumer, P., et al., *Hysteresis modeling of thin permalloy films and parameter interpretation.* IEEE Transactions on Magnetics, 2004. **40**(4): p. 2745-2747.

98. Holanda, J., et al., *Longitudinal spin Seebeck effect in permalloy separated from the anomalous Nernst effect: Theory and experiment.* Physical Review B, 2017. **95**(21): p. 214421.

99. Yin, S.L., et al., *Hybrid anomalous and planar Nernst effect in permalloy thin films.* Physical Review B, 2013. **88**(6): p. 064410.

100. Lou, P.C. and S. Kumar, *Spin mediated enhanced negative magnetoresistance in Ni80Fe20 and p-silicon bilayer.* Solid State Communications, 2017. **259**: p. 24-28.

101. Lou, P.C., W.P. Beyermann, and S. Kumar, *Spin mediated magneto-electro-thermal transport behavior in Ni80Fe20/MgO/p-Si thin films.* Journal of Applied Physics, 2017. **122**(12): p. 123905.

102. Chen, L., et al., *Robust spin-orbit torque and spin-galvanic effect at the Fe/GaAs (001) interface at room temperature.* Nature Communications, 2016. **7**(1): p. 13802.

103. Shen, K., G. Vignale, and R. Raimondi, *Microscopic Theory of the Inverse Edelstein Effect.* Physical Review Letters, 2014. **112**(9): p. 096601.

104. Avci, C.O., et al., *Fieldlike and antidamping spin-orbit torques in as-grown and annealed Ta/CoFeB/MgO layers.* Physical Review B, 2014. **89**(21): p. 214419.

105. Brataas, A. and K.M.D. Hals, *Spin–orbit torques in action.* Nature Nanotechnology, 2014. **9**(2): p. 86-88.

106. Fan, Y., et al., *Magnetization switching through giant spin–orbit torque in a magnetically doped topological insulator heterostructure.* Nature Materials, 2014. **13**(7): p. 699-704.

107. Lau, Y.-C., et al., *Spin–orbit torque switching without an external field using interlayer exchange coupling.* Nature Nanotechnology, 2016. **11**(9): p. 758-762.

108. Fukami, S., et al., *Magnetization switching by spin–orbit torque in an antiferromagnet–ferromagnet bilayer system.* Nature Materials, 2016. **15**(5): p. 535-541.

109. Sola, A., et al., *Longitudinal spin Seebeck coefficient: heat flux vs. temperature difference method.* Scientific Reports, 2017. **7**(1): p. 46752.

110. Cahill, D.G., *Thermal conductivity measurement from 30 to 750 K: the 3ω method.* Review of scientific instruments, 1990. **61**(2): p. 802-808.

111. Hopkins, P.E. and L.M. Phinney, *Thermal Conductivity Measurements on Polycrystalline Silicon Microbridges Using the 3ω Technique.* Journal of Heat Transfer, 2009. **131**(4).

112. Liu, W. and M. Asheghi, *Thermal conduction in ultrathin pure and doped single-crystal silicon layers at high temperatures.* Journal of Applied Physics, 2005. **98**(12): p. 123523.

113. Avery, A.D., et al., *Thermal and electrical conductivity of approximately 100-nm permalloy, Ni, Co, Al, and Cu films and examination of the Wiedemann-Franz Law.* Physical Review B, 2015. **92**(21): p. 214410.

114. Kikkawa, T., et al., *Separation of longitudinal spin Seebeck effect from anomalous Nernst effect: Determination of origin of transverse thermoelectric voltage in metal/insulator junctions.* Physical Review B, 2013. **88**(21): p. 214403.

115. Uchida, K., et al., *Thermal spin pumping and magnon-phonon-mediated spin-Seebeck effect.* Journal of Applied Physics, 2012. **111**(10): p. -.

116. Schwab, P. and R. Raimondi, *Magnetoconductance of a two-dimensional metal in the presence of spin-orbit coupling.* The European Physical Journal B - Condensed Matter and Complex Systems, 2002. **25**(4): p. 483-495.

117. Dolgopolov, V.T., A.A. Shashkin, and S.V. Kravchenko, *Spin polarization and exchange-correlation effects in transport properties of two-dimensional electron systems in silicon.* Physical Review B, 2017. **96**(7): p. 075307.

118. Broto, J.M., et al., *Magnetoresistance of a Si-MOSFET structure in a parallel magnetic field.* Physica B: Condensed Matter, 2004. **346**(Supplement C): p. 493-497.

119. Okamoto, T., et al., *Spin polarization and metallic behavior in a silicon two-dimensional electron system.* Physical Review B, 2004. **69**(4): p. 041202.

120. Ono, K., et al., *Hole Spin Resonance and Spin-Orbit Coupling in a Silicon Metal-Oxide-Semiconductor Field-Effect Transistor.* Physical Review Letters, 2017. **119**(15): p. 156802.

121. Miao, B.F., et al., *Inverse Spin Hall Effect in a Ferromagnetic Metal.* Physical Review Letters, 2013. **111**(6): p. 066602.

122. Dash, S.P., et al., *Electrical creation of spin polarization in silicon at room temperature.* Nature, 2009. **462**(7272): p. 491-494.

123. Dejene, F.K., et al., *Spin heat accumulation and spin-dependent temperatures in nanopillar spin valves.* Nat Phys, 2013. **9**(10): p. 636-639.

124. Takayama, A., et al., *Tunable Spin Polarization in Bismuth Ultrathin Film on Si(111).* Nano Letters, 2012. **12**(4): p. 1776-1779.

125. Lou, P.C. and S. Kumar, *Spin-Driven Emergent Antiferromagnetism and Metal–Insulator Transition in Nanoscale p-Si.* Physica Status Solidi B: Basic Research, 2017.

126. Lou, P.C. and S. Kumar, *Spin-Hall effect and emergent antiferromagnetic phase transition in n-Si.* Journal of Magnetism and Magnetic Materials, 2017.

127. Skinner, T.D., et al., *Complementary spin-Hall and inverse spin-galvanic effect torques in a ferromagnet/semiconductor bilayer.* Nature Communications, 2015. **6**: p. 6730.

128. Jiang, Z., et al., *Enhanced spin Seebeck effect signal due to spin-momentum locked topological surface states.* Nat Commun, 2016. **7**: p. 11458.

129. Qu, D., et al., *Inverse spin Hall effect in AuxTa1-x alloy films.* Physical Review B, 2018. **97**(2): p. 024402.

130. Liu, L., et al., *Spin-torque switching with the giant spin Hall effect of tantalum.* Science (New York, N.Y.), 2012. **336**: p. 555-8.

131. Hao, Q., W. Chen, and G. Xiao, *Beta (β) tungsten thin films: Structure, electron transport, and giant spin Hall effect.* Applied Physics Letters, 2015. **106**(18): p. 182403.

132. Lou, P.C. and S. Kumar, *Spin-Driven Emergent Antiferromagnetism and Metal–Insulator Transition in Nanoscale p-Si.* physica status solidi (b), 2017: p. 1700545.

133. Lou, P.C. and S. Kumar, *Spin-Hall effect and emergent antiferromagnetic phase transition in n-Si.* Journal of Magnetism and Magnetic Materials, 2018. **452**: p. 129-133.

134. Hoffman, S., K. Sato, and Y. Tserkovnyak, *Landau-Lifshitz theory of the longitudinal spin Seebeck effect.* Physical Review B, 2013. **88**(6): p. 064408.

135. Hopkins, P.E. and L.M. Phinney, *Thermal Conductivity Measurements on Polycrystalline Silicon Microbridges Using the 3ω Technique.* Journal of Heat Transfer, 2009. **131**(4): p. 043201-043201-8.

136. Gierz, I., et al., *Silicon Surface with Giant Spin Splitting.* Physical Review Letters, 2009. **103**(4): p. 046803.

137. Matsushita, S.Y., et al., *Anisotropic electronic band structure of intrinsic Si(110) studied by angle-resolved photoemission spectroscopy and first-principles calculations.* Physical Review B, 2017. **96**(12): p. 125302.

138. Hrabec, A., et al., *Spin-orbit interaction enhancement in permalloy thin films by Pt doping.* Physical Review B, 2016. **93**(1): p. 014432.

139. Lou, P.C. and S. Kumar, *Generation and detection of dissipationless spin current in a MgO/Si bilayer.* Journal of Physics: Condensed Matter, 2018. **30**(14): p. 145801.

140. Qu, D., et al., *Self-consistent determination of spin Hall angles in selected 5d metals by thermal spin injection.* Physical Review B, 2014. **89**(14): p. 140407.

141. Ramos, R., et al., *Thermoelectric performance of spin Seebeck effect in Fe3O4/Pt-based thin film heterostructures.* APL Materials, 2016. **4**(10): p. 104802.

142. Lin, W., et al., *Enhancement of Thermally Injected Spin Current through an Antiferromagnetic Insulator.* Physical Review Letters, 2016. **116**(18): p. 186601.

143. Ramos, R., et al., *Temperature dependence of the spin Seebeck effect in [Fe3O4/Pt]n multilayers.* AIP Advances, 2017. **7**(5): p. 055915.

144. Rezende, S.M., et al., *Magnon spin-current theory for the longitudinal spin-Seebeck effect.* Physical Review B, 2014. **89**(1): p. 014416.

145. Meier, D., et al., *Thermally driven spin and charge currents in thin NiFe${}_{2}$O${}_{4}$/Pt films.* Physical Review B, 2013. **87**(5): p. 054421.

146. Lou, P.C., et al., *Large spin Hall effect in Si at room temperature.* Physical Review B, 2020. **101**(9): p. 094435.

147. Yang, M.-M., D.J. Kim, and M. Alexe, *Flexo-photovoltaic effect.* Science, 2018.

148. Noël, P., et al., *Non-volatile electric control of spin–charge conversion in a SrTiO3 Rashba system.* Nature, 2020. **580**(7804): p. 483-486.

149. Martin, L.W. and A.M. Rappe, *Thin-film ferroelectric materials and their applications.* Nature Reviews Materials, 2017. **2**(2): p. 16087.

150. Cahill, D.G., *Thermal conductivity measurement from 30 to 750 K: the 3 omega method.* Review of Scientific Instruments, 1990. **61**(2): p. 802-808.

151. Chuang, T.C., et al., *Enhancement of the anomalous Nernst effect in ferromagnetic thin films.* Physical Review B, 2017. **96**(17): p. 174406.

152. Tian, D., et al., *Separation of spin Seebeck effect and anomalous Nernst effect in Co/Cu/YIG.* Applied Physics Letters, 2015. **106**(21): p. 212407.

153. Jin, H., et al., *Effect of the magnon dispersion on the longitudinal spin Seebeck effect in yttrium iron garnets.* Physical Review B, 2015. **92**(5): p. 054436.

154. Kikkawa, T., et al., *Critical suppression of spin Seebeck effect by magnetic fields.* Physical Review B, 2015. **92**(6): p. 064413.

155. Avery, A.D., M.R. Pufall, and B.L. Zink, *Determining the planar Nernst effect from magnetic-field-dependent thermopower and resistance in nickel and permalloy thin films.* Physical Review B, 2012. **86**(18): p. 184408.

156. Slachter, A., F.L. Bakker, and B.J. van Wees, *Anomalous Nernst and anisotropic magnetoresistive heating in a lateral spin valve.* Physical Review B, 2011. **84**(2): p. 020412.

157. Wang, W., et al., *Anomalous spin–orbit torques in magnetic single-layer films.* Nature Nanotechnology, 2019. **14**(9): p. 819-824.

158. Yang, A.C., et al., *Rashba spin–orbit coupling enhanced anomalous Hall effect in MnxSi1−x/SiO2/Si p–i–n junctions.* RSC Advances, 2016. **6**(61): p. 55930-55935.

159. Ishizuka, H. and N. Nagaosa, *Spin chirality induced skew scattering and anomalous Hall effect in chiral magnets.* Science Advances, 2018. **4**.

160. Wang, Y., et al., *Determination of intrinsic spin Hall angle in Pt.* Applied Physics Letters, 2014. **105**(15): p. 152412.

161. Sinova, J., et al., *Spin Hall effects.* Reviews of Modern Physics, 2015. **87**(4): p. 1213-1260.

162. Weng, Y.-C., C.T. Liang, and J.G. Lin, *Modulation of spin-charge conversion in silicon.* Applied Physics Letters, 2019. **115**(23): p. 232101.

163. Shikoh, E., et al., *Spin-Pump-Induced Spin Transport in p-Type Si at Room Temperature.* Physical Review Letters, 2013. **110**(12): p. 127201.

164. Mosendz, O., et al., *Quantifying Spin Hall Angles from Spin Pumping: Experiments and Theory.* Physical Review Letters, 2010. **104**(4): p. 046601.

165. Noel, P., et al., *Highly Efficient Spin-to-Charge Current Conversion in Strained HgTe Surface States Protected by a HgCdTe Layer.* Physical Review Letters, 2018. **120**(16): p. 167201.

166. Rojas-Sánchez, J.C., et al., *Spin to Charge Conversion at Room Temperature by Spin Pumping into a New Type of Topological Insulator: $\ensuremath{\alpha}$-Sn Films.* Physical Review Letters, 2016. **116**(9): p. 096602.

167. Lesne, E., et al., *Highly efficient and tunable spin-to-charge conversion through Rashba coupling at oxide interfaces.* Nature Materials, 2016. **15**: p. 1261.

168. Vaz, D.C., et al., *Mapping spin–charge conversion to the band structure in a topological oxide two-dimensional electron gas.* Nature Materials, 2019.